Projection-based Topology Optimization Method for Linear and Nonlinear Design

by

Hao Deng

B.S., Beihang University, 2014

M.S., Beihang University, 2017

Submitted to the Graduate Faculty of the

Swanson School of Engineering in partial fulfillment

of the requirements for the degree of

Doctor of Philosophy

University of Pittsburgh

2021

UNIVERSITY OF PITTSBURGH

SWANSON SCHOOL OF ENGINEERING

This dissertation was presented

by

Hao Deng

It was defended on

July 12, 2021

and approved by

Qing-Ming Wang, Ph.D., Professor, Department of Mechanical Engineering and Materials Science

Xiayun Zhao, Ph.D., Assistant Professor, Department of Mechanical Engineering and Materials Science

Jeen-Shang Lin, Sc.D., Associate Professor, Department of Civil and Environmental Engineering

Dissertation Director: Albert C. To, Ph.D., William Kepler Whiteford Professor, Department of Mechanical Engineering and Materials Science

Projection-based Topology Optimization Method for Linear and Nonlinear Design

Hao Deng, Ph.D.

University of Pittsburgh, 2021

Lighter designs are desirable in many industrial applications and structural optimization is an effective way to generate lightweight structures. Topology optimization is an important tool for investigating the optimal design of engineering structures. Although continuum topology optimization method has already achieved remarkable progress in recent years, there still exist several challenges for conventional density-based method such as manufacturability. Additive manufacturing (AM) is a rapidly developing technology by which the design can achieve more freedom. However, it does not mean that the optimized design generated by topology optimization algorithm can be directly manufactured without any geometry post-processing. Besides AM techniques, the traditional manufacturing methods of machining and casting are also popular in recent years, because the majority of engineering parts are manufactured through these methods. It is difficult for conventional density-based method to account for these manufacturing constraints. The projection-based topology optimization approach is a new trend in this field to properly restrict the optimal solutions by implementing geometric constraints. The nature of projection method is to apply new design variables projected in a pseudo-density domain to find the optimal solutions.

In this dissertation, several advanced projection-based topology optimization schemes are proposed to resolve linear and nonlinear design problems and demonstrated through numerical examples. In chapter 2 and 3, a new projection technique is proposed to resolve nonlinear topology

optimization problems with large deformation. Chapter 4 describes a novel design method, which combines the TPMS (Triply periodic minimal surface) formulation with standard projection-based method to design functionally graded TPMS lattice. In chapter 5, a projection-based method is combined with moving particles for reverse shape compensation for additive manufacturing technique. Chapter 6 describes a density-based boundary evolving algorithm based on projection function for continuum-based topology optimization. In the chapter 7, a novel projection-based method for structural design considering restrictions of multi-axis machining processes is proposed.

Table of Contents

List of Tables

List of Figures

Preface

The four-year experience at University of Pittsburgh is unforgettable. I feel lucky to go through my PhD qualification and obtain PhD degree successfully. I would like to thank many people who provide me valuable instructions and guidance to me during my PhD career, which has led to the completion of this dissertation.

First, thanks to my PhD advisor Albert C To, who instructs me to do several challenging research problems and give me enough freedom to do research of my interests. Secondly, I would like to say sincere thanks to my committee members, Prof. Qing-Ming Wang, Prof. Xiayun Zhao, and Prof. Jeen-Shang Lin for their serving on my committee regardless of tight time schedule. They gave me a lot of valuable comments and suggestions of my dissertation. Third, I would like to express my gratitude to my colleagues in the computational mechanics group for their collaboration and help. I would like to give many thanks to my past and current members: Dr. Xuan Liang, Praveen Vulimiri, Basil Paudel, Shawn Hinnebusch, and among others, for their generous support and advice. At last, I want to express my deepest and sincere gratitude to my parents for their endless support and encouragement.

1.0 Introduction

The primary goal of this dissertation is to propose several advanced projection-based methods for structural and shape optimization ranging from linear to nonlinear physical problems. The main focus of the proposed methods lies in the implementation of manufacturing constraints for optimal designs. The motivation, background and research objective are presented in this chapter.

1.1 Topology Optimization

Structural topology optimization is a tool for distributing material in a prescribed domain to obtain optimized structural performance through an optimal way. Topology optimization experienced a rapid development since the pioneering works of Bendsoe and Kikuchi[1]. Nowadays, several advanced and powerful methods have been proposed for topology optimization (TO), where TO method is already been used in many application fields. A state-of-the-art review of recent developments in TO can be found in Refs [2-7]. Solid Isotropic Material Penalty (SIMP) method [8] and level set method [9, 10] are the most common TO methods. The SIMP method penalizes the intermediate region to obtain a solid-void design, while the level set method represents the structural design implicitly via the zero-level set of a function, which does not require penalization of intermediate densities and a clear solid-void interface can be found. Instead, this advantage of level set method may come at the expense of other challenges such as relatively poor convergence [2]. Besides the conventional topology optimization method, several new TO

method are proposed in recent years. Guo et al [11, 12] proposed a new computational framework called the moving morphable component (MMC), which embeds moving morphable components within the level set scheme. This computational scheme incorporates geometry and mechanical information into topology optimization in an explicit way, and the structural complexity can be easily controlled in an explicit way. Another method called the Moving Morphable Voids (MMVs) was also proposed by Guo et al [13, 14], which introduced a set of geometry parameters to describe the boundary of the structure in an explicit way. Recently, Tortorelli and colleagues [15] proposed a geometry projection method for the continuum-based topology optimization made of discrete elements. This method uses a differentiable projection of geometry onto a fixed background mesh for optimization. The sensitivities of objective functions with respect to the explicit geometry parameterization are readily derived based on the chain rule. Note that this method is in the context of density-based computational framework, and hence standard finite element method (FEM) and nonlinear programming algorithm can be applied. Furthermore, the projection-based geometry description method has been extended to solve stress constraint problem, inverse design of lattice, three-dimensional compliance problem, and multi-material designs, etc [16-23]. Meanwhile, several other advanced topology optimization methods are proposed in recent years [24-26]. Educational code for topology optimization is very important and useful for engineers and researchers to get started with. After the Top99 MATLAB code [27]developed by Sigmund for simple 2D topology optimization problem, several other codes have been followed, which significantly promoted the development of this research field. A table is listed here which reviews the published codes in recent years including three major methods: SIMP [28], level set [29], and BESO[30]. These codes are helpful for students and engineers to understand the basic mathematical formulation of topology optimization.

Table 1.1 Educational code for topology optimization

Authors and Reference	Programming language	Method
(2001) O. Sigmund [27]	MATLAB	SIMP
(2005) Liu Z, Korvink J G et al [31]	FEMLAB	Level set
(2010) Challis V J [32]	MATLAB	Level set
(2010) Suresh, Krishnan [33]	MATLAB	SIMP (Pareto)
(2010) Huang X, Xie Y M. [30]	MATLAB	BESO
(2011) Andreassen, Erik, et al [34]	MATLAB	SIMP
(2012) Talischi, Cameron, et al [35]	MATLAB	PolyTop
(2014) Zegard T, Paulino G H [36]	MATLAB	Ground Structure
(2015) Aage, Niels, et al. [37]	PETSc	SIMP
(2015) Otomori, Masaki, et al. [38]	MATLAB	Level set
(2015) Xia L, Breitkopf P [39]	MATLAB	SIMP
(2016) Pereira, Anderson, et al [40]	MATLAB	PolyTop
(2018) Wei, Peng, et al [41]	MATLAB	Level set
(2018) Loyola, Rubén Ansola, et al [42]	MATLAB	SERA
(2018) Laurain, Antoine. [43]	FEniCS	Level set
(2018) Sanders, Emily D., et al. [44]	MATLAB	PolyMat
(2018) Dapogny, Charles, et al. [45]	FreeFem++	Shape variation
(2019) Chen Q, Zhang X, Zhu B. [46]	MATLAB, APDL	SIMP
(2019) Gao, Jie, et al. [47]	MATLAB	SIMP
(2019) Liang Y, Cheng G. [48]	MATLAB	Integer programming
(2020) Smith H, Norato J A.[49]	MATLAB	Geometry projection
(2020) Picelli R, et al. [50]	MATLAB	TOBS
(2020) Lin H, Xu A, Misra A, et al. [51]	APDL	DER-BESO
(2020) Ferrari F, Sigmund O. [52]	MATLAB	SIMP

1.2 Soft Material Design

In recent years, designing the flexible electronics, soft robots and wearable electronic devices draws great attention from academia and industry due to their extraordinary mechanical response [53-55]. Such devices and structures usually experience large deformations under external loading conditions, which is different from the traditional stiff structure design. Recently, topology optimization methods are utilized to design flexible and soft structures based on finite deformation theory. For the SIMP method, Bruns and Tortorelli [56] embedded a filtering scheme

into SIMP method to design compliant mechanism, where the geometric and material nonlinearities are considered. Wallin et al [57] compared different stiffness measurement for compliant mechanism design under large deformation. Fengwen et al [58] proposed a new energy interpolation scheme to stabilize the numerical simulations for topology optimization, where the mesh distortion phenomenon is alleviated when structures undergo large deformation. Ivarsson et al [59] applied a transient finite strain viscoplastic model in gradient-based topology optimization framework to design impact mitigating structures. Li et al [60] extended the shape preserving topology optimization approach from linear elastic case to geometrically nonlinear problems, where the structural complementary elastic work is chosen as objective function. Luo et al [61] proposed a simple and effective additive hyperelasticity technique to circumvent excessive mesh distortion in solving the density-based topology optimization of elastic structures undergoing large deformation. Ortigosa et al [62] proposed a novel stabilized computational approach for SIMP-based TO method for hyperelastic material design subjected to very large deformation. For level set method, Chen et al [63] proposed an effective level-set-based topology optimization method for the design of hyperelastic structures undergoing large deformation. Luo et al [64] presented an effective topology optimization methodology for the compliance design of hyperelastic material with frictionless contact supports. Chung et al [65] proposed a level-set based topology optimization method for designing structures undergoing large deformation due to thermal and mechanical loads, where the thermo-mechanical response can be controlled via topology optimization. Xue et al [66] performed structural topology optimization under finite deformation using explicit geometry description, where a Moving Morphable Void (MMV)-based approach is developed for designing large deformation mechanism. Kato et al [67] proposes a method of micro-macro concurrent topology optimization for a two-phase nonlinear solid to minimize the

end compliance of its microstructure undergoing large deformation. Some other related works can be found in Ref [68-71].

1.3 Manufacturing Constraint

In the past, fabrication of complex geometry is limited by manufacturing techniques, but recent rapid advancement of 3D printing technology makes these designs achievable nowadays. 3D printing is recognized as a technology that increasing ‘design freedom’ and allows designers and engineers to create unique products. Despite these advantages, AM has its unique limitations which should be addressed, and these limitations inevitable limit the geometry complexity to some extends. Therefore, manufacturing-oriented topology optimization become a new trend in optimization design research field. Besides the AM technique, multi-axis machining is also a widely used techniques in subtractive manufacturing for metal component production. The unnecessary material is removed by machining tool until the desired shape achieves. For high-strength aerospace or naval structures, multi-axis machining is an ideal option for manufacturing parts. Thus, how to effective generate the designs which are ready for subtractive manufacturing is a meaningful research topic.

1.4 Research Objectives

1.4.1 Projection-based Topology Optimization Method for Buckling-induced Design

Motivated by key advances in manufacturing techniques, the tailoring of materials to achieve novel properties such as energy dissipation properties has been the focus of active research in engineering and materials science over the past decade. The goal of material design is to determine the optimal spatial layout to achieve a desired macroscopic constitutive response. However, the manufacturing abilities are the key factors to constrain the feasible design space, eg, minimum length and geometry complexity. Conventional density-based method, where each element works as a variable, always results in complicated geometry with large number of small intricate features. To address the challenges, a new density field representation technique, named, Heaviside function-based geometric representation algorithm, is proposed in this chapter, where density field is represented by truss-like components. Truss-like components have less control parameters and easier to handle for sensitivities derivation, especially for distance sensitivities. Using bar components to explicitly represent density field can explore design space effectively and generate simple structures without any intricate small features at borders. Furthermore, this density representation method is mesh independent and design variables are reduced significantly so that optimization problem can be solved efficiently using small-scale optimization algorithm, eg, sequential quadratic programming.

1.4.2 Bézier Skeleton Explicit Density (BSED) Representation Algorithm for Metamaterial Design

Motivated by key advances in manufacturing techniques, the tailoring of materials to achieve novel properties such as energy dissipation properties has been the focus of active research in engineering and materials science over the past decade. The goal of material design is to determine the optimal spatial. A new density field representation technique called the Bézier skeleton explicit density (BSED) representation scheme for topology optimization of stretchable metamaterials under finite deformation is proposed for the first time. The proposed approach overcomes a key deficiency in existing density-based optimization methods that typically yield designs that do not have smooth surfaces but have large number of small intricate features, which are difficult to manufacture even by additive manufacturing. In the proposed approach, Bézier curves are utilized to describe the skeleton of the design being optimized where the description of the entire design is realized by assigning thickness along the curves. This geometric representation technique ensures that the optimized design is smooth and concise and can easily be tuned to be manufacturable by additive manufacturing. In the optimization method, the density field is described by the Heaviside function defined on the Bézier curves. Compared to NURBS or B-spline based models, Bézier curves have fewer control parameters and hence are easier to manipulate for sensitivity derivation, especially for distance sensitivities. Due to its powerful curve fitting ability, using Bézier curve to represent density field allows exploring design space effectively and generating concise structures without any intricate small features at the borders. Furthermore, this density representation method is mesh independent and design variables are reduced significantly so that optimization problem can be solved efficiently using small-scale optimization algorithms such as sequential quadratic programming.

1.4.3 Projection-based Method for Flexible Functionally Graded Lattice Design

The goal is to propose a projection-based implicit modeling method (PIMM) for functionally graded lattice optimization, which does not require any homogenization techniques. In this method, a parametric projection function is proposed to link the implicit function of functionally graded lattice with the finite element background mesh. To reduce the number of design variables, the radial basis function (RBF) is utilized to interpolate the implicit design field. The triply periodic minimal surface (TPMS) lattice is employed to demonstrate the proposed method. Compared with conventional homogenization-based topology optimization, the proposed method can effectively resolve the stress-constrained lattice design; for example, sharp corners are removed from the initial design after optimization. The proposed PIMM method is flexible and can potentially be extended to design graded irregular porous scaffold and non-periodic lattice infill designs.

1.4.4 Reverse Shape Compensation via a Projection-based Moving Particle Optimization Method

Reverse shape compensation is widely used in additive manufacturing to offset the displacement distortion caused by various sources, such as volumetric shrinkage, thermal cooling, etc. Also, reverse shape compensation is also an effective tool for the four-dimensional (4D) printing techniques, shape memory polymers (SMPs) , or 3D self-assemble structures to achieve a desired geometry shape under environmental stimuli such as electricity, temperature, gravity etc. A gradient-based moving particle optimization method for reverse shape compensation is proposed to achieve a desired geometry shape under a given stimuli. The geometry is described by discrete

particles, where the radius basis kernel function is used to realize a mapping from particle to density field, and finite element analysis is used to compute the deformation under the external stimulus. The optimization problem is formulated in detail, and MMA optimizer is implemented to update the location of discrete particles based on sensitivity information. In this work, self-weight due to gravity imposed on linear elastic structures is considered as the source of deformation. The objective of the problem is then to find the initial shape so that the deformed shape under gravity is close to desired geometry shape. The computational framework for reverse shape compensation described here has the potential to be extended to consider linear and non-linear deformation induced by other external stimuli.

1.4.5 Projection-based Boundary Evolving Method for Large Deformation Design

We propose a density-based boundary evolving algorithm for continuum-based topology optimization. The boundary of voids in the design domain is described by RBF (radial basis function) function controlled by RBF knots in polar coordinate, where the voids are projected onto a fixed grid using Heaviside function. For merging overlapped multiple voids, the p-norm function is introduced to describe composite density field. The differentiability of the projection-based boundary description algorithm allows for the sensitivity analysis via the chain rule, and therefore, it enables an efficient gradient-based optimization method. The goal of this chapter is to optimize the initial design to generate buckling-induce mechanism under large deformation, and without loss of generality, the hyperelastic material model is chosen to describe the material behavior. Notably, this method possesses the merit of level set method, where the intermediate density only exists at the boundary of topology shape. At the same time, the proposed method is still in the

density-based optimization framework and standard sensitivity analysis of density-based methods can be directly derived based on the chain rule.

1.4.6 Projection-based Topology Optimization Method for Multi-Axis Machining

This chapter proposes a novel projection-based method for structural design considering restrictions of multi-axis machining processes. A new mathematical formulation based on Heaviside function is presented to transform the design field into a geometry which can be manufactured by multi-axis machining process. The formulation is developed for 5-axis machining, which can be also applied to 2.5D milling restriction. The filter techniques are incorporated to effectively control the minimum size of void region. The standard compliance minimization problem is demonstrated to explore different machinable freeform designs using proposed approach.

2.0 Projection-based Topology Optimization Method for Buckling-induced Design

2.1 Large Deformation Optimization Problem Description

The last decade has witnessed rapid incorporation of soft rubberlike elastomers that exhibit instantaneous elastic response up to large strains into a wide range of engineering applications. For instance, soft electronics or soft robotics, largely constructed from soft rubberlike materials are capable to achieve bio-induced functionality. Compared to small deformation problem, both material and geometry nonlinearity need to be considered for large deformation topology optimization problem. Hyperelastic material model is a general mathematical model to describe the deformation behavior of soft material under external response. A hyperelastic material is a type of constitutive model for which the stress–strain relationship derives from a strain energy density function.

2.2 Nonlinear Finite Element Analysis based on Total Lagrangian Formulation

The analysis model of a hyperelastic body under external loading is briefly described in this section. This is a classical theory and well-developed in the past few years [72-76]. When a hyperelastic body undergoes a large deformation, the deformed configuration and undeformed configuration are presented in Figure 2.1. Here, the subscript ‘0’ denote the undeformed state. The total Lagrangian formulation, which uses the undeformed geometry as reference, is applied here to obtain the structural equilibrium equation. Hyperelastic materials belong to a particular class of

elastic materials where the stress field in the material can be determined by differentiating strain density energy with respect to strain without considering deformation history.

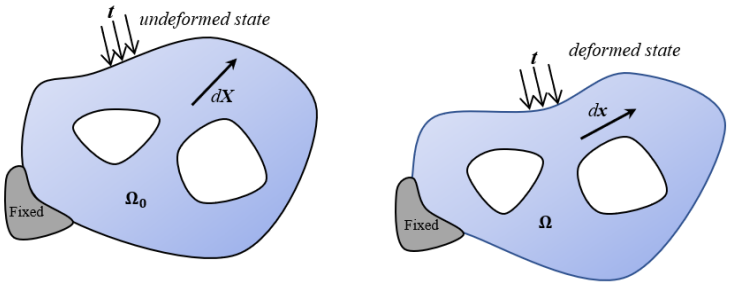

Figure 2.1 Deformation of a continuum body from its undeformed configuration to a deformed configuration

A point locates at $\boldsymbol{X}$ at initial state transfers to $\boldsymbol{x}$ in the deformed configuration, and the displacement vector is $\boldsymbol{u} = \boldsymbol{x} - \boldsymbol{X}$. Transformation can be described by deformation gradient $\boldsymbol{F}$,

$$F = \boldsymbol{I} + \frac{\partial \boldsymbol{u}}{\partial \boldsymbol{X}} = \boldsymbol{I} + \nabla_0 \boldsymbol{u} \tag{2.1}$$

Note that $\boldsymbol{I}$ is second-order identity tensor. Spatial equilibrium equation for a deformable body is written as,

$$div\, \boldsymbol{\sigma} + \boldsymbol{f} = \boldsymbol{0} \tag{2.2}$$

where $\boldsymbol{\sigma}$ is Cauchy stress tensor, $\boldsymbol{f}$ is body force. In this chapter, the Mooney-Rivlin model [77], which is one of the most popular hyperelastic material model, is adopted here to describe the strain energy function. The principle of minimum potential energy and variational method are used to obtain quasi-static physical equations for hyperelastic materials. To simplify our problem, conservative external force is assumed here, which is independent of structural deformation. The governing equation (2.2) is resolved using the finite element method with the Newton-Raphson scheme as described in Ref [74]. It is necessary to note that both material nonlinearity and geometric nonlinearity need to be taken into consideration during hyperelastic material deformation analysis. For hyperelastic materials, the stress is obtained directly from strain energy.

Several models have been proposed to model these materials such as the Mooney-Rivlin model. The three invariants of the right Cauchy-Green deformation tensor are expressed as follows:

$$I_1 = \boldsymbol{C}:\boldsymbol{I}$$
$$I_2 = \boldsymbol{C}:\boldsymbol{C} \tag{2.3}$$
$$I_3 = det(\boldsymbol{C})$$

where $\boldsymbol{C}$ is the right Cauchy–Green deformation tensor, and $\boldsymbol{I}$ is identity tensor. Mathematical operator (:) denotes double contraction of two tensors. The strain energy expression of Mooney-Rivlin model, which include the effect of the first and second invariants I_1 and I_2, can be written as follows:

$$\psi(J_1, J_2, J_3) = A_{10}\left(I_1 I_3^{-1/3} - 3\right) + A_{01}\left(I_2 I_3^{-2/3} - 3\right) + \frac{K}{2}(I_3^{1/2} - 1)^2 \tag{2.4}$$

where A_{10} and A_{01} are two nonzero parameters, which need to be determined through material testing. K is the bulk modulus. Most hyperelastic materials such as rubber have a large bulk modulus, which means a small volume change leads to a large hydrostatic pressure.

2.3 The Challenges and Solutions for Capturing Nonlinear Behavior

There are several challenges to optimize metamaterial to achieve extreme damping behavior. Some of the challenges are induced by the optimization formulation such as failure constraint and cost function, the others are inherent to the highly complex nonlinear behavior of instability that we try to capture. To resolve the challenges for capturing nonlinear behavior, essential numerical algorithm is introduced and implemented as follows. a) Because of the geometric nonlinearity, a so-called "element instability" phenomenon will happen, which is caused

by excessive mesh distortion of the low-density elements. Once element in low density area are instable, failing to capture the equilibrium state is an inevitable issue arisen in FEM analysis due to the non-convergence of the Newton-Raphson method. Two simple techniques are developed in the past, namely "convergence criterion relaxation" [78] and the "element removal" [79]. However, above two schemes do not present satisfactory performance for very large deformation such as snap through behavior. Recently, a new energy interpolation scheme [80] is proposed by Wang et.al to alleviate mesh excessive distortion phenomenon. Based on this method, two different FEM models are applied at low stiffness regions and high stiffness regions, which is achieved using energy interpolation with a threshold projection function. Here, we apply energy interpolation scheme to resolve mesh excessive distortion. b) Snap through and snap back phenomenon pose some of the most difficult problems in nonlinear analysis. How to effectively trace such a complex load path is quite necessary for optimization design. The Newton-Raphson method is a popular and efficient algorithm to solve nonlinear equations, while this method always fails in load-control analysis when snap through behavior happens. One way to circumvent this issue is by applying displacement control, but still cannot avoid the issue of the snap-back behavior. The arc length method (ALCM) [81] is a common method to solve a system of equations when there exists one or more critical points. Although arc length method is well developed in recent years, one of the major limitations of this method is in correctly determining the direction of load increment [82]. Meanwhile, numerical instability near instability points is the other issue for ALCM. Generalized displacement control method [83] has been proposed as an alternative method to follow loading path, which already shows great potential for complex nonlinear problems. Recently, a modification of GDCM (MGDCM) method is proposed [84], which presents more robust performance and ability to capture equilibrium paths with high curvature. In this

chapter, MGDCM path-following algorithm is adopted to trace load-displacement curves. c) Stability points are important concepts closely related to energy dissipation ability of unit cell. One way to detect and compute critical points is through the bi-section method where the sign of the diagonals of tangent stiffness matrix need to be monitored. However, convergence rate is slow for bi-section method. An efficient way to compute the singular points using extended system is proposed in Ref. [85] and the detailed implementation procedure can be found in Ref. [86]. However, Hessian matrix becomes ill-conditioned when the solution point approaches the critical point. To overcome this inherent difficulty, a modified solution technique for extended system based on rank-one updated algorithm is proposed by [86] to improve the condition number of tangent stiffness. Here, we apply extended system to determine the critical points.

2.4 Two-Dimensional Geometric Projection based on Heaviside Function

To controlling the structural complexity of an optimal design, a new density projection algorithm is described in this section to explicit describe and control geometric shape. Considering requirement of practical manufacturing, optimal design with controllable structural complexity is preferred such as bars or beams. Actually, several methods were reported for controlling the complexity in topology optimization design such as Norato.et al [15, 18] and Tortorelli.et al [20]. However, there still exist some weakness such as generating reasonable initial configuration and avoiding exceeding material 0-1 bounds at local regions. To address above challenges, an alternative geometric mapping method is proposed in this chapter as following. The design is defined by a set of line segments, which control the density distribution using Heaviside Function. Each line segment is parameterized by the location of two end points. The width of the line segment

is determined by parameter w in Heaviside Function. The minimum distance from any point $\boldsymbol{p}$ in design domain to line segment is defined as following [87],

$$\boldsymbol{d}(\boldsymbol{x_L}, \boldsymbol{x_R}, \boldsymbol{p}) = \begin{cases} \|\boldsymbol{b}\| \ \ \boldsymbol{if}\ \boldsymbol{a}\cdot\boldsymbol{b} \le \boldsymbol{0} \\ \|\boldsymbol{g}\| \ \ \boldsymbol{if}\ \boldsymbol{0} < \boldsymbol{a}\cdot\boldsymbol{b} < \boldsymbol{a}\cdot\boldsymbol{a} \\ \|\boldsymbol{e}\| \ \ \boldsymbol{if}\ \boldsymbol{a}\cdot\boldsymbol{b} > \boldsymbol{a}\cdot\boldsymbol{a} \end{cases} \tag{2.5}$$

with

$$\begin{cases} \boldsymbol{a} = \boldsymbol{x_L} - \boldsymbol{x_R} \\ \boldsymbol{b} = \boldsymbol{p} - \boldsymbol{x_R} \\ \boldsymbol{e} = \boldsymbol{p} - \boldsymbol{x_L} \\ \boldsymbol{g} = \left[\boldsymbol{I} - \frac{\boldsymbol{1}}{\|\boldsymbol{a}\|}\boldsymbol{a}\otimes\boldsymbol{a}\right]\boldsymbol{b} \end{cases} \tag{2.6}$$

where the operator $\|\cdot\|$ represents the Euclidean 2-norm, and $\otimes$ denotes Kronecker product of two matrices. The geometric representation of above vectors is demonstrated in Figure 2.2. To illustrate the definition of minimum distance, the minimum distance $\boldsymbol{d}$ from a point on a circle to a line segment is plotted in blue lines as shown in Figure 2.3.

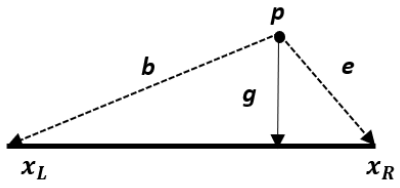

Figure 2.2 Geometry representation

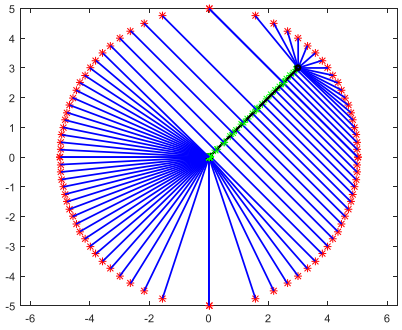

Figure 2.3 Minimum distance

To perform topology optimization algorithm on a fixed grid, geometric projection from line segments to a density field is achieved by a smoothed Heaviside function, stated as,

$$\rho = \frac{1}{2}(1 + \tanh(\beta(w - d))\,\bar{\bar{\rho}} + \rho_{min} \tag{2.7}$$

where $\bar{\bar{\rho}}$ denotes density of the segment, and the segment can be considered as non-existent if $\bar{\bar{\rho}} = 0$. w is a threshold used to determine the width of projection domain and parameter β determines the properties of density transition region. Parameter β have significant effects on boundary of geometry projection as shown in Figure 2.4. Increasing value of β makes boundary become more distinct, and width of geometry projection is determined by w as plotted in Figure 2.5. ρ_{min} is a small non-negative value. Obviously, discrete geometric component is successfully represented by projection based on Heaviside function, which is a more direct approach to define geometry projection compared to the method proposed by Totorelli [20].

(a) $\beta = 1$ (b) $\beta = 5$ (c) $\beta = 10$

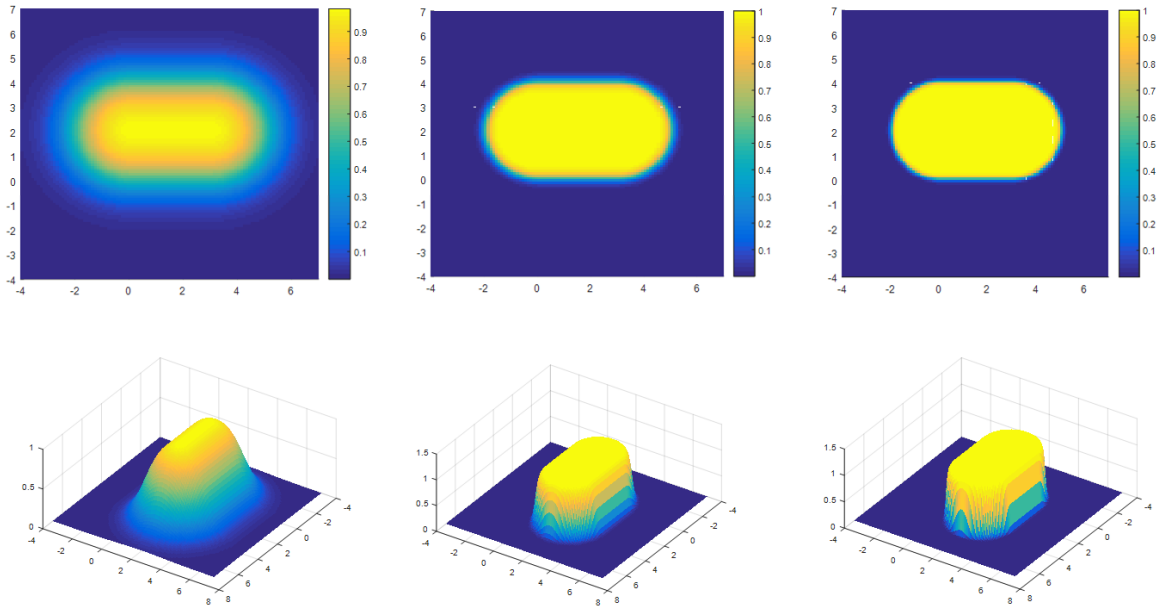

Figure 2.4 The effect of parameter β on geometry projection (a) $\beta = 1$ (b) $\beta = 5$ (c) $\beta = 1$

(a) $w = 0.5$ (b) $w = 1$ (c) $w = 1.5$

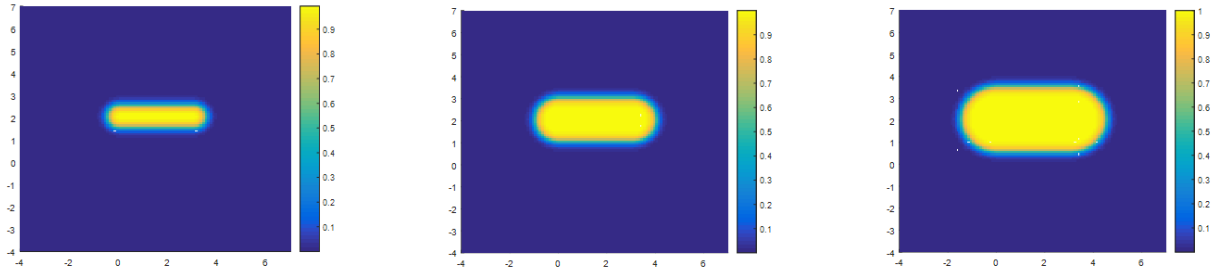

Figure 2.5 The effect of parameter w on geometry projection (a) $w = 0.5$ (b) $w = 1$ (c) $w = 1.5$

Above section describes the projection from a single discrete component to density layout. For multiple discrete components, composite density needs to be defined as following,

$$\widetilde{\rho_j} = \max \rho_{ij} \ \ (i = 1 \dots n, j = 1 \dots m) \tag{2.8}$$

where n denotes number of components, and m represents total element number. Due to the non-differentiable nature of maximum function, p-norm formulation is applied to achieve smooth approximation of maximum function. Thus, the composite density is defined as,

$$\widetilde{\rho_j} = \left(\sum_{i=1}^{n} {\rho_{ij}}^{p}\right)^{1/p} \tag{2.9}$$

Note that if p tends to $+\infty$, the value in p-norm formulation above approximates the maximum of density ρ_{ij} ,while , for finite p value, p-norm function always exceeds the maximum density. As mentioned by Ref [20], composite density may exceed the 1. However, for two-dimension design, it is necessary to restrict composite density between 0 and 1. To overcome this numerical issue, a special density projection (SDP) function is introduced as following,

$$\overline{\rho_j} = \tanh(3\widetilde{\rho_j}) \tag{2.10}$$

The curve property of above projection function is shown in Figure 2.6. Compared to Ref [20], differentiability during optimization is guaranteed using SDP function instead of applying

discontinuous minimum function to avoid artificially high stiffness ($\widetilde{\rho_j} > 1$) at local regions. Using p-norm function combined with SDP can effectively constrain the composite density between 0 and 1, the similar numerical approach applying lower bound KS (LKS) function can be found in Ref [33].

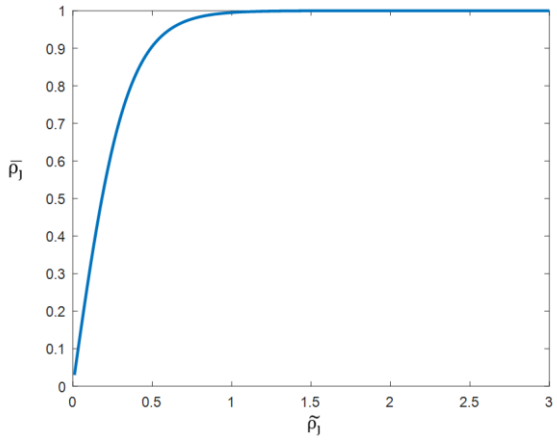

Figure 2.6 Curve of special density projection function

2.5 Sensitivity Analysis of Geometry Projection

To solve the topology optimization based on discrete geometric components, the sensitivity of the geometry projection with respect to the composite density is required. The chain rule is applied as following,

$$\frac{\partial \bar{\rho}_j}{\partial \mathbf{X}} = \frac{\partial \bar{\rho}_j}{\partial \tilde{\rho}_j} \frac{\partial \tilde{\rho}_j}{\partial \rho_{ij}} \frac{\partial \rho_{ij}}{\partial \mathbf{X}} \tag{2.11}$$

where $\mathbf{X} = [\boldsymbol{x_L}, \boldsymbol{x_R}, \bar{\bar{\rho}}, w]$. The first two terms in above equations are given by,

$$\frac{\partial \bar{\rho}_j}{\partial \tilde{\rho}_j} = 3 - 3\tanh\left(3\tilde{\rho}_j\right)^2 \tag{2.12}$$

$$\frac{\partial \tilde{\rho}_j}{\partial \rho_{ij}} = \left(\sum_{i=1}^{n} {\rho_{ij}}^p\right)^{\frac{1}{p}-1} \left(\sum_{i=1}^{n} {\rho_{ij}}^{p-1}\right) \tag{2.13}$$

k denotes the index of discrete geometry component. where δ_{ik} is Kronecker delta, defined as:

$$\begin{cases}\delta_{ik} = 1 \; if \; i = k \\ \delta_{ik} = 0 \; if \; i \neq k\end{cases} \tag{2.14}$$

the derivative of $\widetilde{\rho_j}$ with respect to the end points $\boldsymbol{x_L}$ and $\boldsymbol{x_R}$ is given by,

$$\frac{\partial \widetilde{\rho_j}}{\partial \boldsymbol{x_L}} = \left(\sum_{i=1}^{n} {\rho_{ij}}^{p}\right)^{\frac{1}{p}-1} \left(\sum_{i=1}^{n} {\rho_{ij}}^{p-1} \frac{\partial \rho_{ij}}{\partial d_{ij}}\right) \frac{\partial d_{ij}}{\partial \boldsymbol{x_L}} \tag{2.15}$$

$$\frac{\partial \widetilde{\rho_j}}{\partial \boldsymbol{x_R}} = \left(\sum_{i=1}^{n} {\rho_{ij}}^{p}\right)^{\frac{1}{p}-1} \left(\sum_{i=1}^{n} {\rho_{ij}}^{p-1} \frac{\partial \rho_{ij}}{\partial d_{ij}}\right) \frac{\partial d_{ij}}{\partial \boldsymbol{x_R}} \tag{2.16}$$

Then sensitivities of the minimum distance d with respect to end points is given by,

$$\frac{\partial d}{\partial \boldsymbol{x_L}} = \begin{cases} -\frac{\boldsymbol{b}}{\|\boldsymbol{b}\|} \;\; if \; \boldsymbol{a}\cdot\boldsymbol{b} \leq 0 \\ \frac{1}{\|\boldsymbol{g}\|}\left[\frac{1}{\|\boldsymbol{a}\|^2}((\boldsymbol{a}\otimes\boldsymbol{b})^T + (\boldsymbol{a}\cdot\boldsymbol{b})\boldsymbol{I}) - \boldsymbol{I}\right]\boldsymbol{g} \;\; if \; 0 < \boldsymbol{a}\cdot\boldsymbol{b} \leq \boldsymbol{a}\cdot\boldsymbol{a} \\ \boldsymbol{0} \;\; if \; \boldsymbol{a}\cdot\boldsymbol{b} \geq \boldsymbol{a}\cdot\boldsymbol{a} \end{cases} \tag{2.17}$$

and

$$\frac{\partial d}{\partial \boldsymbol{x_R}} = \begin{cases} -\frac{\boldsymbol{b}}{\|\boldsymbol{b}\|} \;\; if \; \boldsymbol{a}\cdot\boldsymbol{b} \leq 0 \\ -\frac{1}{\|\boldsymbol{g}\|\|\boldsymbol{a}\|^2}((\boldsymbol{a}\otimes\boldsymbol{b})^T + (\boldsymbol{a}\cdot\boldsymbol{b})\boldsymbol{I})\boldsymbol{g} \;\; if \; 0 < \boldsymbol{a}\cdot\boldsymbol{b} \leq \boldsymbol{a}\cdot\boldsymbol{a} \\ -\frac{\boldsymbol{e}}{\|\boldsymbol{e}\|} \;\; if \; \boldsymbol{a}\cdot\boldsymbol{b} \geq \boldsymbol{a}\cdot\boldsymbol{a} \end{cases} \tag{2.18}$$

As mentioned by Ref. [15], the sensitivities of signed distance above are continuous across the branches of the function.

2.6 Initial Guess of Geometric Component Distribution

As depicted by previous literatures [15], random initial guess of geometry component is chosen as initial value of optimization progress. It is feasible to use random initial distribution for linear problem. One weakness of random initialization is that the ends of geometry component

always cannot connect to other components. Thus, there exist gaps between geometry components, which is undesirable for solving geometry nonlinear problem in that excessive mesh distortion may happen in the gap region during FEM analysis. Hence it is essential to find an initial layout which should be a connected path of geometry components between loads and the boundary conditions. As described by Ref [19], the value of failure constraint is highly sensitive to a small change of geometric component design variables, and some worse initial values leads to unreasonable optimal design. Thus, a reasonable initial value of design variables is of great significance for convergence of optimization progress. However, how to construct an initial connected design is still a tricky problem, especially for nonlinear TO problem. From our numerical experiments, a density based optimal design can work as a guidance for geometric component initialization. Inspired by this point, an identification process is proposed in this chapter to construct a reasonable initial values of design variables. This identification progress can be divided into two parts. This first part is topology optimization using density-based methods, a coarse layout should be achieved, which can work as a design guidance for TO with geometric component. It is worth to mention that there is no need to reach an ideal 0-1 solution for density based TO. A coarse layout with a large amount of intermediate density during optimization progress is enough to work as guidance. This is a computational inexpensive procedure and limit iterations are enough for optimization progress. The second part is an identification progress, which can be regarded as a sub optimization problem. The sub optimization problem is formulated as follows,

$$minimize \quad \sum(\bar{\bar{X}}_G(\boldsymbol{x_L}, \boldsymbol{x_R}, \bar{\bar{\rho}}, w) - X_I)^2 \tag{2.19}$$

where parameters $\boldsymbol{x_L}, \boldsymbol{x_R}, \overline{\overline{\rho}}, w$ are design variables of geometric components. $\overline{\overline{X}}_G$ denotes density projection from geometric components. X_I represents objective density from density-based optimization results. Hence, this cost function can be explained as finding an optimal initial layout of geometric component to minimize the difference between geometry projection with desired density distribution from density-based optimal results. Due to the limited parameters needed to be identified, sequential quadratic programming (SQP) method [88] is implemented here to find a local minimum of cost function. Detailed description of identification progress will be demonstrated in numerical examples.

2.7 A Comparison between Geometry Projection Algorithm and Traditional Density-based Method

Geometry projection algorithm is a new explicit geometry control method, which is capable of giving an explicit control of the minimum structural length scale in a very straightforward way with use of some purely geometric constraints. From one aspect, geometry projection algorithm is mesh independent, which means that design variables are not dependent on mesh density and adaptive mesh refinement is direct to implement without density mapping. From computational complexity aspect, geometry projection algorithm belongs to model reduction category to some extent. Clearly, the design variables reduce significantly after projection, which can be solved by regular small-scale optimization solver (e.g. sequential quadratic programming [89]) instead of implementing large-scale optimization algorithm such as MMA. This also enables highly resolved finite element analysis without increasing the dimension of the non-linear programming problem, a desirable property. In such a situation, reduction of design variables is able to improve the

efficiency of sensitivity computation progress significantly. Besides, the geometric projection method can produce truss-like material layout, which is ideal for additive manufacturing because final optimized layouts do not contain small unfavorable features, e.g. local complicated curves. The minimum length of optimal design can be directly controlled by parameters of Heaviside function. The Heaviside function-based geometric projection method proposed in this article can also be applicable to metal design. From the manufacturing point for metal, the processes that require supports, can self-support so long as the overhang is above a particular angle to the horizontal. Therefore, modifying the design to make it self-support shows a great potential in reduction of material usage. Apparently, using discrete bars to represent density field is promising for self-support designs, because the angle of every component is convenient to handle by adding angle constraint for each component in optimization progress, this part will be studied further in the future.

2.8 Mathematical Formulation for Energy Dissipation Design based on Negative Stiffness Behavior

To formulate the optimization problem for high energy dissipative metamaterials, a brief review of mechanical behavior of a simple negative stiffness structures is provided here. Considering a phase transforming chain, whose unit cell is composed by a sinusoidal beam. Each sinusoidal beam in a chain can work as a compliant bi-stable mechanism. The characteristic normalized force-displacement response of one unit cell is shown in Figure 2.7 in blue solid line, where the force-displacement curve of unstable element contains a spinodal region (Regime 2) due to non-monotonicity of stiffness. Note that force-displacement response is approximated by a

linear response. Considering a chain containing several unit cells, the chain presents hysteresis behavior and mechanical energy will dissipate during one loading and unloading circle. In fact, mechanical behavior of the chain under displacement control changes significantly with change of element number, and the maximum possible dissipation per element in a chain equals the energy dissipation achieved by applying force control [90]. As shown in Figure 2.7, the area encompassed by the red dash curve represents the maximum energy dissipation per element under displacement control if a chain containing infinite unit cells, named as the theoretical absorption capacity [90].

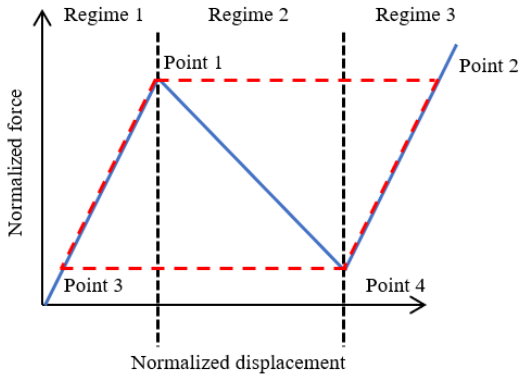

Figure 2.7 Mechanical response of a basic cell

Theoretical energy absorption capacity is a key point for material design due to unit cell being far smaller than the macro structural length scale. For real snap-through structures, mechanical response is a curve (see numerical examples) and the exact mathematical description of enclosed area is difficult to define for a robust topology optimization algorithm. A simplified expression is thus applied by approximating the enclosed area by a trapezoid defined by four points on the red curve as shown in Figure 2.7. Note that Point 1 is the instability point during loading and Point 2 is the point after the structure snaps through to. Point 3 is the instability point during unloading, while Point 4 is the point after snapping through. The area of a trapezoid can be expressed as,

$$\Omega = (d_2 - d_1 + d_3 - d_4) \cdot (\lambda_1 - \lambda_3) \tag{2.20}$$

Above equation is the cost function in numerical examples.

Material softening phenomenon means that a deformed structure is no longer able to resist additional force and the reversible capacity is destroyed. Although materials such as some special rubbers [91] can resist even more than 300% strain without softening, the capacity of most other soft material to endure large strain is still very limited. When designing bi-stable structures, traditional continuum-based hyperelastic models do not include material strain energy bound which leads to unbounded energy accumulation. Evidently, this is unphysical and may result in unreasonable engineering design when using traditional hyperelastic materials. Considering that large strain is unavoidable during snap through behavior, failure criterion plays a key role in simulating the material to avoid unreasonable design, as the energy of real hyperelastic material needs to be constrained for design and may be defined as material failure energy. Such a limiter is a direct criterion to measure recoverability of material. Actually, different failure criteria is available for hyperelastic materials: (1) the maximum principal stress (2) the maximum principal stretch (3) the maximum shear stress (4) von Mises stress and (5) the strain energy. As experiment implemented by K.Y.Volokh [92], the strain energy is almost constant for the failure states under different loads and tension tests compared to other failure criteria, and von-Mises stress shows a wider range of scattering compared to strain energy. Thus, using strain energy as failure criteria is more accurate and reasonable for measuring failure of soft material. Due to the local nature of the element strain energy, it is difficult to optimize each material point due to high computational cost of matrix inversion. One effective method is to use the p-norm function [93] to integrate each element energy into one objective. Element strain energy needs to be penalized with ρ_i^q to avoid

the singularity phenomenon when element density approaches zero, see Ref. [93] by Holmberg for a detailed discussion. The strain energy in p-norm form can be expressed by:

$$E_{PN} = \left[\frac{1}{N}\sum_{i=1}^{N}(\gamma_i \rho_i^q E_i(\boldsymbol{x}))^p\right]^{\frac{1}{p}} \tag{2.21}$$

where γ_i is an interpolation factor, N is element number of the whole model, and $E_i$is strain energy for each element. Note that the energy interpolation scheme introduced by Wang.et al [80] indicates that energy for the whole structure is blended with nonlinear and linear parts. For low density region, the energy of elements is obtained based on linear theory, while the objective function related to hyperelastic element strain energy should exclude linear energy part. Thus, removing energy contributions from these linear elements is necessary, and hence interpolation factor γ_i is used to multiply to the element strain energy. More details regarding interpolation factor γ_i can be found in Ref. [80]. It is essential to note that the failure constraints at two limit points (peaks) are applied to design bi-stable element instead of monitoring strain energy at each equilibrium state, which is almost impossible for implementation. In general, we can choose several equilibrium states as shown in Figure 2.8 to apply failure constraint so that failure criteria is satisfied at these states. The strain energy in p-norm form at state j is written as θ_j. In this chapter, we apply failure criteria at two limit points, which can be easily extended to multiple equilibrium states.

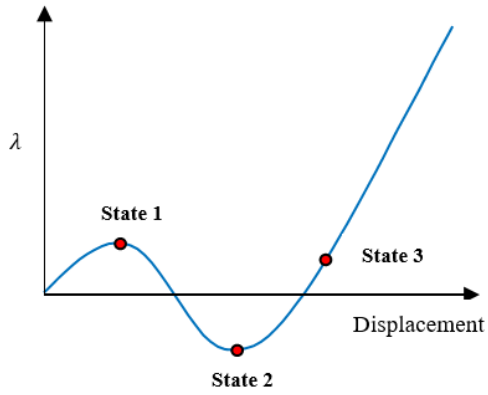

Figure 2.8 Strain energy constraint applied at different equilibrium state under displacement control

2.9 Optimization Formulation

The above algorithm requires that an initial snap-through behavior is needed so that limit points exist. For a regular design domain, an initial snap through behavior does not exist, like a square domain. Thus, the priority is that modifying the force-displacement curve through topology optimization so that a negative stiffness behavior occurs. One way to realize bi-stable behavior for arbitrary domain is through controlling two points on the displacement-force curve as described by Ref [21]. Therefore, the optimization progress can be divided into two independent stages. The first stage modifies the displacement-force curve to show negative stiffness, the second stage, which is based on the final design of stage I, optimize material layout to maximize energy dissipation ability. Once the snap-through behavior appears, the stage I will stop. The stage II starts based on the result inherited from the optimized layout of stage I. The stopping criteria for the stage II is the change of objective value less than 1%. Thus, the optimization problem is separated into two parts, the first part is to tailor the material to shown snap-through behavior. The optimization problem in the first part is formulated as described in Ref [21]. More details can be

found in Ref [21]. Once the structures present snap-through behavior. The second optimization part is formulated as follows,

$$Maximize \;\; \Omega = (d_2 - d_1 + d_3 - d_4) \cdot (\lambda_1 - \lambda_3)$$
$$subject\ to \begin{cases} \frac{V(x)}{|\Omega|} - v_f^* \leq 0 \\ c\left[\frac{1}{M}\sum_{j=1}^{M}(\theta_j)^p\right]^{\frac{1}{p}} < 1 \quad (at\ limit\ points) \end{cases} \tag{2.22}$$

Note that cost function is area of trapezoid determined by four points as described in Figure 2.7. Here d denotes displacement and λ is force factor. Subscript number i $(i = 1,2,3,4)$ represents index of point. θ_j in the constraint denotes the p-norm strain energy at state j.

$$\theta_j = \left[\frac{1}{N}\sum_{i=1}^{N}\left(\frac{E_i(\boldsymbol{x})}{\bar{E}}\right)^p\right]^{\frac{1}{p}} \tag{2.23}$$

where $\bar{E}$ is the strain energy limit and p is p-norm factor. c is an adaption parameter, which is computed from the previous optimization iteration. Details description of the parameter c is found in Ref. [93]. v_f^* and $|\Omega|$ represent prescribed volume fraction and area of design domain. Gradient-based optimization method is employed here to solve the optimization problem above efficiently by deriving accurate sensitivities of the objective function and constraints.

Identifying the initial distribution of geometry component is an essential procedure for topology optimization. This procedure is described in detail in above section. With the initial design variable of geometry component, Heaviside function is applied to project the geometry components to the density field. Nonlinear finite element is formulated based on energy interpolation scheme, and the path-following algorithm is realized to trace the force-displacement curve. Limit points are directly computed through extended system with nearby initial points obtained by path-following algorithm. With the information from limit points, the value of cost function and constraints is evaluated, and sensitivity based on adjoint method is obtained. Hence, the design variable can be updated by the sensitivity information using MMA algorithm [94]. The

flow chart of discrete geometry component optimization algorithm is shown in Figure 2.9. The optimization algorithm can be divided into three stages. Stage I apply traditional density-based method to obtain a coarse design that presents snap-through behavior. An inverse sub-optimization problem is achieved to fit geometric components to the material layout obtained in stage I. The final stage use density representation algorithm proposed in this chapter to maximize energy dissipation considering failure constraint in prescribed domain. The details of algorithm implementation are demonstrated in Figure 2.10.

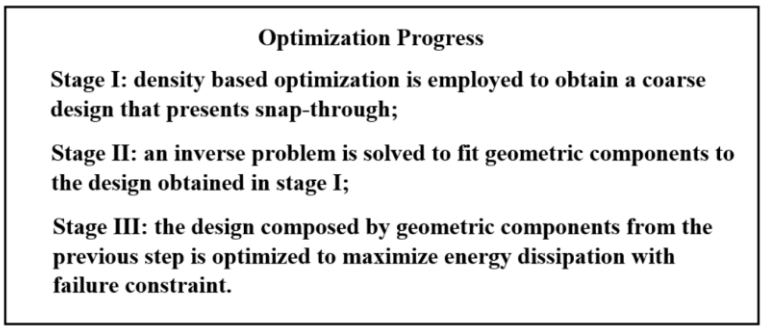

Figure 2.9 Flow chart of optimization algorithm

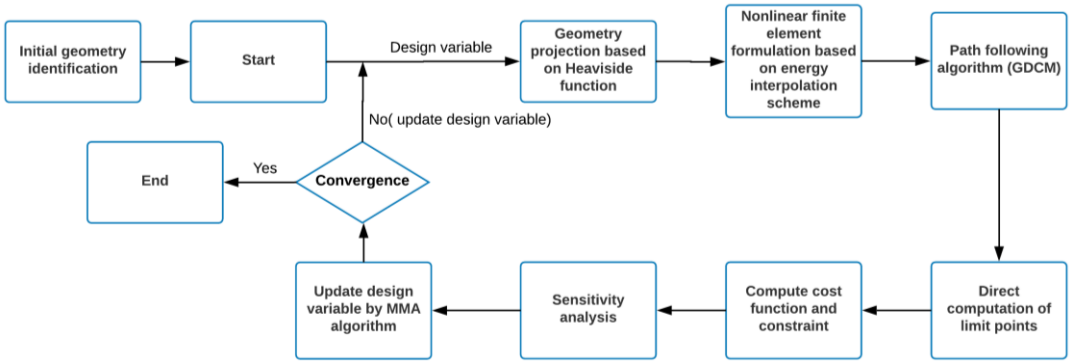

Figure 2.10 Details of algorithm implementation

2.10 Numerical Examples

In this section, three cases are demonstrated to present the effectiveness of our algorithm. In these three cases, material failure is considered in the design as a constraint to affect the material layout. The initial geometry component distribution is identified from density based numerical results. The method of moving asymptotes (MMA) [94] is applied to solve optimization problem, which constructs and solves a sequence of convex approximation sub-problem based on sensitivities during optimization progress to update the design point. Note that the parameters used in these cases are dimensionless. The penalty parameter and p-norm factor are chosen as $penal = 3$ and $p = 10$. Plane strain assumption is applied in analysis and design.

2.10.1 Slender Beam Design without Failure Constraint

A slender beam structure is shown in Figure 2.11, which is clamped at both ends and a transverse concentrate force is applied at the center of top line. Due to symmetry of design domain and boundary conditions, half domain is chosen to design. Design domain is discretized by 30×100 4-node bilinear elements. Soft material mechanical behavior is described by the Mooney-Rivlin model with $A_{10} = 34$, $A_{01} = 5.8$ and $K = 2000$. The volume constraint in the optimization is 30% of the design domain. In the first numerical case, the objective is maximizing the energy dissipation capacity, where material failure constraint is not taken into consideration. Before applying TO method with discrete geometry component, an initial material layout should work as a guidance to generate initial design variable of discrete geometry component. Hence a density-based topology optimization progress is implemented to achieve snap through behavior. This progress contains two stages, the first stage should be redistributing material within design

domain to generate a bi-stable structure, named as stage I. Once a snap through behavior presents during optimization progress, stage II started with initial density distribution inherited from final design of stage I. The solution at the end of stage I is shown in Figure 2.12. The inverse sub-optimization problem is resolved using SQP (sequential quadratic programming) method, and identified geometric component is plotted in Figure 2.14. The identification progress converges after 160 iterations as shown in Figure 2.13 . Note that the design domain is made of 5 geometry components, and the projection parameter w is constrained by $1 < w < 2$. The optimized material layout is presented in Figure 2.15. To make a comparison with traditional density-based method, the material layout obtained by density-based method is shown in Figure 2.17. It is worth to mention that the optimized result using our proposed method has simple geometry shape, and the border of the material layout is composed of straight line instead of complex curves. This simple material layout is better for manufacturing in engineering. Moreover, through constraining the width of geometry component, the minimum length of final optimized design can be directly controlled. The mechanical response of initial identified configuration is presented in Figure 2.16 (red line), while the response of optimized material layout is shown in blue line. Obviously, the energy dissipation capacity increases significantly after optimization.

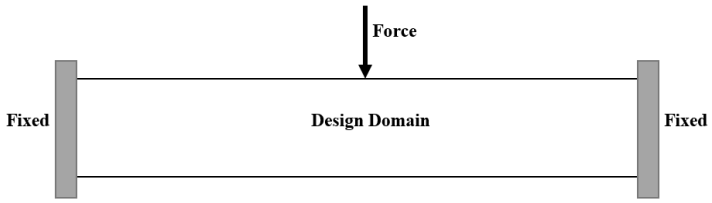

Figure 2.11 Slender beam design domain

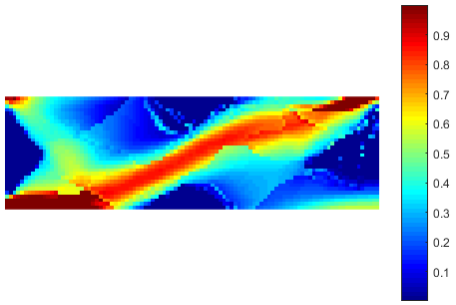

Figure 2.12 Solution at the end of Stage I

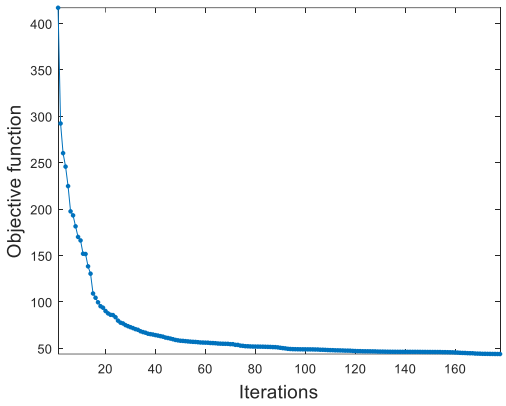

Figure 2.13 Identification progress ($1 < w_{bar} < 2$)

(a) Density distribution (b) Geometric component distribution

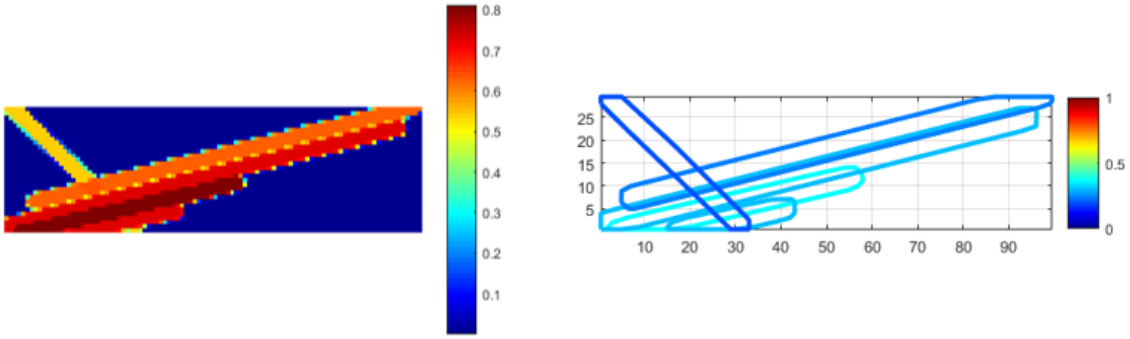

Figure 2.14 Initial discrete component distribution (a) Density distribution (b) Geometric component distribution

(a) Density distribution (b) Geometric component distribution

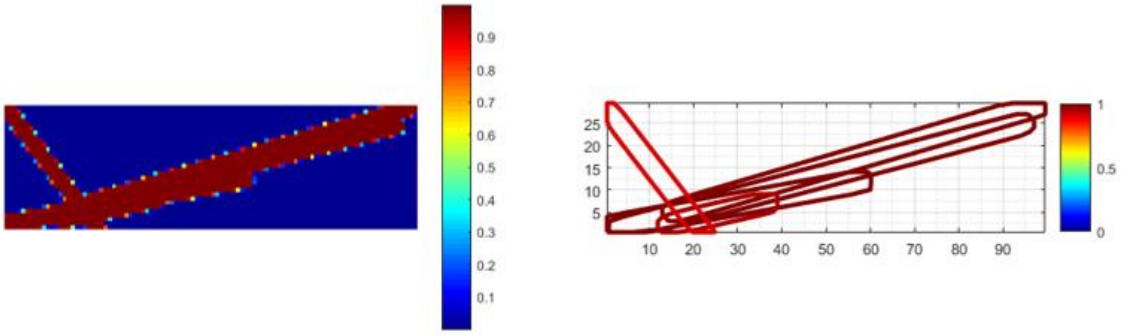

Figure 2.15 Discrete component distribution (component number: 5) (a) Density distribution (b) Geometric component distribution ($1 < w_{bar} < 2$)

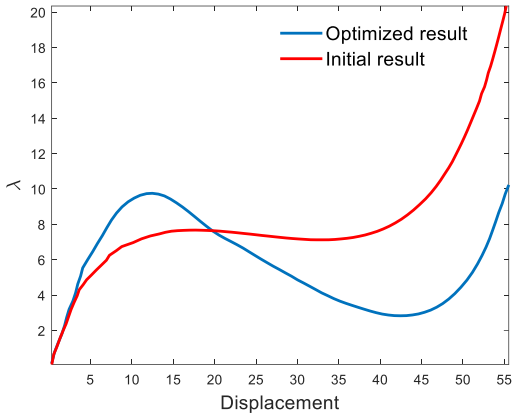

Figure 2.16 Force-displacement curve

Figure 2.17 Optimized results based on traditional density-based method

2.10.2 Slender Beam Design with Failure Constraint

In this numerical example, material softening phenomenon happens at 20% strain under uniaxial tension, which corresponding to failure strain energy value around 4. A solution at the end of stage I is plotted in Figure 2.18 with intermediate density area. It is worth to mention that the density layout shown in Figure 2.18 presents snap through behavior. The volume constraint in the optimization is 40% of the design domain. This material layout will work as a desired density objective to guide the initial layout of geometry component. Sequential quadratic programming (SQP) method is implemented here to find a local minimum of cost function

The initial identified geometry component is presented in Figure 2.19, and the design domain is made of 15 geometry components. Note that the initial geometry components have already presented negative stiffness mechanical properties after numerical testing. Thus, optimization progress for the discrete geometry component can directly skip to the second stage with present initial design variables. To achieve the geometry control of final numerical results, the projection parameter w is constrained by $w < 2$, and location parameters $\boldsymbol{x_R}$ and $\boldsymbol{x_L}$ are constrained by the boundary of slender beam design. The optimal geometry component layout is shown in Figure 2.20. After around 110 iterations, the optimization progress converges as plotted in Figure 2.22, where the red line represents value of strain energy in p-norm formulation. Note that the constraint of strain energy will converge to 1 after optimization, which means the maximum element strain energy in the design domain reaches failure energy. The evolution of optimization progress is presented in Figure 2.21. It is worth to mention that our objective is to maximize dissipation energy, which is equivalent to minimize the negative value of energy dissipation. Therefore, we find that value of objective function is negative.

It can be clearly observed that the optimal layout has arched shape. When the structure moves downwards under external force, the arched shape begin to buckle. During this progress, the compression energy of the whole structure increases at first and then decreases faster than the bending energy. The components on the left and right side enhance stiffness of the overall structure, which results in a higher difference between two buckling forces at limit points and hence a higher theoretical energy absorption capacity. The force-displacement curve plotted in Figure 2.24, which finds that the force minimum located at the second stable point is positive, which means the structure can recover by itself without actively pulling it back. The deformation at two limit points are shown in Figure 2.23.

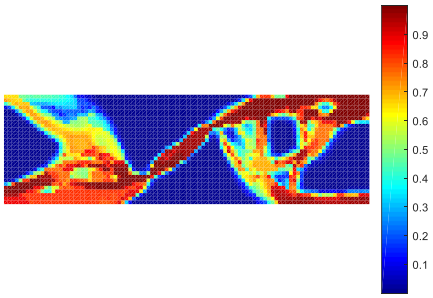

Figure 2.18 Solution at the end of Stage I

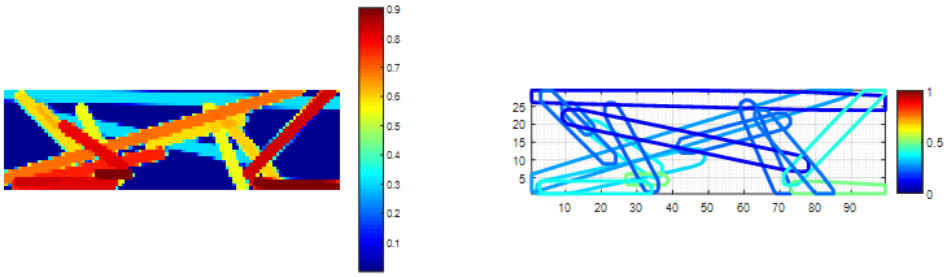

Figure 2.19 Initial geometry component layout

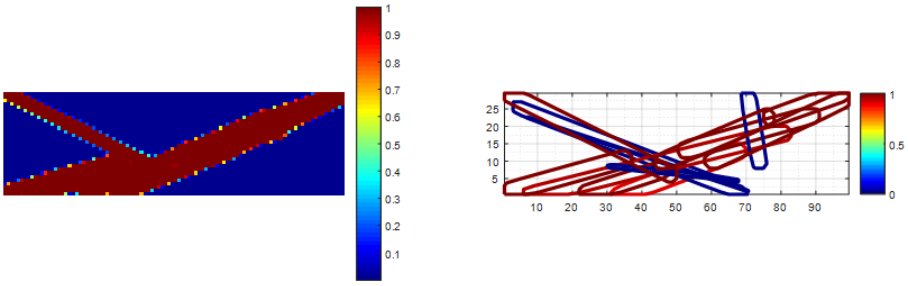

Figure 2.20 Optimized geometry component layout

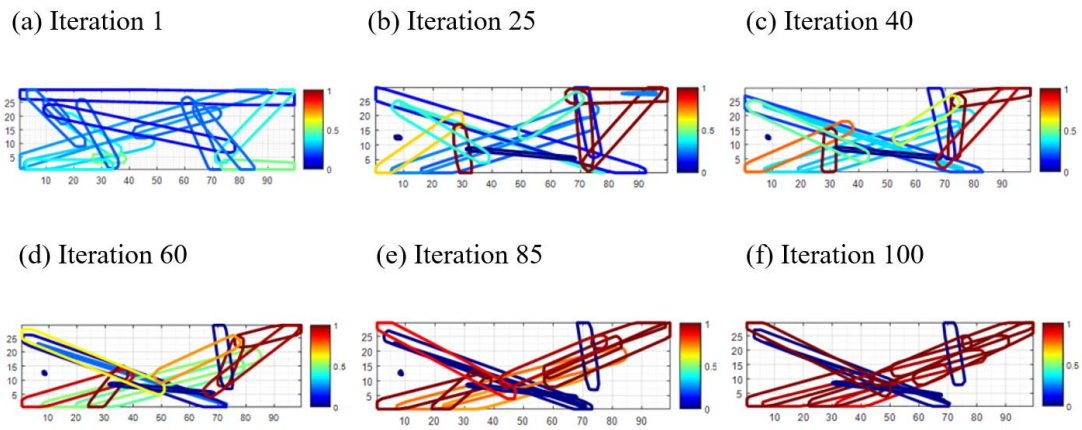

Figure 2.21 Evolution of optimization progress

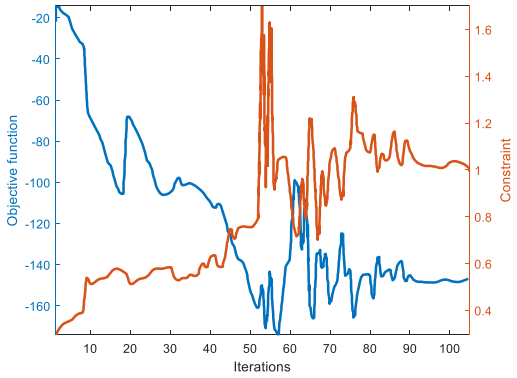

Figure 2.22 Convergence history

(a) First stable point (b) Second stable point

Figure 2.23 Deformation at two stable points: (a) First limit point and (b) Second limit point

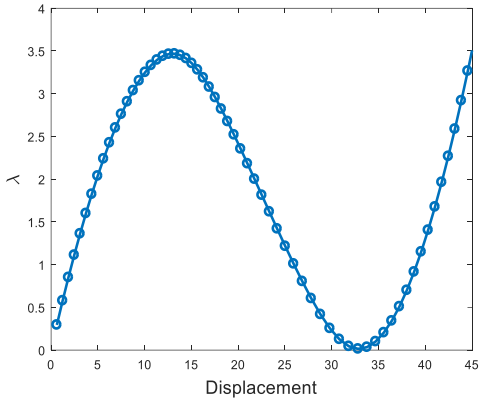

Figure 2.24 Force-displacement curve

2.11 Conclusions

In this chapter, extreme energy dissipation metamaterial design considering failure constraint through topology optimization algorithm is demonstrated in details. Approximation of theoretical energy absorption is formulated through mathematical expression and strict sensitivities are deducted by adjoint method. Material failure is measured by strain energy and p-norm formulation are utilized. To explicit control and express geometric shape, an alternative projection method is presented for continuum-based topology optimization made of geometric components. This geometric projection algorithm is completely based on a fixed grid and hence

inherit the advantages of density-based TO method. By applying the chain rule, the sensitivities with respect to geometry parameters are convenient to derive. This guarantees the application of gradient-based optimization frame with standard nonlinear programming algorithms. The density mapping algorithm in this article is based on Heaviside function, which is possessed of strong generality and can be extended to apply curved skeleton to control complex geometry shape in the future. Two typical cases are presented in detail, and truss-like optimal results are readily to achieve. Compared to ground structure methods, geometric projection method has more freedom to place and size the components. Note that the SDP function is introduced to resolve the issue that the density may exceed the upper limit 1 at overlapping region. From numerical results, method proposed in this article has the ability to remove redundant components, and identification progress is effective to find initial layout and construct connected load path between the load and boundary.

3.0 Topology Optimization Design of Stretchable Metamaterials with Bezier Skeleton Explicit Density (BSED) Representation Algorithm

3.1 Current Progress of Topology Optimization for Flexible Material Design

Stretchable electronics has been studied for almost 20 years and several novel applications ranging from bio-integrated devices to wearable technologies can be found. Demand for higher performing mechanical design raises new challenges in soft system designs. For instance, wearable electronics, which deals with complex, flexible and stretchable biological systems, require that artificial material to be able to exhibit high stretchability while retaining stiff to transfer loading. Unfortunately, conventional electronics made of silicon or polymers are rigid and brittle in nature and hence are not ideal for wearable electronics due to lacking the ability to stretch. A number of ground-breaking ideas have recently been proposed to achieve the above functional requirements such as (I) application of unconventional materials (e.g. hydrogel [95]) and (II) novel structures with new mechanical characteristics. In this chapter, we focus on designing new metamaterial to achieve certain functionality such as stretchability and compliance. With the advent of additive manufacturing technology, the ability to fabricate complicated geometries made of varies materials from metal to soft materials is possible. Thus, metamaterial design becomes an emerging field in research in that it may be utilized to generate novel material to satisfy the desired functional requirement. As reported in [96], some designed lattice structures made of metamaterials show ultrahigh reversible stretchability, which opens the door to design stretchable electronics. Compared to traditional metamaterial design optimization performed using linear finite element analysis, designing metamaterial with high stretchability requires considering geometrical and

material nonlinearity. Determining the effective homogenized properties of nonlinear materials at finite deformation is challenging and is an active field of research. Elastomer test [74], such as uniaxial tension, is one feasible method to determine effective properties of novel metamaterial. Similar to the methods applied in Ref. [97], three elastomer testing methods (uniaxial tension, equi-biaxial tension, pure shear) are applied in this chapter to evaluate effective material properties.

Traditional density-based method, where each element works as a design variable, always results in complex geometry with large number of small intricate features, while these small features are not amenable for manufacturability for AM or post-processing that can cause a loss in geometric accuracy. To address the above challenge, a new density field representation technique called the Bézier skeleton explicit density (BSED) representation scheme for topology optimization of stretchable metamaterials is proposed in this chapter for the first time. First, Bézier curves are widely used in computer graphics to produce curves which appear reasonably smooth at all scales and are employed in the proposed approach to describe the skeleton of the design being optimized so that the entire design is described by assigning the Bézier curve with certain thickness. The proposed approach ensures that the optimized design is smooth and concise, and can easily be manufactured by AM. Second, the density field is described by the Heaviside function defined on the Bézier curves in the optimization model. Compared to NURBS or B-spline based models, Bézier curves have fewer control parameters and hence are easier to manipulate for sensitivity derivation, especially for distance sensitivities. Due to its powerful curve fitting ability, using Bézier curve to represent density field allows exploring design space effectively and generating concise structures without any intricate small features at the borders. Furthermore, this density representation method is mesh independent and design variables are

reduced significantly so that optimization problem can be solved efficiently using small-scale optimization algorithms such as sequential quadratic programming.

3.2 Bezier Representation

To represent the skeleton based on curve segment, the so-called Bézier polygon is introduced. Every polynomial curve segment can be represented by Bézier polygon, where the curve segment lies in the convex hull of its Bézier polygon. Note that a Bézier curve is a parametric curve that uses Bernstein polynomials as a basis.

3.2.1 Bernstein Polynomials

The Bernstein polynomials of degree *n* is defined as follows,

$$B_i^n(u) = \binom{i}{n} u^i (1-u)^{n-i}, i = 0, \cdots, n \tag{3.1}$$

where

$$\binom{i}{n} = \frac{n!}{i!(n-i)!} \tag{3.2}$$

The Bernstein polynomials over $[0,1]$ of different degree n (4, 5, 6) are plotted in Figure 3.1.

(a) $n = 4$ (b) $n = 5$ (c) $n = 6$

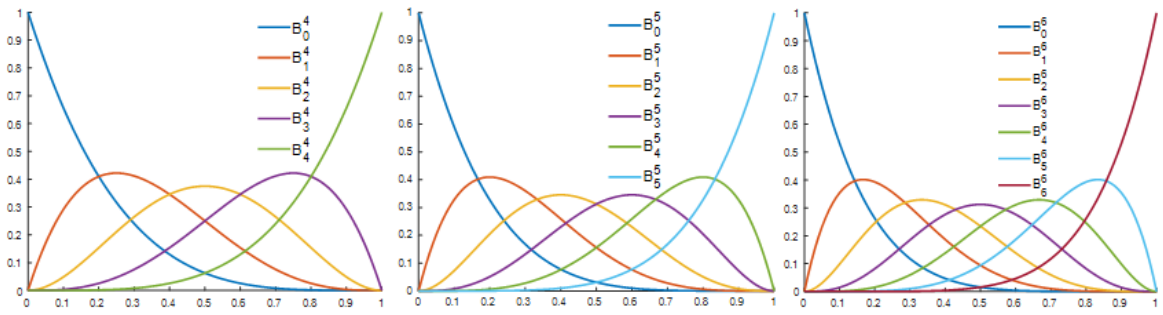

Figure 3.1 The Bernstein polynomials of degree *n* over [0, 1]: (a) *n*=4, (b) *n*=5, and (c) *n*=6.

All polynomials of degree less than n can be represented by Bernstein polynomials bases B_i^n, and hence the Bézier representation of polynomial curve $\boldsymbol{\chi}(u)$ is defined as:

$$\boldsymbol{\chi}(u) = \sum_{i=0}^{n} \boldsymbol{\psi_i} B_i^n(u) \tag{3.3}$$

where $\boldsymbol{\psi_i}$ is coefficient of the Bernstein polynomial bases. Using the following affine transformation

$$u = \alpha(1-t) + \gamma t, \;\; \alpha \neq \gamma, t \in [0,1] \tag{3.4}$$

the *n* th degree Bézier representation of polynomial curve can be written as:

$$\boldsymbol{\chi}(t) = \sum_{i=0}^{n} \boldsymbol{\chi_i} B_i^n(t) \tag{3.5}$$

where coefficients $\boldsymbol{\chi_i}$ are called Bézier points, which are the vertices of the Bézier polygon of curve $\boldsymbol{\chi}(t)$ over the interval $[a, b]$. Parameter t is called local parameter. A high-order Bézier curve segment with five control points is shown in Figure 3.2, where the blue dotted line and blue dots represent Bézier polygon and control points, respectively. Equation (3.5) can be expressed explicitly as follows:

$$\boldsymbol{\chi}(t) = \sum_{i=0}^{n} \binom{n}{i} (1-t)^{n-i} t^i \boldsymbol{\chi_i} \; (t \in [0,1]) \tag{3.6}$$

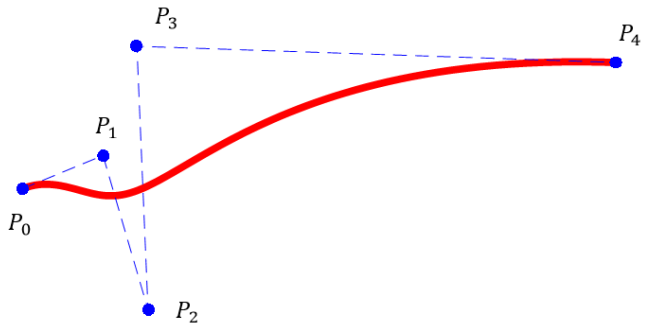

Figure 3.2 A high-order (*n*=4) curve segment with its Bézier polygon

3.3 Geometry Mapping based on Heaviside Function

The design is defined by a set of curved-based skeletons, which control the density distribution using the Heaviside function. Each curved-based skeleton is described by a single Bézier curve. The width of the skeleton is determined by a parameter w in the Heaviside function. The minimum distance from any point $\boldsymbol{p}$ in the design domain to the skeleton curve is demonstrated in Figure 3.3, where the blue solid line represents the minimum distance. Given a point $\boldsymbol{p}$ and a Bézier curve $\boldsymbol{\chi}(t)$, the point projection (minimum distance) can be described as finding a solution t_0, such that,

$$\|\boldsymbol{p} - \boldsymbol{\chi}(t_0)\| = min\{\|\boldsymbol{p} - \boldsymbol{\chi}(t)\|\},\ t \in [0,1] \tag{3.7}$$

If $t_0 \notin \{0.1\}$, the following necessary condition should be satisfied,

$$\boldsymbol{\chi}'(t_0) = 0 \tag{3.8}$$

where $\boldsymbol{\chi}'(t)$ denotes the derivative of $\boldsymbol{\chi}(t)$. Thus, the above point projection problem can be solved by a root-finding problem of a polynomial equation.

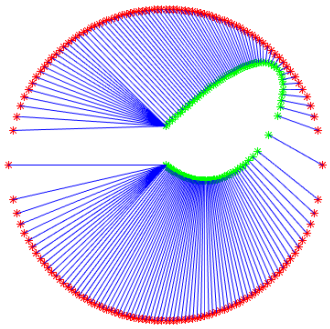

Figure 3.3 Points projection on a curved skeleton

To perform topology optimization algorithm on a fixed grid, geometric mapping from curved-based skeletons to a density field is achieved by a smoothed Heaviside function stated as:

$$\rho = \frac{1}{2}(1 + \tanh(\beta(w - d))\,\bar{\bar{\rho}} + \rho_{min} \tag{3.9}$$

where $\bar{\bar{\rho}}$ denotes density of the segment, and the segment can be considered as non-existent if $\bar{\bar{\rho}} = 0$. d represents the projection distance from centroid of grid to skeleton. w is a threshold used to determine the width of mapping domain and parameter β determines the properties of density transition region. The parameter β has significant effect on the boundary of geometric projection as shown in Figure 3.4. Increasing value of β makes boundary become more distinct, and width of geometry mapping is determined by w as plotted in Figure 3.5. ρ_{min} is a small non-negative value. Obviously, the thickness of skeleton can be modified directly through parameter w, which is able to control the minimum length of the optimized design.

(a) $\beta = 0.3$ (b) $\beta = 1$ (c) $\beta = 5$

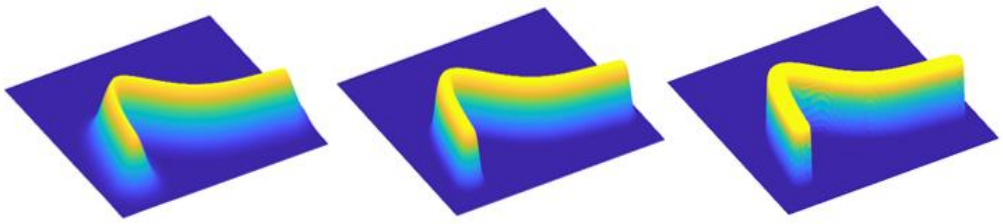

Figure 3.4 The effect of parameter β on density field (a) $\beta = 0.3$ (b) $\beta = 1$ (c) $\beta = 5$

Figure 3.5 The Effect of parameter w on geometry mapping: (a) $w = 1$, (b) $w = 3$, and (c) $w = 5$ for $\beta = 5$

To explicitly express geometry control based on curved skeleton, the relationship between curved skeleton and mapping density field is plotted in Figure 3.6. The boundary enveloping line of mapping density, which can effectively reflect the effect of skeleton thickness on density field. Note that the boundary enveloping line becomes non-smooth if mesh density of FEM is not enough.

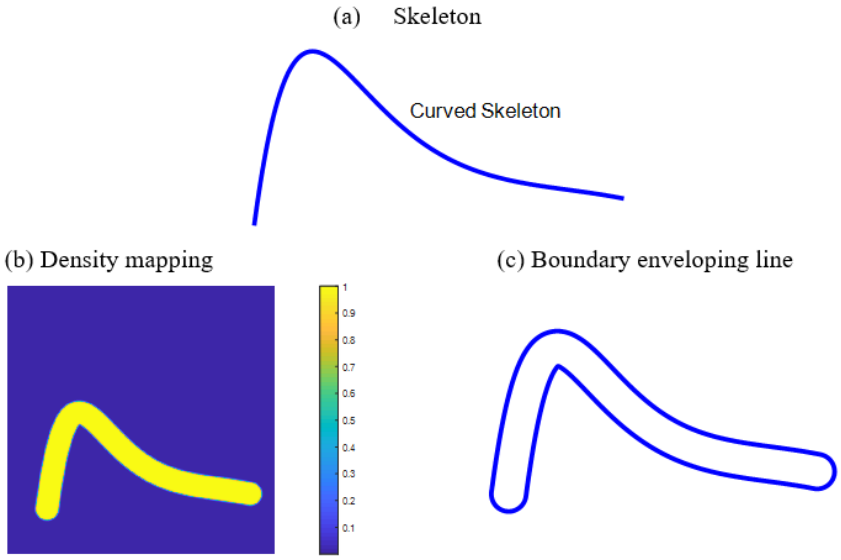

Figure 3.6 Geometry mapping from skeleton to density field (a) Skeleton, (b) Density mapping, and (c) Boundary enveloping line

3.4 Density Field Mapping of Multiple Curved Components

The previous section describes the mapping from a single component to density layout. For multiple curved components, composite density needs to be defined as follows:

$$\widetilde{\rho_j} = \max \rho_{ij} \ (i = 1,2 \cdots n, j = 1,2 \cdots m) \tag{3.10}$$

where n denotes number of components and m represents total element number. Due to the non-differentiable nature of maximum function, p-norm formulation is applied to achieve smooth approximation of the maximum function. Thus, the composite density is defined as:

$$\widetilde{\rho_j} = \left(\sum_{i=1}^{n} {\rho_{ij}}^{p}\right)^{1/p} \tag{3.11}$$

Note that if p tends to $+\infty$, the value in the p-norm formulation above approximates the maximum of density ρ_{ij}, while for finite p value, p-norm function always exceeds the maximum density. In this chapter, the value of p is set to be 10. As mentioned in Ref. [20], composite density may exceed unity. However, for two-dimension design, it is necessary to restrict composite density between 0 and 1. To overcome this numerical issue, a special density projection (SDP) function is introduced as follows:

$$\overline{\rho_j} = \tanh(3\widetilde{\rho_j}) \tag{3.12}$$

The curve property of the above projection function is shown in Figure 2.1. Compared to Ref. [20], differentiability during optimization is guaranteed using SDP function instead of applying discontinuous minimum function to avoid artificially high stiffness ($\widetilde{\rho_j} > 1$) at local regions. Note that $\overline{\rho_j}$, which is the actual input data for FEM analysis, represents the real physical density in this work.

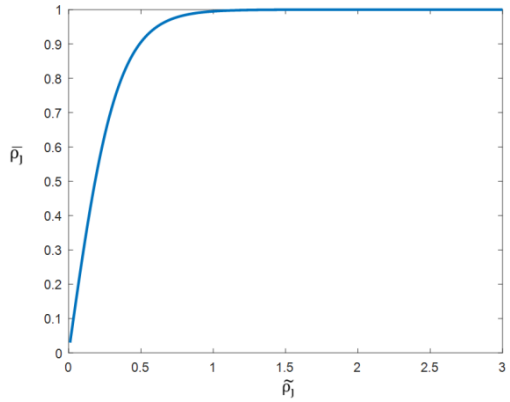

Figure 3.7 Property of special density projection function

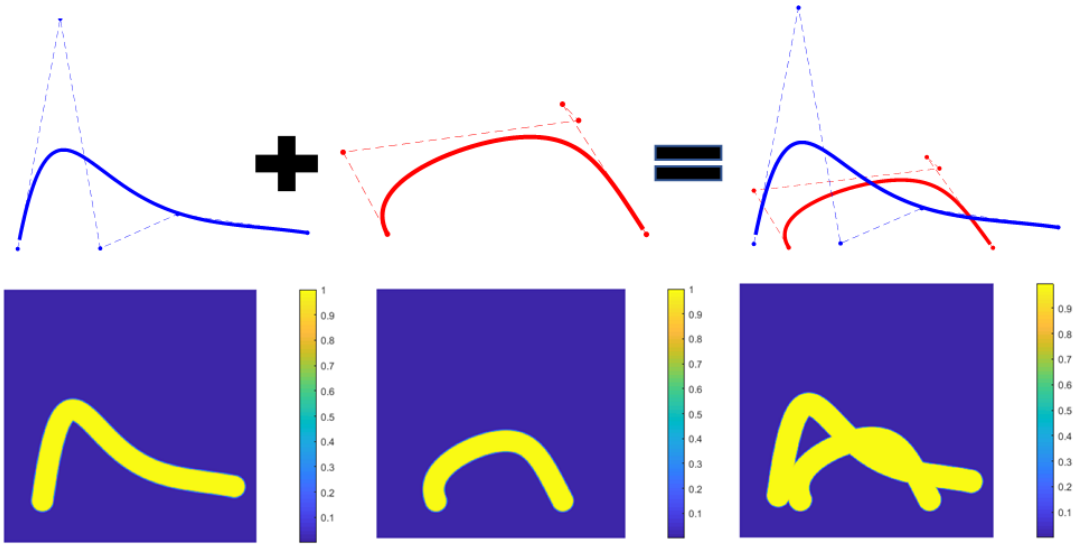

Figure 3.8 Density field mapping of two curved components ($w = 3, \beta = 5$)

3.5 Characterization of Material Behavior in Elastomer Test

For a periodic material, effective material properties can be evaluated using a unit cell as illustrated in Figure 3.9. Homogenization methods can be regarded as an effective method to calculate material properties for small deformation problems. For finite deformation problem, the

effective material properties strongly depend on each deformation state and accurately predict material nonlinear behavior is still a challenging problem. Applying standard elastomer testing method is one feasible way to simplify the problem. Three major strain states including uniaxial tension, equal biaxial tension, and simple shear are applied in this chapter to evaluate effective material properties, and designs under three different strain states are presented to exhibit high stretchability and stiffness.

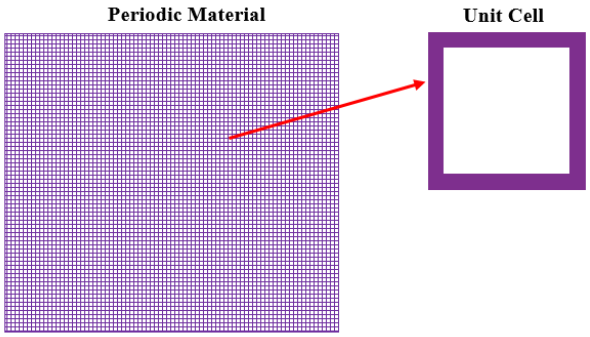

Figure 3.9 Schematic illustration of a unit cell and periodic materials

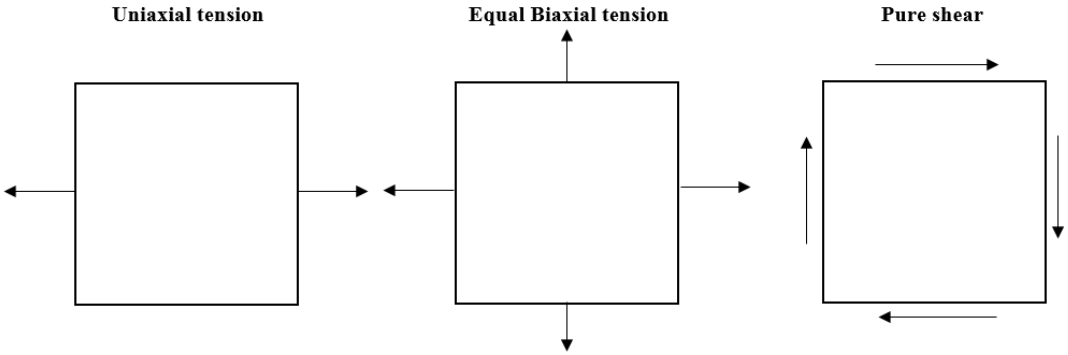

Figure 3.10 Three major strain states

In the elastomer tests, the material behavior can be characterized using the unit cell under MPCs boundary conditions. For uniaxial tension test, materials are uniformly stretched along longitudinally as shown in Figure 3.10. In such a situation, each node on the left and right

boundaries need to satisfy the displacement boundary condition, which means that a constant displacement difference u_c is assumed such that $u_r - u_l = u_c$. Note that u_r and u_l represent displacement on right and left boundary, respectively. It is important to mention that the transverse displacement for upper and lower boundary should also satisfy displacement boundary conditions.

For finite element analysis, multi-point constraints (MPCs) is an effective way to impose displacement difference boundary conditions [98]. MPCs enforce relations among the degrees of freedoms at two or more distinct nodes in a FE model. For multi-point constraints, a set of linear equations that couple the DOFs by the constraints, are called "constraint equations". In such a situation, the constraint equations can be written as,

$$\mathbf{Au=Q} \tag{3.13}$$

where A is a constant matrix and Q is a constant vector. u is global displacement vector. The schematic illustration of MPCs boundary conditions is demonstrated in Figure 3.11.

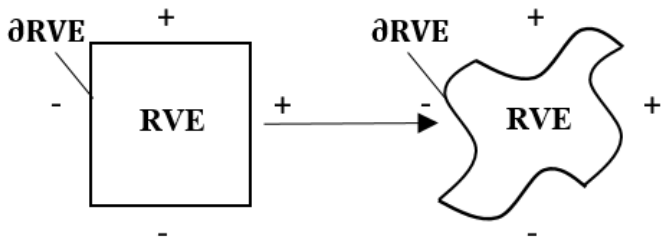

Figure 3.11 Schematic illustration of MPCs boundary conditions

To implement the above equations in nonlinear finite element analysis. Three different methods are available to impose above constraint equations, namely: (1) Transformation equation method, (2) Lagrange multiplier method, and (3) penalty function method. In this chapter, the penalty function method is applied to impose displacement difference conditions in FEM analysis.

For nonlinear finite element with constraint equations, the following equilibrium equation is constructed:

$$\boldsymbol{R(u)} + (\boldsymbol{A^T \alpha A})\boldsymbol{u} - \boldsymbol{F} - \boldsymbol{A^T \alpha Q} = \boldsymbol{0} \tag{3.14}$$

where $\boldsymbol{R(u)}$ is internal force and $\boldsymbol{F}$ is external force. $\boldsymbol{\alpha}$ is diagonal matrix of penalty weights, with $\boldsymbol{\alpha_{ii}} > 0$ and $\boldsymbol{\alpha_{ij}} = \boldsymbol{0}$ $(\boldsymbol{i \neq j})$**.** It is worth to mention that penalty term in above equations can be physically interpreted as additional forces to enforce the constraint approximately. Note that $\boldsymbol{A^T \alpha A}$ is referred to as penalty matrix, and the constraints can be satisfied exactly if the penalty weight $\boldsymbol{\alpha_{ii}}$ tends to infinity**.** Actually, choosing a right penalty need to balance the trade-off between reducing the constraint violation and limiting the solution error due to ill-conditioning system. In this chapter, the value of penalty weight is chosen as $\alpha_{ii} = 10^8$.

3.6 Generalized Energy Failure Criterion for Hyperelastic Materials

When designing stretchable metamaterial, the critical problem is that how to guarantee material reversible capacity under large deformation without plastic deformation or fracture. For regular 3D printing materials, the elastic regime of these materials is usually limited to 10% or less, such as ABS (Acrylonitrile butadiene styrene). For inorganic electronic materials such as silicon, small strains (around 1%) can lead to rupture. Therefore, the primary goal of designing stretchable metamaterial is resisting irreversible deformation. For metallic materials, von Mises stress or strain can work as a criterion to measure material failure behavior, while the failure mechanism is more sophisticated for soft materials. For centuries, scientists have made great efforts to develop theories for predicting mechanical failure of materials, and eventually the "generalized energy criterion" is proposed to be one universal law for various different kinds of

materials. Based on continuum thermodynamics, material failure in solid material is triggered by internal interactions between material particles, which is represented macroscopically by a specified elastic strain energy density. Energy-based failure criterion is regarded as a universal criterion for different types of materials. The failure of materials usually originates from a specific plane, and basic failure mechanisms contain two physical conditions: Shearing failure driven by shear stress and cleavage driven by the normal stress as presented in Figure 3.12. Fracture of material needs energy to break the atomic bonding to form the crack, and the energy density associated with the failure is defined presented in Figure 3.12

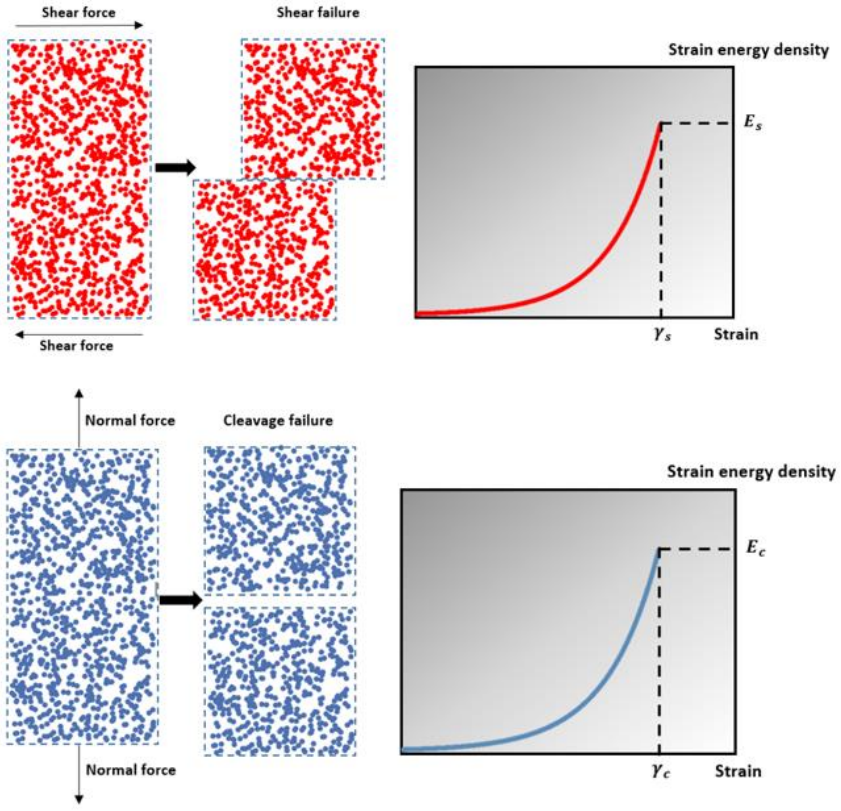

Figure 3.12 Illustrations on the two basic failure mechanisms of Hyperelastic materials

When designing soft materials, material models such as the Mooney-Rivlin model cannot model the softening of the material at large strains since the model assumes that the strain energy of the model materials can increase without bound. However, it is clear that no real material can store unlimited amount of energy without failure under finite deformation. As described in Ref. [99], real hyperelastic materials may experience softening when material strain is large enough. Volokh [100-104] further developed this theory and proposed the softening hyperelasticity approach, which describes strain softening by introducing the energy limiter. Meanwhile, Rittel et al [105] have observed the existence of material energy limiter in experiments. Traditional continuum-based hyperelastic models do not include energy limiter which leads to unbounded energy accumulation. Evidently, this is unphysical and may result in unreasonable engineering design when using traditional hyperelastic materials. To design stretchable metamaterial, the energy of real hyperelastic material needs to be limited the design load and may be defined as material failure energy. Such a limiter is a direct criterion to measure recoverability of material. In fact, different failure criteria have been utilized to describe failure of hyperelastic materials, which include the (1) maximum principal stress, (2) maximum principal stretch, (3) maximum shear stress, (4) von Mises stress, and (5) strain energy. Based on the experiment conducted by Volokh [92], the results show that strain energy is almost constant for the failure states induced by various loading modes ranging from uniaxial to equal biaxial tension. The von Mises stress exhibits a wider range of scattering as compared to strain energy. The maximum stresses and stretches vary significantly with the variation of loads from uniaxial to equal biaxial tension. Thus, using strain energy as failure criterion is more accurate and reasonable for measuring failure of soft material and hence will be utilized also in the optimization algorithm development.

3.7 Optimization Method

This study focuses on designing materials to present better stretchability and stiffness under finite deformation. The optimization formulation is described in detail in this section.

3.7.1 Design parameterizations

For structures experiencing large strains, excessive mesh distortion in low-density region often occurs, which always leads to divergence of nonlinear finite element analysis. Remeshing can alleviate this issue but is a cumbersome and computationally expensive process. To make optimization robust, an energy interpolation form proposed by Wang et al [58] is adopted here to relieve excessively distorted mesh in low-density area:

$$\Phi_e(\boldsymbol{u}_e) = [\Phi(\gamma_e \boldsymbol{u}_e) - \Phi_L(\gamma_e \boldsymbol{u}_e) + \Phi_L(\boldsymbol{u}_e)]E_e \tag{3.15}$$

where $\Phi()$ is the stored elastic energy density for base material and $\Phi_L()$ is the stored elastic energy density under small deformation. E_e is a scaling parameter (i.e. $E_e = 1$ for solid material and $E_e = \varepsilon$ (ε is a very small value) for void region). Linear element is chosen to describe material deformation behavior for low-density elements, which is insensitive to large deformation. In contrast, high-density elements need to be analyzed by non-linear analysis. In the equation above, the interpolation factor γ_e equals to unity for solid elements, while $\gamma_e = 0$ corresponds to void element. The interpolation factor should satisfy that the stored energy corresponds to linear energy when $\gamma_e = 0$, while the elastic energy is simply depicted by the nonlinear energy term if $\gamma_e = 1$. A continuous and smooth method based on the Heaviside projection function is applied to ensure a smooth and differentiable transition between these two regions, which is successfully tested by

the fictitious domain approach [58]. Therefore, the threshold parameter γ_e can be modeled as follows:

$$\gamma_e = \frac{\tanh(\beta_1 x_t)+\tanh\left(\beta_1(\bar{x}_e{}^{pl}-x_t)\right)}{\tanh(\beta_1 x_t)+\tanh(\beta_1(1-x_t))} \tag{3.16}$$

where x_t is a threshold used to determine the element behavior, and $\bar{x}_e$ is the element density. In most cases, $x_t = 0.01$ and $\beta_1 = 500$ are reasonable values to separate these two distinct regions in the optimization progress. The scaled parameter E_e for each element can be interpolated as:

$$E_e = \bar{x}_e(\boldsymbol{X})^{pl}(1-\varepsilon)+\varepsilon \tag{3.17}$$

where ε is a very small value (i.e. $\varepsilon = 10^{-5}$). pl is penalization parameter and is set to a value of 3 in this work unless otherwise stated. Note that $\boldsymbol{X}$ is the design variable.

3.7.2 Optimization Formulations

The optimization problem for designing stretchable and stiff metamaterial can be formulated to maximize material stiffness with local failure constraint for a given finite strain:

$$\max \boldsymbol{f} = \boldsymbol{l}^{\boldsymbol{T}}\boldsymbol{f}^{\boldsymbol{int}}(\boldsymbol{u}) \quad subject\ to \begin{cases} \frac{V(\boldsymbol{X})}{|\Omega|} - v_f^* \le 0 \\ c\left[\frac{1}{N}\sum_{i=1}^{N}\left(\frac{E_i(\boldsymbol{X})}{\bar{E}}\right)^p\right]^{\frac{1}{p}} < 1 \end{cases} \tag{3.18}$$

where $\boldsymbol{l}$ is a zero vector with unit entries at the degrees of freedom on the boundary, and $\boldsymbol{l}^{\boldsymbol{T}}\boldsymbol{f}^{\boldsymbol{int}}(\boldsymbol{u})$ represents reaction force on the boundary due to prescribed displacement. $E_i(\boldsymbol{X})$ is strain energy for every element and $\bar{E}$ is prescribed energy limiter for material failure. Note that the p-norm formulation is applied to measure local maximum element strain energy and c is an adaptive parameter. N denotes element number, and p-norm parameter is chosen as $p = 10$. $V(\boldsymbol{X})$ is the

volume of the design, $|\Omega|$ is the total volume of the initial fixed design domain, and v_f^* is the prescribed volume constraint.

3.7.3 General Sensitivity Derivation based on Adjoint Method

Gradient-based optimization method is employed here to solve the optimization problem above efficiently by deriving accurate sensitivities of the objective function and constraints. In the current study, gradients can be evaluated analytically using the adjoint method. For adjoint method, a general formulation corresponding to the nonlinear model is described in this section. The governing equilibrium equation in residual form can be written as follows:

$$\boldsymbol{\Psi} = \boldsymbol{R} - \boldsymbol{F} = \mathbf{0} \tag{3.19}$$

Any other constraint equations for the physical problem are expressed as follows:

$$\boldsymbol{\mathcal{H}} = \mathbf{0} \tag{3.20}$$

For a given function $\mathcal{F}$, which can work as objective or constraint, an augmented Lagrangian function G is formulated based on the adjoint method:

$$\boldsymbol{G} = \boldsymbol{\mathcal{F}} + \boldsymbol{\psi}^{\boldsymbol{T}}\boldsymbol{\Psi} + \boldsymbol{\kappa}^{\boldsymbol{T}} \cdot \boldsymbol{\mathcal{H}} \tag{3.21}$$

where $\boldsymbol{\psi}$ and $\boldsymbol{\kappa}$ are Lagrange multiplier. For arbitrary vectors $\boldsymbol{\psi}$ and $\boldsymbol{\mathcal{H}}$, the equation $G = \mathcal{F}$ can be established. Thus, achieving the derivative $\frac{\partial G}{\partial \boldsymbol{\rho}}$ is equivalent to obtaining the sensitivities of the augmented Lagrangian function G with respect to material density ρ. A general procedure to obtain the derivative of G using the chain rule can be expressed as:

$$\frac{\partial \boldsymbol{G}}{\partial \boldsymbol{\rho}} = \frac{\partial \boldsymbol{\mathcal{F}}}{\partial \boldsymbol{\rho}} + \frac{\partial \boldsymbol{\mathcal{F}}}{\partial \boldsymbol{U}}\frac{\partial \boldsymbol{U}}{\partial \boldsymbol{\rho}} + \boldsymbol{\psi}^{\boldsymbol{T}}\left(\frac{\partial \boldsymbol{\Psi}}{\partial \boldsymbol{\rho}} + \frac{\partial \boldsymbol{\Psi}}{\partial \boldsymbol{U}}\frac{\partial \boldsymbol{U}}{\partial \boldsymbol{\rho}}\right) + \boldsymbol{\kappa}^{\boldsymbol{T}} \cdot \left(\frac{\partial \boldsymbol{\mathcal{H}}}{\partial \boldsymbol{\rho}} + \frac{\partial \boldsymbol{\mathcal{H}}}{\partial \boldsymbol{U}}\frac{\partial \boldsymbol{U}}{\partial \boldsymbol{\rho}}\right) \tag{3.22}$$

where $\boldsymbol{U}$ is the global displacement vector and operator $\frac{\partial}{\partial \rho}$ represents a derivative with respect to ρ . Re-arranging above Equation as follows:

$$\frac{\partial G}{\partial \rho} = \left(\boldsymbol{\psi}^{\boldsymbol{T}} \frac{\partial \boldsymbol{\Psi}}{\partial \boldsymbol{U}} + \boldsymbol{\kappa}^{\boldsymbol{T}} \frac{\partial \boldsymbol{\mathcal{H}}}{\partial \boldsymbol{U}} + \frac{\partial \mathcal{F}}{\partial \boldsymbol{U}}\right) \frac{\partial \boldsymbol{U}}{\partial \rho} + \frac{\partial \mathcal{F}}{\partial \rho} + \boldsymbol{\psi}^{\boldsymbol{T}} \frac{\partial \boldsymbol{\Psi}}{\partial \rho} + \boldsymbol{\kappa}^{\boldsymbol{T}} \frac{\partial \boldsymbol{\mathcal{H}}}{\partial \rho} \tag{3.23}$$

Choosing $\boldsymbol{\psi}$ and $\boldsymbol{\kappa}$ such that

$$\boldsymbol{\psi}^{\boldsymbol{T}} \frac{\partial \boldsymbol{R}}{\partial \boldsymbol{U}} + \boldsymbol{\kappa}^{\boldsymbol{T}} \frac{\partial \boldsymbol{\mathcal{H}}}{\partial \boldsymbol{U}} + \frac{\partial \mathcal{F}}{\partial \boldsymbol{U}} = \boldsymbol{0} \tag{3.24}$$

The parameter ψ and κ are known as adjoint vector. Thus,

$$\frac{\partial G}{\partial \rho} = \frac{\partial \mathcal{F}}{\partial \rho} + \boldsymbol{\psi}^{\boldsymbol{T}} \frac{\partial \boldsymbol{\Psi}}{\partial \rho} + \boldsymbol{\kappa}^{\boldsymbol{T}} \frac{\partial \boldsymbol{\mathcal{H}}}{\partial \rho} \tag{3.25}$$

The above derivation is usually referred to as the discrete adjoint method.

3.7.4 Sensitivity of Objective and Constraints

Note that element density ρ is chosen as design variable in this section, and sensitivity with respect to Bézier-based representation parameters **X** can be obtained by the chain rule. For MPCs boundary conditions, the equilibrium equations can be written as:

$$\boldsymbol{r} = \boldsymbol{R}(\boldsymbol{u}) + (\boldsymbol{A}^{\boldsymbol{T}} \boldsymbol{\alpha} \boldsymbol{A})\boldsymbol{u} - \boldsymbol{F} - \boldsymbol{A}^{\boldsymbol{T}} \boldsymbol{\alpha} \boldsymbol{Q} = \boldsymbol{0} \tag{3.26}$$

Based on design parametrization, the adjoint method described in above section is employed to obtain the sensitivities of the objective and constraint functions θ, with respect to density ρ, given as:

$$\frac{\boldsymbol{\partial \theta}}{\boldsymbol{\partial \rho}} = \frac{\boldsymbol{\partial \theta(u)}}{\boldsymbol{\partial \rho}} + \boldsymbol{\lambda}^{\boldsymbol{T}} \frac{\boldsymbol{\partial r}}{\boldsymbol{\partial \rho}} \tag{3.27}$$

The adjoint variable vector λ is obtained by solving the following equation:

$$(\boldsymbol{K}^{*})^{\boldsymbol{T}} \boldsymbol{\lambda} = -\left(\frac{\boldsymbol{\partial \theta(u)}}{\boldsymbol{\partial \rho}}\right)^{\boldsymbol{T}} \tag{3.28}$$

where

$$\boldsymbol{K}^{*} = \left(\boldsymbol{K_t} + (\boldsymbol{A^T \alpha A})\right) \tag{3.29}$$

Note that $\boldsymbol{K_t}$ is the tangent stiffness matrix at the equilibrium state, and superscript $\boldsymbol{T}$ denotes the transpose of the matrix.

3.8 Initial Guess of Geometric Component Distribution

As in previous works [15], random initial guess of geometry component is chosen to initiate optimization. It is feasible to use random initial distribution for linear problem. One weakness of random initialization is that the ends of one geometry component do not always connect with other components. Thus, this non-connectivity issue is undesirable for solving geometry nonlinear problem in that excessive mesh distortion may happen in the gap region during FEM analysis. Hence it is essential to find an initial layout which should be a connected path of geometry components between loads and the boundary conditions. As described by Ref. [19], the value of failure constraint is highly sensitive to a small change of geometric component design variables, and hence some perturbed initial values could lead to unreasonable optimal design. Thus, a reasonable initial value of design variables is of great significance for convergence of optimization progress. However, how to construct an initial connected design is still a tricky problem, especially for nonlinear optimization problem. From our numerical experiments, a density based optimal design can work as a guidance for geometric component initialization. Inspired by this experience, an identification process is proposed in this chapter to construct a reasonable initial values of design variables. This identification progress can be divided into two parts. This first part is topology optimization using density-based methods to obtain a coarse layout, which can be used as a design guidance for optimization with geometric component. It is worth to mention that there

is no need to reach an ideal 0-1 solution for density based optimization. A coarse layout with a large amount of intermediate densities during optimization progress (i.e. iteration=10) is enough to yield an initial layout. The second part is an identification progress, which can be regarded as an auxiliary optimization problem. The auxiliary optimization problem is formulated as follows:

$$minimize \ \ \sum(\bar{\bar{X}}_G(\boldsymbol{\chi_i}, \bar{\bar{\rho}}, w) - X_I)^2 \tag{3.30}$$

where parameters $\boldsymbol{\chi_i}, \bar{\bar{\rho}}, w$ are the design variables of geometric components. $\bar{\bar{X}}_G$ denotes density projection from geometric components. X_I represents objective density from density-based optimization results. Hence, this optimization problem aims to find an optimal initial layout of geometric component by minimizing the difference between geometry projection with desired density distribution from density-based optimal results. Due to the limited parameters needed to be identified, sequential quadratic programming (SQP) method [88] is implemented here to find a local minimum of the cost function. Detailed description of the identification progress will be demonstrated in numerical examples. It is worth to mention that the material layouts do not have distinct difference under three different loading conditions after the few initial optimization iterations (i.e. 10). For simplicity, we apply the density-based optimized material layout under uniaxial tension as initial configuration to the proposed optimization method for all numerical examples.

3.9 2D Optimized Results under Uniaxial Tension

For material design under uniaxial tension, we design materials with symmetry along both axial directions. To characterize material behavior using the unit cell as presented in Figure 3.13, MPCs boundary conditions are applied along four sides of the design domain. $\bar{\boldsymbol{u}}$ is a constant

displacement difference between right and left edges. The strain energy limit for base material is set to 1.1, which corresponds to 10% strain under uniaxial tension. The goal is to maximize the material stiffness under 30% strain along the horizontal direction without local material failure. The design domain is discretized with 100×100 quadrilateral elements with element size equals to 1. The loading and boundary conditions together with the design domain are plotted in Figure 3.13. The constant displacement difference is set to $\bar{\boldsymbol{u}} = 30$. The width of the Bézier skeleton is set to be $2 < w < 3$, and volume fraction constraint is chosen as 0.3. Note that the value of p-norm for strain energy aggregation is chosen as $p = 10$. In fact, increasing the value of p is better to improve the approximation of the maximum, while a value of p that is too high will result in convergence difficulty during optimization. Due to the highly nonlinear nature, the move limit for MMA algorithm need to be small enough to ensure that no gap exists during optimization progress, which will lead to excessive mesh distortion in finite element analysis. The move limit is chosen as 0.01 after several numerical tests. The optimized material layout is shown in Figure 3.14 (a). For comparison, the optimized density results without failure constraint is plotted in Figure 3.14 (b). Based on optimization results considering failure constraint, only four effective Bézier-based components remain after optimization has been completed, which demonstrates that the optimizer is able to remove redundant geometric components from the initial design. We would like to mention that there is no need to employ higher order Bézier curves, because 15 initial components have enough degrees of freedom to explore the design domain. The 5×5 lattice structures obtained based on the optimized design are shown in Figure 3.16. It is interesting to find that the optimized metamaterial considering failure constraint shares high similarity to the so-called "horseshoe" serpentine design, which is widely used in stretchable electronics. Besides stretchable electronics, these serpentine-shaped structures can be found in many expandable systems made by

stiff materials such as cardiovascular stents. The “horseshoe” serpentine structure is presented in Figure 3.17. In fact, “horseshoe” microstructures can rotate to accommodate the applied displacement, leaving much smaller intrinsic strain in the base materials compared with the applied strain. The contours of strain energy distribution with a thousand lines are presented in Figure 3.18. The maximum local strain energy of optimized results without failure constraint almost reaches 20, while the material stiffness is around 4 times compared to the optimized design considering failure constraint. The optimized compliance of unit cell based on BSED is 17.4. To make a comparison, an optimized result with standard density-based method is presented in Figure 3.19. For the standard density-based method, where each element works as a design variable, the staggered boundary can be found in the optimized result as shown in Figure 3.19. Some post-processing techniques are needed to generate smooth material layouts. Small holes are also found in the optimized results, which is not preferred for additive manufacturing [106] due to precision limitation. For the design generated with BSED method, the designs are described by Bézier curve with certain thickness, the boundary can be smooth enough due to explicit geometric description without any limitation of FEM mesh resolution. The other merit of BSED is that it is easier to generate standard CAD model and edited in general CAD software [107], because the optimal design is described by parametric space, which is ready to directly define geometry in software using feature-based modeling [108], instead of converting the STL (stereolithography) file to ISO standard exchange format (i.e. STEP file [109]). Meanwhile, the number of design variables is reduced significantly compared to standard density-based method. The optimized compliance of unit cell with standard density-based method is 15.8, which is slightly lower than optimized result generated by BSED method. This is reasonable due to more freedom in the design space.

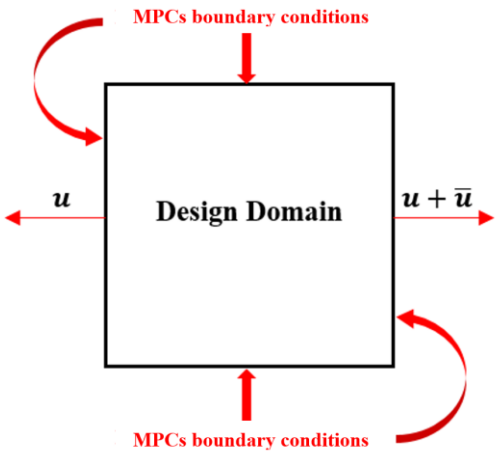

Figure 3.13 Design domain of a unit cell in uniaxial tension

(a) with failure constraint (b) without failure constraint

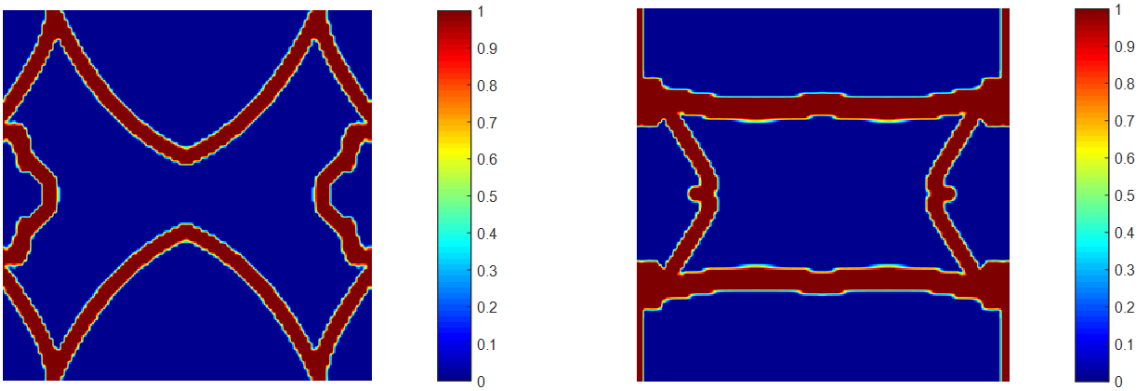

Figure 3.14 Optimized density results in uniaxial tension (a) with failure constraint and (b) without failure constraint

(a) with failure constraint (b) without failure constraint

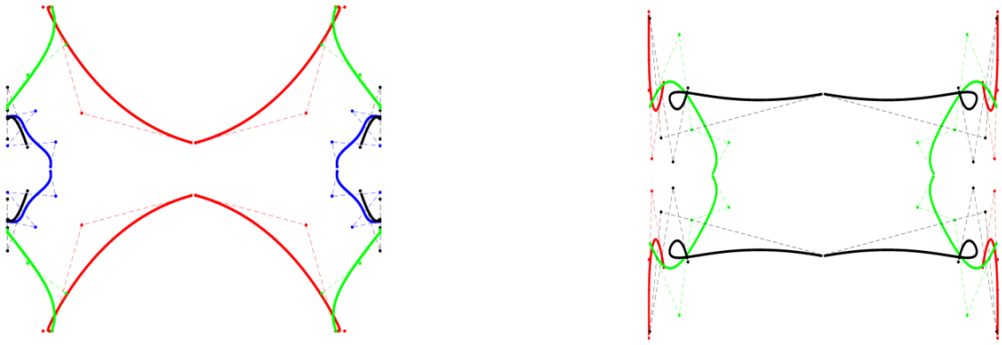

Figure 3.15 Optimized Bézier skeleton (a) with failure constraint and (b) without failure constraint

(a) with failure constraint (b) without failure constraint

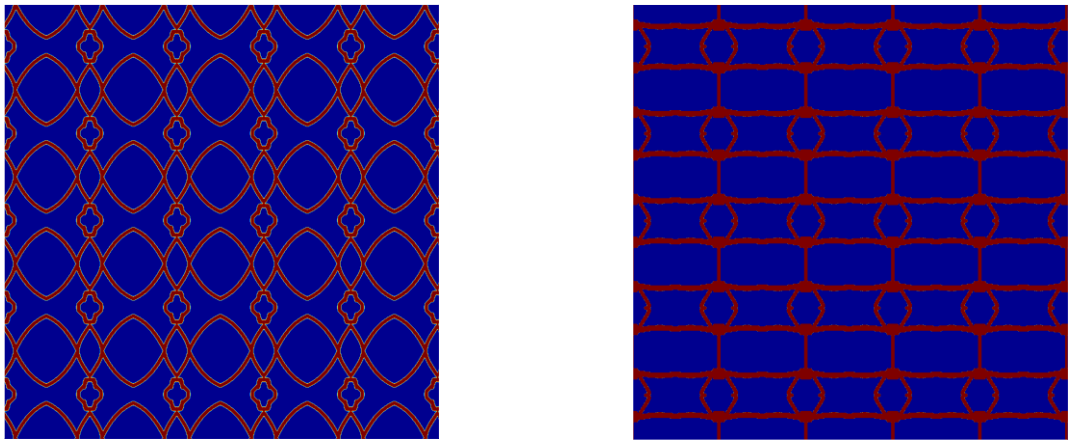

Figure 3.16 5 by 5 lattice structures consisted of the optimized unit cell design (a) with failure constraint and (b) without failure constraint

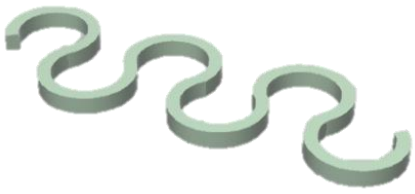

Figure 3.17 The "horseshoe" serpentine shape structure

(b) with failure constraint

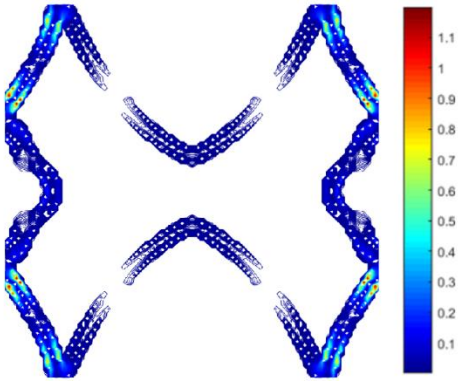

(b) without failure constraint

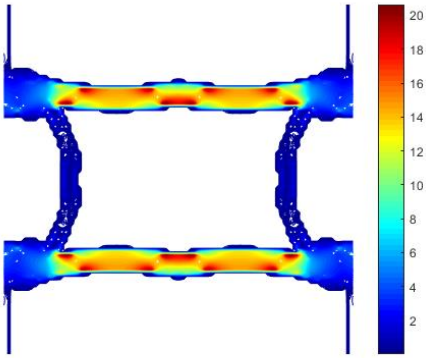

Figure 3.18 Strain energy distribution for the undeformed configuration (a) with failure constraint (b) without failure constraint

(a) Undeformed configuration

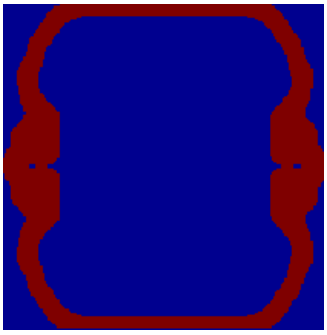

(b) Deformed configuration

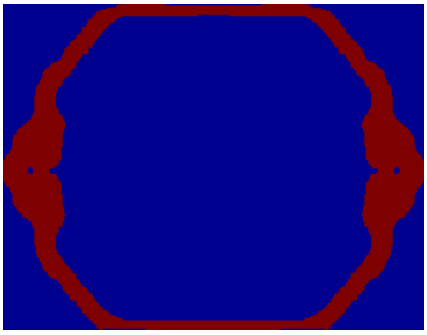

Figure 3.19 Optimized result with standard density-based method (a) Undeformed configuration (b) Deformed configuration

3.10 2D Optimized Results under Equal Biaxial Tension

In this subsection, we apply the proposed optimization formulation to design materials under equal biaxial tension, see Figure 3.20. We aim at designing high stiffness materials subjected to 30% strain along both longitudinal and transverse directions without local failure. The

dimension and material properties are the same as previous numerical example, where 100×100 quadrilateral elements with element size equals to 1 are used to discretize the design domain. The same optimization parameters are applied in this numerical example. The maximum allowed volume is 30% of the design domain volume. The optimized microstructure considering failure constraint is presented in Figure 3.21(a), while the result without constraint is shown in Figure 3.21(b). Figure 3.22 show the optimized Bézier skeletons. The optimized result show "horseshoe" structures along both directions. Note that only the geometric components with $\bar{\rho} > 0.1$ are displayed. For design without failure constraint, the optimized microstructure shares much similarity with the honeycomb structure, see Figure 3.23(b). The perspective of the full periodic microstructure is demonstrated in Figure 3.23. The strain energy contours are found in Figure 3.24, where deformation at 30% strain along both directions is plotted in Figure 3.25.

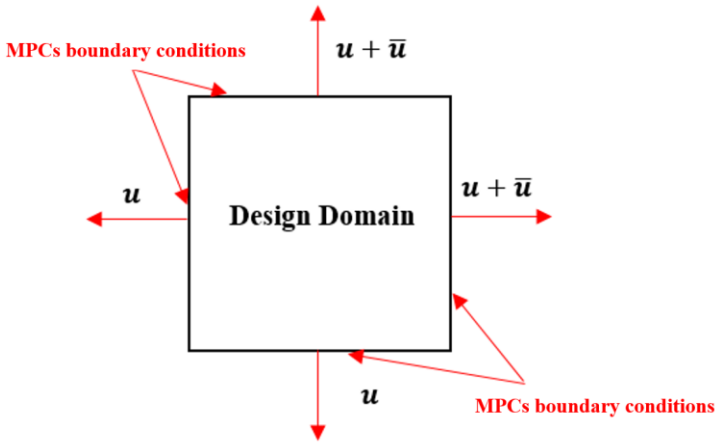

Figure 3.20 Design domain of a unit cell in equal biaxial tension

(a) with failure constraint (b) without failure constraint

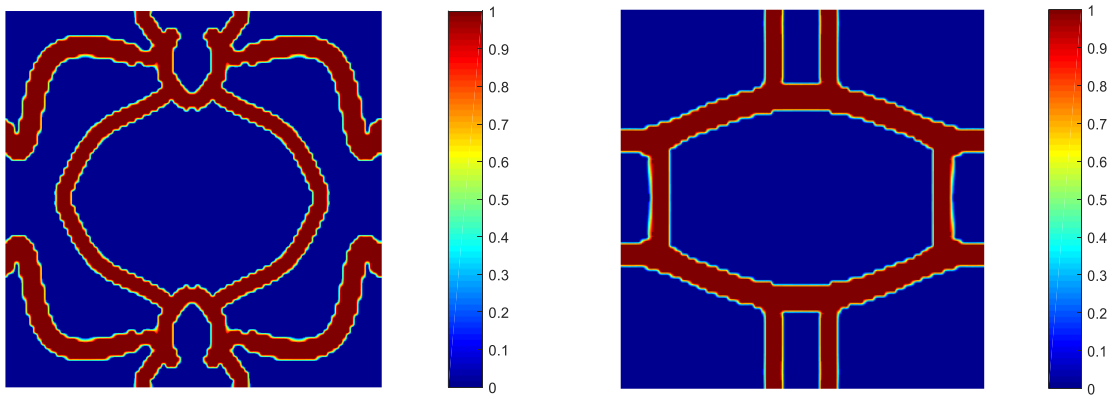

Figure 3.21 Optimized density results in equal biaxial tension (a) with failure constraint and (b) without failure constraint

(a) with failure constraint (b) without failure constraint

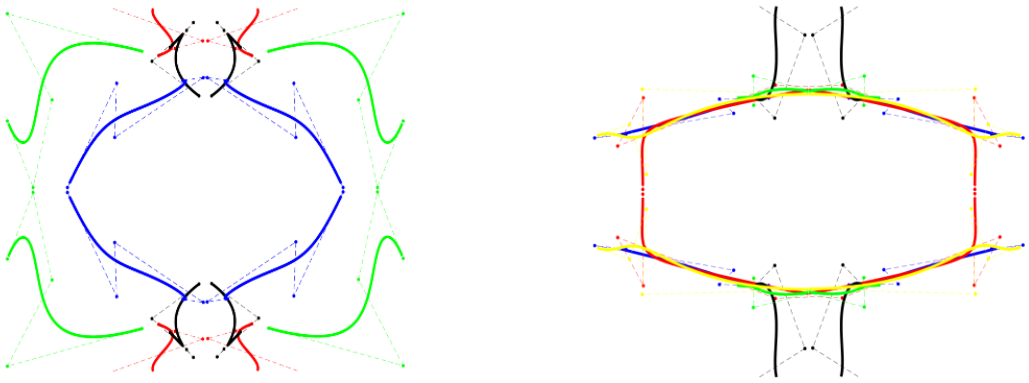

Figure 3.22 Optimized Bézier skeleton (a) with failure constraint and (b) without failure constraint

(a) with failure constraint (b) without failure constraint

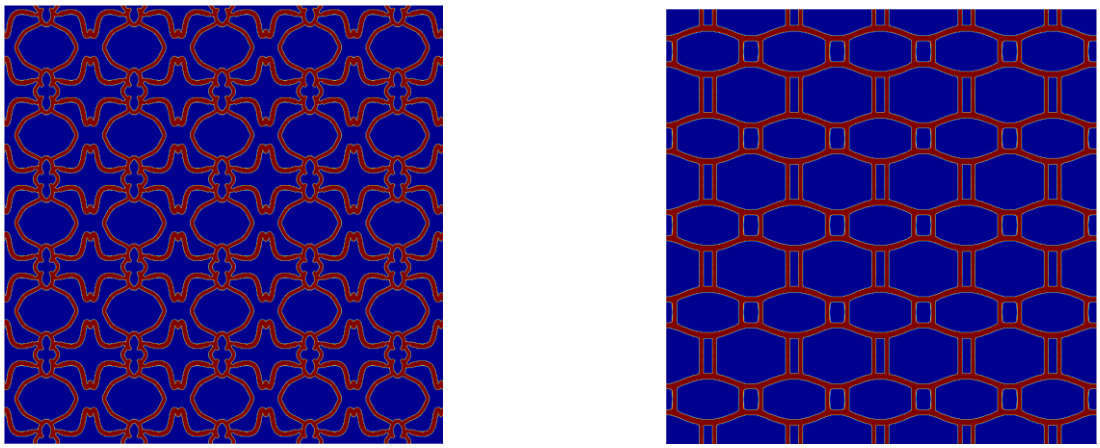

Figure 3.23 A 5 by 5 lattice structure consisted of the optimized unit cell (a) with failure constraint and (b) without failure constraint

(a) with failure constraint (b) without failure constraint

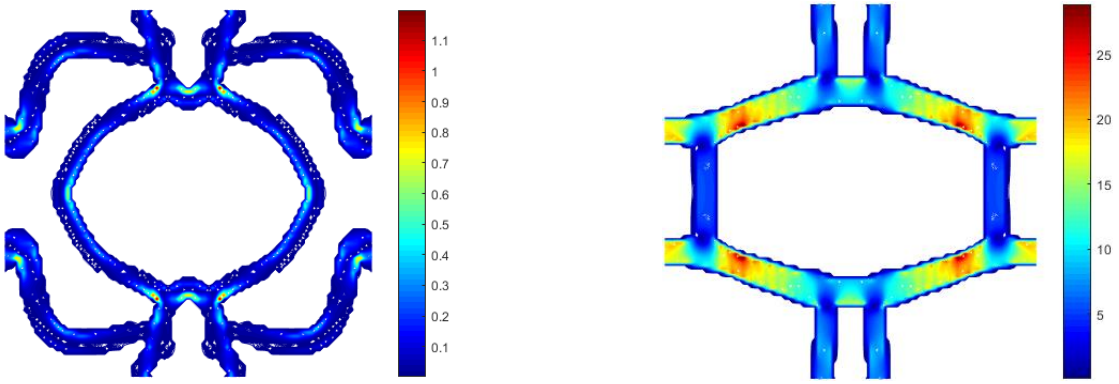

Figure 3.24 Strain energy distribution on undeformed configuration (a) with failure constraint and (b) without failure constraint

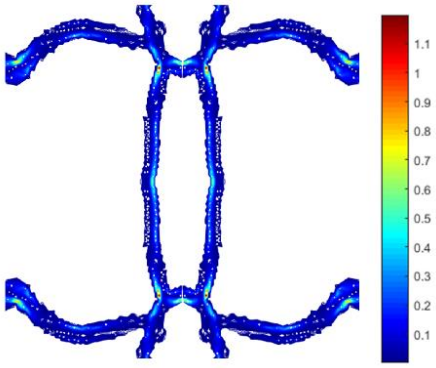

Figure 3.25 Strain energy distribution contours on deformed configuration

3.11 Conclusions and Discussions

In this chapter, a Bézier skeleton explicit density (BSED) representation algorithm is proposed for the topology optimization of stretchable metamaterial. Material failure is measured by strain energy and p-norm formulation are utilized. A Heaviside function is applied to create a mapping from geometry skeleton to mesh grids, where the skeleton is described by the Bézier curves. This density representation method successfully inherits the main advantages of density-based topology optimization. Sensitivities of the objectives and constraints with respect to control parameters can be readily derived by using the chain rule. Standard nonlinear programming algorithms are applied in this algorithm. The initial configuration for the proposed method is obtained by performing optimization using standard density-based method on coarse mesh for a few iterations, which would lead to a well-connected layout. From the numerical examples, redundant geometry members can be removed, and the thickness of skeleton can be easily controlled by parameters of Heaviside function. Due to the powerful curve fitting ability, using Bézier curve to represent density field can explore design space effectively compared to bar-like

structures, and generate manufacturing friendly structures without any intricate small features in optimal design. Furthermore, this density representation method is mesh independent and the design variables are reduced significantly so that the optimization problem can be solved efficiently using regular optimization algorithm. From the numerical results, the optimized material layout shares high similarity to the “horseshoe” structures, which are widely found in soft electronics design. Therefore, the method proposed in this chapter shows great potential and opens the door for designing manufacturable microstructures to achieve extreme stretchable materials that can be utilized for applications such as stretchable electronics and soft robotics.

4.0 Projection-based Method for Flexible Functionally Graded Lattice Design

4.1 Current Progress of Optimization for Lattice Structure Design

Cellular materials or lattice structures have been utilized in numerous applications and are common in nature, such as bone, wood, sponge, etc. Recently, these porous materials are designed to achieve multi-functional material for weight reduction, energy absorption or heat transfer [110, 111]. Lattice structures made by metal are widely applied to product design in the field of orthopedic regenerative medicine [112]. These include, for example, design of bone scaffolds and implants to replicate the biomechanical properties of host bones. Porous metallic structure is an ideal candidate for repairing or replacing damaged bone because of its tunable mechanical properties. More importantly, porous metals can be designed to be open-celled to promote in-growth of bone tissue, which accelerates the osseointegration process. Conventional processes are difficult or impossible to fabricate porous media due to intricate internal architecture. Recent advancement in additive manufacturing (AM) enables fabrication of lattice structures which has significantly increased the demands for implants with customized mechanical performance [112]. In fact, open-celled lattice structures are preferred for additive manufacturing for many reasons including [113]: a) inherent porosity can minimize residual stress to reducing printed part distortion, b) reduce support materials due to self-supporting unit cells, and c) no enclosed voids so that the powder can be easily removed. Several approaches are proposed in recent years to generate lattice structures, such as generic ground truss structure approaches etc. [113, 114]. Triply periodic minimum surfaces (TPMS) is becoming a promising microstructure for designing scaffolds due to its extraordinary mechanical performance. TPMS is composed of three-

dimensional continuous smooth surfaces, for which the average curvatures at each surface point is zero. These structures are called biomimetic structures, which is widely found in biological systems in nature, such as butterfly wings. Due to its geometric properties, these structures have the advantages of lightweight, high strength, and high specific surface area. Another merit of TPMS is that these structures can be defined using implicit equations. Besides, TPMS has already been proven to be a versatile source for biomorphic scaffold designs, and provided a viable and stable environment to replace damaged bones because of the smooth bending properties and optimized fluid permeability [115]. In this chapter, we focus on the design of functionally graded lattice structure with TPMS unit cell due to its extraordinary mechanical properties.

Topology optimization (TO) for designing functionally graded lattice is a hot topic in recent years. Several efficient topology optimization methods have been proposed based on homogenization theory by assuming that the two scales are separated [116-123], and some algorithms were developed based on reduced order modeling technique [124-126]. In recent years, some new hierarchical lattice structure design methods have been proposed as well. Xia [127] reviews recent advances in designing multiscale structural modeling and design of nonlinear structures. Yvonnet et al [128] proposed a topology optimization method for lattice structures in the case of non-separated scales, where a non-local numerical homogenization method is implemented. Recent advances in scale-related periodic design, the prefect connectivity between different optimized unit cell is guaranteed [118, 120, 129-133].

The conventional computer-aided design (CAD) technique creates geometric objects using surfaces, which is an ideal solution for visualization and conventional subtractive manufacturing process, such as computer numerical control (CNC) cutting machine tools. However, this surface-based shape representation method is not an ideal for designs for additive manufacturing (AM).

The AM technology builds an object in a layer-by-layer way, which can be applied to print extremely complex designs such as porous scaffolds or lattice structures. In general, geometric model for AM can be implemented using voxels, tetrahedra, parametric solids, or implicit field function [134] defined in three-dimensional space. However, using voxel points or a set of tetrahedra can be expensive in terms of storage space. Moreover, representation with voxels or tetrahedra provide only an approximation of the real object. For parametric representation, it is extremely tedious and difficult to design lattice structures using constructive solid geometry (CSG) [135]. Compared to the above methods, a ready-to-print geometric object is to describe a geometry as a 3D function $F(x, y, z)$, which directly informs the AM machine to determine whether the point $\boldsymbol{P}(x, y, z)$ should be printed. Recent research has shown that geometry modeling using implicit functions are particularly suitable for modeling lattice and porous media. This AM-friendly modeling method has attracted great attention from academia and industry for AM design and has already been used to model any complex geometry in general. More importantly, this implicit field modeling method for AM has already been commercialized and achieve great success by a software company called nTopology, Inc. The main advantages of implicit modeling are as follows: i) An implicit geometry is directly defined in the physical space, which can directly provide precise information of objects to a 3D printer. ii) Implicit modeling is a lightweight geometric modeling technique without requirement of massive storage space. iii) Recent research has shown that implicit functions are particularly suitable for modeling microporous structures [134, 136]. Therefore, using implicit function to model porous media or lattice scaffold is a more advanced and feasible approach for future AM-oriented design.

4.2 Implicit Modeling for Functionally Graded Lattice

4.2.1 Generation of Functionally Graded Lattices based on Implicit Modeling

In general, lattice unit cells can be constructed using surface-based representation method. Using the TPMS as an example, the structure can be defined by an implicit function (i.e. $f(x, y, z) = t$), where t is the parameter that governs the offset from the level sets, and t can vary in design domain. There are several different types of TPMS as described in Ref. [113]. The four typical structures of TPMS [137] are shown in Figure 4.1. The TPMS can be utilized to create lattice structures with unique mechanical characteristics. Furthermore, the lattice structures generated by TPMS have a higher surface-to-volume ratio compared with traditional strut-based lattice structures [138]. The gyroid is one of the most popular TPMS with robust mechanical performance. In this chapter, we focus on the lattice design based on the gyroid minimum surface.

(a) G ('Gyroid') (b) P ('Schwarz P') (c) D ('Diamond') (d) N ('Neovius')

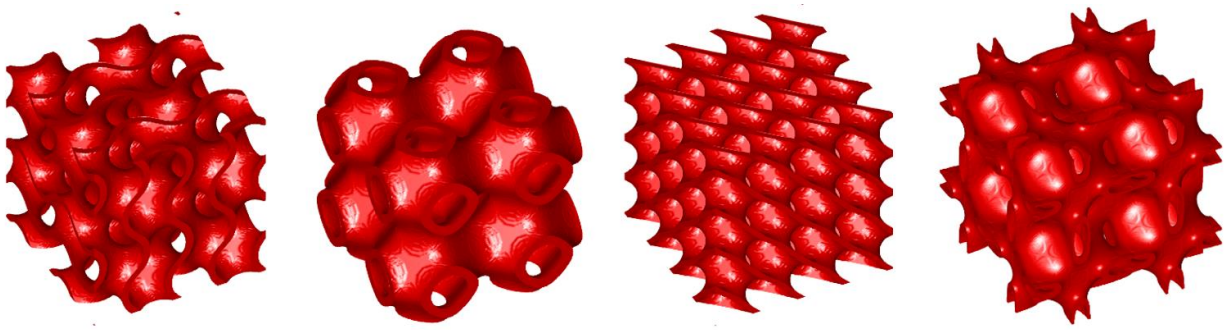

Figure 4.1 Triply periodic minimal surface (TPMS)

In general, explicit TPMS formulation can be constructed using inequality conditions expressed as follows [113]:

$$f(x, y, z)^2 \leq t \quad (t > 0) \tag{4.1}$$

The control equations for the gyroid surface is

$$f_G(x,y,z) = \sin(\lambda_x x)\cdot\cos(\lambda_y y) + \sin(\lambda_y y)\cdot\cos(\lambda_z z) + \sin(\lambda_z z)\cdot\cos(\lambda_x x) \quad (4.2)$$

where $\lambda_i (i = x, y, z)$ is the function periodicity, expressed as:

$$\lambda_i = \frac{2\pi}{L_i} \ (with\ i = x, y, z) \quad (4.3)$$

where L_i is the absolute dimension which defines the length of a unit cell. To design functionally graded lattice structures, the material grading in three-dimensional space can be realized by operating through 4D representation (x, y, z, t), where the t is an iso-value matrix in the (x, y, z) space. Therefore, a functionally graded lattice can be represented in an implicit way as follows:

$$f(x,y,z)^2 \leq t(x,y,z) \quad (4.4)$$

where the $t(x, y, z)$ controls the spatial variation of unit cell volume fraction in three-dimensional Cartesian space. Therefore, designing functionally graded (FG) TPMS lattice is equal to varying the variable $t(x, y, z)$ in the design domain. The design domain for $t(x, y, z)$ in Cartesian space can be discretized by voxels. The continuous function $t(x, y, z)$ in space can be reconstructed through field values at every voxel. In fact, the periodicity λ_i can be also varied in three-dimensional Cartesian space. However, the periodicity is fixed in the design domain for the present work.

For conventional density-based topology optimization, design domain is discretized by finite element (FE) mesh, where each element works as a design variable. To connect the implicit field with density-based method, a Heaviside function-based projection method is implemented here to map the implicit field to the background FE mesh, which enables topology optimization algorithm to be performed on a fixed grid. An approximate Heaviside function can be defined as

$$\mathrm{H}_{a,c}(x) = \frac{1}{1+e^{-a\cdot(x-c)}} \quad (4.5)$$

In the above equation, a and c are two parameters that could control the shape of Heaviside function. A projection from the parametric design space $t(x,y,z)$ to density field ρ can be expressed as:

$$\rho(x,y,z) = \mathrm{H}_{a_0,c_0}\big(t(x,y,z)\big) \cdot \mathrm{H}_{a_1,c_1}(t(x,y,z) - f(x,y,z)^2) \tag{4.6}$$

where H_{a_0,c_0} and $\mathrm{H}_{a_1,c_1}$are Heaviside function defined in Eq. (4.5) with different control parameters. Note that the $t(x,y,z)$ is closely related to the volume fraction of unit cell. Thus, the first term is used to control the volume fraction of gyroid lattice. If the volume fraction at point (x,y,z) is a small value, the first term will tend to zero so that the material at this point can be removed. The second term works as a projection to map the gyroid lattice to density field. Hence Eq. (4.6) is capable of mapping the design space $t(x,y,z)$ to density field $\rho(x,y,z)$. In practice, the design space $t(x,y,z)$ is a continuous differentiable function in design domain. To effective construct implicit field $t(x,y,z)$ in the entire design domain with a single globally continuous and differentiable function**,** the radial basis functions (RBFs) [139] is introduced here to model the implicit field $t(x,y,z)$. The RBFs are able to interpolate scattered data to generate smooth surface, and is an effective way to approximate complex function. Radial basis functions are radially symmetric functions centered at a specific point, called an RBF knot, which can be expressed as follows:

$$\varphi_i(\boldsymbol{x}) = \varphi(\|\boldsymbol{x} - \boldsymbol{x_i}\|) \tag{4.7}$$

where $\|\cdot\|$ denotes the Euclidean norm and $\boldsymbol{x_i}$ is the position of the knot. There are several possible radial basis functions, including thin-plate spline, Gaussians [140], etc. In this chapter, The Gaussian function is chosen to work as the RBF kernel, where the explicit form of Gaussian function is expressed as follows:

$$\varphi(\|\boldsymbol{x} - \boldsymbol{x_i}\|) = e^{-\left(\frac{\|x-x_i\|}{\epsilon}\right)^2} \tag{4.8}$$

where ϵ is a parameter to control the shape of the Gaussian function. The implicit function $t(x)$ in the design domain can be interpolated via the RBF functions as:

$$t(x) = \sum_{i=1}^{N} \alpha_i \varphi_i(x) \tag{4.9}$$

where α_i is the expansion coefficient of the radial basis function positioned at the ith knot. The above equations can be rewritten as

$$\boldsymbol{t}(\boldsymbol{x}) = \boldsymbol{\phi}^{\boldsymbol{T}}(\boldsymbol{x})\boldsymbol{\alpha} \tag{4.10}$$

where

$$\boldsymbol{\phi}(x) = [\varphi_1(x), \varphi_2(x), \cdots \varphi_N(x)]^T, \ \ \boldsymbol{\alpha} = [\alpha_1, \alpha_2, \cdots \alpha_N]^{\boldsymbol{T}} \tag{4.11}$$

Using the RBFs to model the implicit function $t(x, y, z)$**,** we have

$$t(x, y, z) = \boldsymbol{\phi}^{\boldsymbol{T}}(x, y, z)\boldsymbol{\alpha_t} \tag{4.12}$$

where $\boldsymbol{\alpha_t}$ is the design variable, which directly determines the implicit function $t(x, y, z)$. The relationship between RBF knot and density is illustrated in Figure 4.2. While each density point is located at the center of each element of the FE mesh, the locations of RBF knots and density points can be independently chosen and do not need to coincide with each other. Therefore, the density field $\rho(x, y, z)$ can be constructed via the following expression:

$$\rho(x, y, z) = H_{a_0,c_0}(\boldsymbol{\phi}^{\boldsymbol{T}}(x, y, z)\boldsymbol{\alpha_t}) \cdot H_{a_1,c_1}(\boldsymbol{\phi}^{\boldsymbol{T}}(x, y, z)\boldsymbol{\alpha_t} - f(x, y, z)^2) \tag{4.13}$$

Note that the coordinate of (x, y, z) should be normalized accordingly to the range of $[0,1]^3$ for optimization purpose.

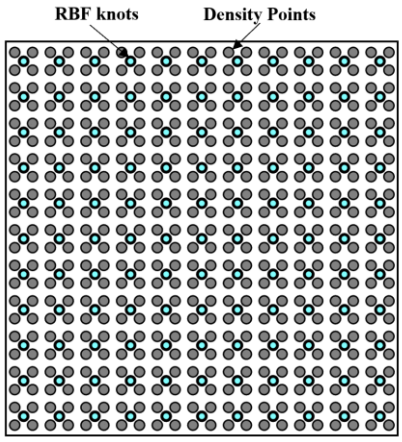

Figure 4.2 RBF knots and density points

4.2.2 Comparison with Homogenization-based Lattice Design

Homogenization-based functionally graded lattice design is a popular method in recent years [141, 142]. The general procedure of this method is as follows: a) Compute the effective mechanical properties of unit cell by Asymptotic Homogenization (AH) method [143], b) conventional density-based TO method with effective material properties computed based on AH, and c) lattice reconstruction based on density optimized results, where the volume fraction of each unit cell is directly determined by material density distribution from density-based TO method. The PIMM method can be classified as a non-homogenization method for lattice design based on implicit modeling. Compared with homogenization-based topology optimization, the pros and cons of the proposed method is listed as follows,

a) Size effect of lattice structures. The AH method is effective when the unit cell is sufficiently small in size compared to macrostructure, while the proposed method is not limited by unit cell size.

b) Several advanced homogenization-based lattice design methods have been proposed in recent years [118], where the configuration of the single unit cell is allowed to optimized and varied in space. However, the microscale topology is fixed for the proposed method.

c) Homogenization-based design method is not feasible for irregular porous scaffold designs [144], which is widely applied and preferred for tissue engineering. For example, Voronoi foam design [145], where there does not exist any periodicity in space, cannot be designed with homogenization-based method. However, because the irregular porous scaffold can be described by the implicit field, projection-based method proposed in this work can be readily applied in such situations.

d) The computational cost for the proposed method is higher than the homogenization-based method, especially when the length scale of unit cell is small. The proposed method is favorable for lattice design where the unit cell is large, while the homogenization is better for the situation where the length scale of unit cell is small.

e) Applying the RBF mapping method to describe the design domain increase the computational cost and implementation complexity compared with standard homogenization-based method.

4.3 Topology Optimization Formulation based on Implicit Modeling

4.3.1 Minimum Compliance

In this section, the implicit modeling method described in the section above is utilized to develop the TO formulation of compliance minimization [146]. The density field is controlled by RBF knots in the design domain. Hence, the TO will iteratively optimize functionally graded

lattice through updating the RBF knots in the design domain until the design achieve the optimal stiffness. Here, the RBF knots are defined as the design variables for evolving the true density field in the design domain during the optimization. Thus, the optimization problem can be expressed as:

$$\begin{cases} Find: \boldsymbol{\alpha_t} \\ Min: C(\boldsymbol{u}, \boldsymbol{\alpha_t}) = \frac{1}{2}\int_{\Omega} \boldsymbol{\varepsilon}(\boldsymbol{u})^T \boldsymbol{D}(\rho(\boldsymbol{\alpha_t}))\boldsymbol{\varepsilon}(\boldsymbol{u}) d\Omega \\ s.t: \frac{1}{|\Omega|}\int_{\Omega} \rho(\boldsymbol{\alpha_t}) d\Omega - V_{prescribe} \leq 0 \end{cases} \tag{4.14}$$

where C is the objective function defined by the structural compliance, $\boldsymbol{\alpha_t}$ is the weight vector of the RBF knots in the design space, ρ is the density distribution in the design domain Ω, and $V_{prescribe}$ is the prescribed volume fraction. In the finite element model, $\boldsymbol{u}$ is the unknown displacement field, $\boldsymbol{\varepsilon}$ is the strain, and $\boldsymbol{D}$ is the elastic tensor matrix.

4.3.2 Design Sensitivity Analysis based on Chain Rule

To obtain the sensitivity of objective function with respect to weights of RBF knots, the chain rule is employed. The adjoint method is applied to obtain the sensitivity with respect to the density field ρ:

$$\frac{\partial C}{\partial \rho} = \boldsymbol{\gamma}^T \frac{\partial \boldsymbol{K}}{\partial \rho}\boldsymbol{u} \tag{4.15}$$

where $\boldsymbol{\gamma}$ is the adjoint vector computed from the adjoint equation $\boldsymbol{K\gamma} = -\boldsymbol{f}$, and $\boldsymbol{K}$ is the assembled stiffness matrix, see Ref. [146]. According to the chain rule, the sensitivity of objective C with respect to design variables $\boldsymbol{\alpha_t}$ can be expressed as:

$$\frac{\partial C}{\partial \boldsymbol{\alpha_t}} = \sum_{i=1}^{nele} \frac{\partial C}{\partial \rho_i} \cdot \frac{\partial \rho_i}{\partial \boldsymbol{\alpha_t}} \tag{4.16}$$

where $nele$ is the total number of elements, and ρ_i denotes the density of ith element. We just simply describe the derivation of density ρ with respect to RBF knots $\boldsymbol{\alpha_t}$ as follows,

$$\frac{\partial \rho}{\partial \boldsymbol{\alpha_t}} = H_{a_0,c_0}{}'(\boldsymbol{\phi^T}(x,y,z)\boldsymbol{\alpha_t}) \cdot \boldsymbol{\phi}(x,y,z) \cdot H_{a_1,c_1}(\boldsymbol{\phi^T}(x,y,z)\boldsymbol{\alpha_t} - f(x,y,z)^2) +$$

$$H_{a_0,c_0}(\boldsymbol{\phi^T}(x,y,z)\boldsymbol{\alpha_t}) \cdot H_{a_1,c_1}{}'(\boldsymbol{\phi^T}(x,y,z)\boldsymbol{\alpha_t} - f(x,y,z)^2) \cdot \boldsymbol{\phi}(x,y,z) \quad (4.17)$$

where $H_{a_0,c_0}{}'(\cdot)$ and $H_{a_1,c_1}{}'(\cdot)$ denote the first derivative of H_{a_0,c_0} and H_{a_1,c_1}. The explicit formulation of $H_{a_0,c_0}{}'(\cdot)$ and $H_{a_1,c_1}{}'(\cdot)$ can be readily obtained using symbolic differentiation system, which is available in a build-in module in MATLAB [147].

4.4 Numerical Examples and Discussion

In this section, several 2D and 3D numerical examples are demonstrated in details on designing functionally graded gyroid lattice structures. The classic MBB beam in two dimensions is first investigated to demonstrate the effective of the proposed implicit modeling method for lattice design. The parameters for all numerical examples are chosen as: $a_0 = 50$, $c_0 = 0.2$, $a_1 = 500$, $c_1 = 0$, $\epsilon = 0.1$. The Method of Moving Asymptotes (MMA) is applied to solve optimization problem. The number of RBF knots in each direction are chosen based on our experience, less RBF knots result in simpler topology shape, while more RBF knots will inevitable increase computational cost. In this chapter, ten RBF knots along each direction are implemented in all numerical examples. Note that for two-dimensional problem, the implicit function for describing the lattice structure $f_{2D}(x,y,z)$ is chosen as follows:

$$f_{2D}(x,y) = \sin(\lambda_x x) \cdot \cos(\lambda_y y) \quad (4.18)$$

4.4.1 Compliance Optimization for MBB Design

The MBB-beam [148] is a popular test and benchmark problem in topology optimization. The symmetry is used for design, and the right half of the beam is modelled. The design of the MBB beam with the loading and boundary conditions is illustrated in Figure 4.3(a). The design domain is uniformly meshed by 200×200 elements with unit length. The prescribed volume fraction is set as 30%. The elastic constants are chosen as follows: elastic modulus E=1 and Poisson's ratio μ=0.3. The 10×10 uniformly distributed RBF knots are generated along two directions. The initial weights of RBF knots are chosen as 0.1. The periodicity parameters are selected as: $L_x = 0.1, L_y = 0.1$. The optimized design is plotted in Figure 4.3(b). As shown in the optimal results, the method proposed in this chapter is able to generate functionally graded lattice infill structures.

(a) MBB beam example (b) Optimal lattice infill design

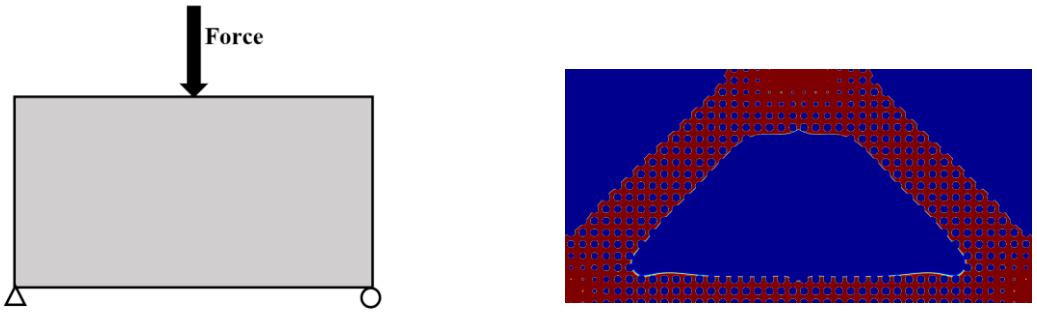

Figure 4.3 (a) MBB beam example (b) Optimal lattice infill design

4.4.2 Compliance Optimization for Three-dimensional Cantilever Beam Design

In this section, a three-dimensional cantilever beam example is presented for compliance optimization. The cantilever beam is modeled by a $200 \times 100 \times 60$ hexahedral mesh, and the

dimension of the design is demonstrated in Figure 4.4. A uniform line force $F = 1$ is applied on the right-bottom of the rectangle domain. The $10 \times 10 \times 10$ uniformly distributed RBF knots in the design domain. Note that $10 \times 10 \times 10$ uniformly distributed RBF knots applied here are only for implementation convenient, which will inevitable results in a difference of length scale in each direction. To obtain a cubic unit cell, the number of knots in every direction should be proportional to mesh number in each direction. However, it is worth to mention that our method is applicable to rectangle unit cell, which is generally not preferred for lattice optimization based on homogenization model. Note that left side of rectangle is fixed. The elastic constants are chosen as follows: Elastic modulus $E = 1$ and Poisson's ratio $\mu = 0.3$. The initial weights of RBF knots are chosen as 0.1, and the periodicity parameters are selected as: $L_x = 0.1$, $L_y = 0.1$, and $L_z = 0.1$. The optimization converges after 30 iterations presented in Figure 4.5(b). The optimized lattice infill result is presented in Figure 4.5(a).

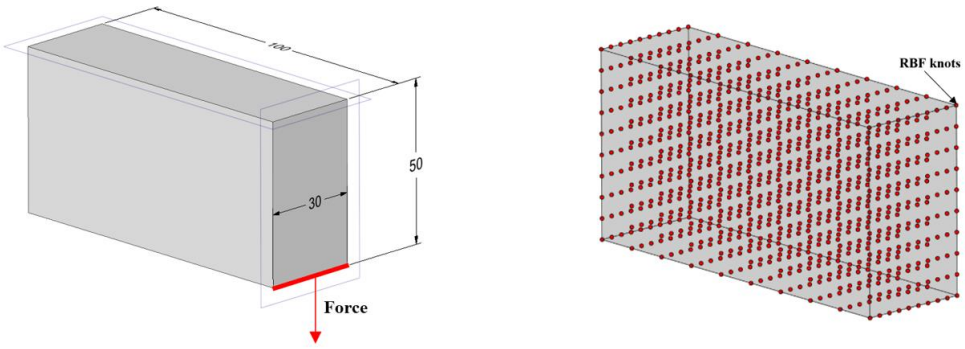

Figure 4.4 Three-dimensional Cantilever Beam and knots distribution

(a) Optimal lattice infill design (b) Convergence history

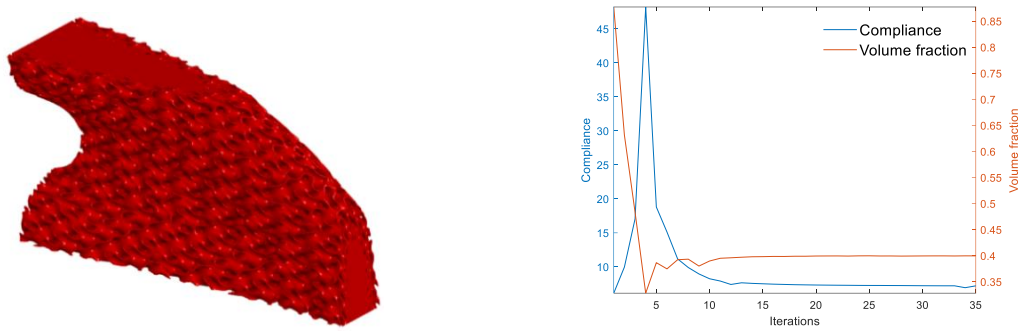

Figure 4.5 (a) Optimal lattice infill design (b) Convergence history

4.4.3 Compliance Optimization for 3D Bracket Design

In this section, a 3D Bracket Design example is presented for compliance optimization. The four corners are constrained by the planar joint with a point load $F = 1$ at the center as shown in Figure 4.6. The 3D Bracket is modeled by a $160 \times 160 \times 80$ hexahedral mesh, and the dimension of the design is demonstrated in Figure 4.6. The $10 \times 10 \times 10$ uniformed distributed RBF knots in the design domain. The initial weights of RBF knots are chosen as 0.1, and the periodicity parameters are selected as: $L_x = 0.1$, $L_y = 0.1$, and $L_z = 0.1$. The elastic constants are chosen as follows: Elastic modulus $E = 1$ and Poisson's ratio $\mu = 0.3$. Actually, the method proposed in this work is able to produce shape-preserving results which are preferred for AM, because 0-1 topology optimization designs sometimes cannot be manufactured such as overhangs, and support structures [149] beneath them are needed. Furthermore, removing support structures is time-consuming and requires additional post-processing. To produce shape-preserving design, the value of parameter c_0 in is set to be $c_0 = 0$. To make a comparison, two distinct optimization results with different values for parameter c_0 are demonstrated in Figure 4.7, and convergence

history for the two different designs is presented in Figure 4.8. The optimized compliance values are close for these two different designs. As shown in Figure 4.7(c-d), the optimized lattice structure is able to maintain the initial geometry configuration, where varied density lattice structures are generated, and materials tend to concentrate on four corners and loading point, and no block materials are removed. This shape preserving result is preferred for design of complex domain, where no overhang constraints are needed if the initial design domain is self-supported.

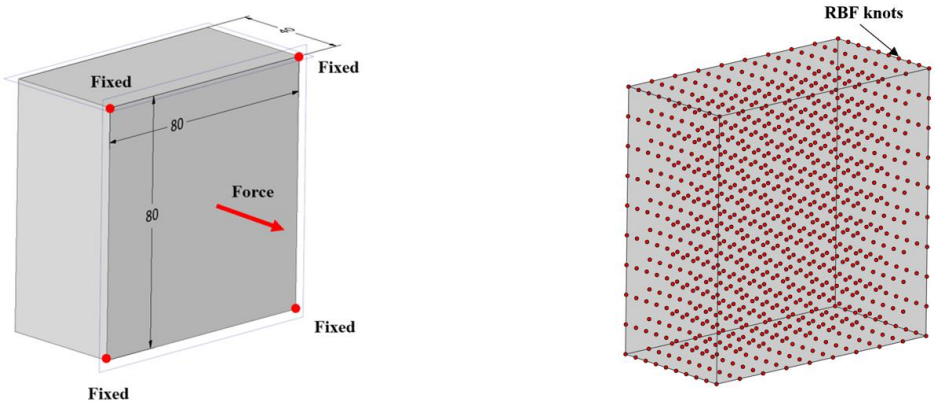

Figure 4.6 3D wheel Design and RBF knots distribution

(a) Front view ($c_0 = 0.2$) (b) Rear view ($c_0 = 0.2$) (c) Front view ($c_0 = 0$) (d) rear view ($c_0 = 0$)

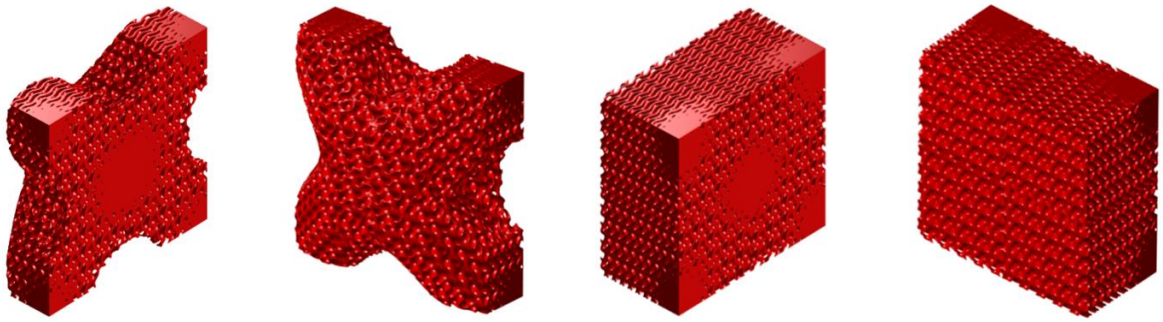

Figure 4.7 3D wheel Design ($c_0 = 0.2$): (a) Front view, and (b) Rear view; 3D wheel shape preserving design ($c_0 = 0$): (c) Front view and (d) Rear view

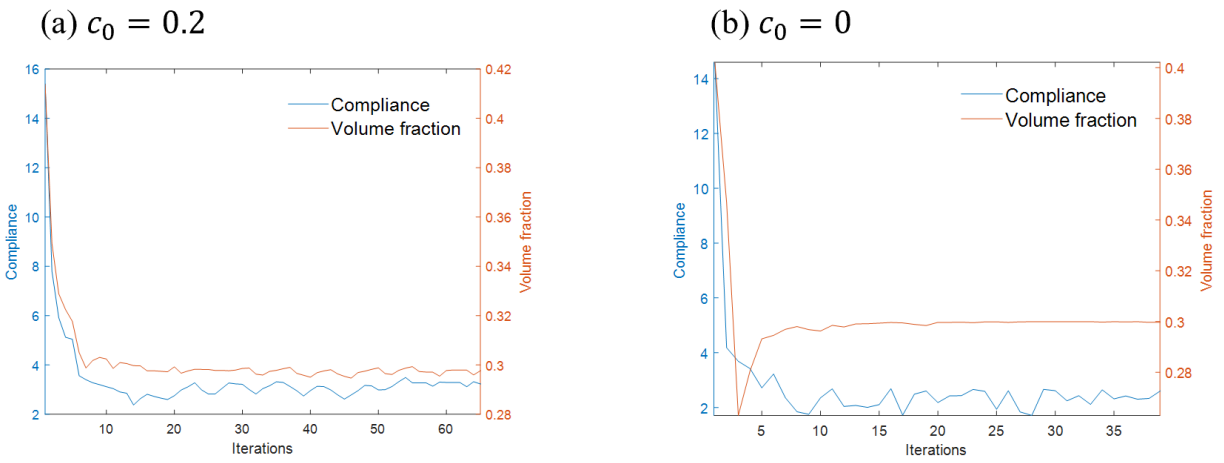

Figure 4.8 Convergence history for two design problems: (a) ($c_0 = 0.2$) and (b) ($c_0 = 0$)

4.5 Conclusion

In this chapter, a new projection-based algorithm based on implicit field for gyroid lattice design is proposed and demonstrated in details. The PIMM algorithm is able to design functionally graded lattice without the need for any homogenization. Thus, the lattice design based on this method is not limited to periodic structures, and can be extended to irregular porous scaffold designs. This point will be demonstrated and verified in the future. The unit cell size for lattice design can be large and not limited by size effects (homogenization necessary condition [150]), which is preferred for AM. Now that the geometry is defined by implicit function, the geometry information is far less than feature-based geometry modeling [151], which is sometimes extremely tedious for modeling porous media or lattice structures, and the data communication between implicit field with additive manufacturing systems is well-addressed by Ref. [134].

5.0 Reverse Shape Compensation via a Projection-based Moving Particle Optimization Method

5.1 Current Progress of Reverse Shape Compensation

Shape deformation under external environmental stimuli is a common phenomenon in nature or engineering [152]. Stimuli-responsive shape memory polymers (SMPs) have achieve remarkable advances in the past decade with a great potential application in biomedical devices, electronic engineering. etc. Shape memory polymers (SMPs) is an important stimuli-responsive polymer, which can recover their original shape when exposure to external stimuli. Many review papers have been published regarding the various SMPs, especially thermal responsive SMPs [153]. However, how to achieve a desired shape or prescribed shape with high accuracy under external stimuli is still a challenging problem. Similar issues can also be found in additive manufacturing. For example, in selected laser melting (SLM) process [154], the part deforms during printing process due to complex interrelated factors, including melt pool solidification, volumetric shrinkage, thermal cooling in the layer-by-layer building process. Due to this complexity, controlling shape deformation to achieve high geometric accuracy is very challenging but highly desirable especially for thin-walled structures. How to control the deformation of printed structures is critical for additive manufacturing processes. Recently, some related works are reported using shape compensation to reduce deformation in the manufacturing process rather than controlling the process parameters. These works are mainly dependent on experimental or simulation data to propose a geometry adjust strategy of the initial design to reduce the geometrical difference between the target shape and printed shape [155-157]. Lately, Afazov and co-workers

[158] developed a new distortion compensation method based on optical 3D scan measurements, where the proposed method are validated through experiment and verified that the mitigation of distortion in SLM is possible applicable for macro-scale components. Similar works regarding distortion compensation via combination between experiment and simulation in SLM can be found in Refs. [159, 160]. Applying mathematical programming approach to achieve a shape compensation is rarely reported in the previous research. Another application can be found in four-dimensional (4D) printing techniques. 4D printing [161-163], which is also known as shape-shifting 3D printing, use smart materials as raw material in additive manufacturing, the idea is basically to embed a smart behavior within a design. The structure printed by 4D techniques becomes the mechanism, and environment stimuli provides a passive source of energy which drives the mechanism to produce the desired behavior or shape. The same question arises here as how to design a shape to produce a desired deformed shape under external stimuli. Another potential application is design of 3D self-assembly structures. Self-assembly of complex structures is common in nature, which is a promising technique to fabricate small scale devices to achieve a deterministic 3D shapes under environmental stimuli. For example, Hua Li. etc. [164] proposed an analytical model of self-folding of thin-plates into a deterministic 3D shapes through fluid-solid interaction based on the beam theory. Similar research can be found in Refs. [165-168]. Thus, shape reverse compensation is one of the effective ways to resolve the above issues. The basic idea of shape compensation is that a displacement offset, obtained by multiplying the expected deformation of the intended shape with a factor of value between 0 and -1, is added to the desired shape so that the deformed shape under environment stimuli coincide with the desired shape. The detailed description of reverse shape compensation techniques can be found in Ref. [155]. In this chapter, a gradient-based moving particle optimization method is proposed in this chapter to

achieve reverse shape compensation, where a mapping from original geometry to deformed configuration is realized using radial basis function (RBF) kernel function. The core novelty of this chapter is to propose a generalized computational framework for reverse shape compensation based on mathematical programming theory which would result in a model without any loose parameter. As a proof-of-concept, the proposed method will be demonstrated on two-dimensional (2D) linear elastic design problems in this work and will be extended in the future to treat more complex situations arisen from additive manufacturing including SLM and 4D printing, and SMPs, 3D self-assembly design etc.

5.2 Formulation of Gradient-Based Moving Particle Optimization Method

The general shape compensation problem can be formulated as follows. To begin, select an arbitrary point $\boldsymbol{P}$ on the target geometry as an illustration. The geometry deforms under some external stimuli such as temperature, gravity, etc. The deformation mapping function $\mathcal{F}(\cdot)$ means that the point $\boldsymbol{P}$ will move to position $\mathcal{F}(\boldsymbol{P})$ under external stimuli. Let the added shape compensation to be $\boldsymbol{S}$, and the deformation of compensated point $\boldsymbol{P}+\boldsymbol{S}$ is denoted as $\mathcal{F}(\boldsymbol{P}+\boldsymbol{S})$, which is a function of shape compensation $\boldsymbol{S}$. The goal of shape compensation is to find $\boldsymbol{S}$ such that:

$$\boldsymbol{P}+\boldsymbol{S}+\boldsymbol{\mathcal{F}}(\boldsymbol{P}+\boldsymbol{S})=\boldsymbol{P} \tag{5.1}$$

Above equations can be rewritten as:

$$\boldsymbol{S}+\boldsymbol{\mathcal{F}}(\boldsymbol{P}+\boldsymbol{S})=\boldsymbol{0} \tag{5.2}$$

The deformation mapping function $\mathcal{F}(\cdot)$ can be a linear or nonlinear function. In this chapter, we use gravity to work as the external deformation stimulus, and finite element analysis (FEA) for the

structural analysis is based on linear elastic theory. The basic idea of the moving particle method is representing a geometry described by discrete particles arbitrarily located. As shown in Figure 5.1, a cube is represented by 11×11 particles, where each particle is independent from others and can move arbitrarily in the prescribed design domain. To compute the deformation of the cube under the gravity field, the particles are first projected onto a finite element mesh to perform FEA with prescribed boundary conditions. The radial basis function (RBF) [139] is introduced here to map the particle to the FE mesh. The RBFs are a well-known tool to interpolate scattered data to generate smooth surface. Radial basis functions are radially symmetric functions centered at a specific point, named as RBF knot, which can be expressed as follows:

$$\varphi(\boldsymbol{x}, \boldsymbol{X_i}) = \varphi(\|\boldsymbol{x} - \boldsymbol{X_i}\|) \tag{5.3}$$

where $\|\cdot\|$ denotes the Euclidean norm and $\boldsymbol{X_i}$ is the position of the knot. There are several possible radial basis functions, including thin-plate spline, Gaussians [140], etc. In this chapter, The Gaussian function is chosen to work as an RBF kernel, the explicit form of Gaussian function is expressed as follows:

$$\varphi(\|\boldsymbol{x} - \boldsymbol{X_i}\|) = e^{-\left(\frac{\|x - X_i\|}{\epsilon}\right)^2} \tag{5.4}$$

where ϵ is a parameter to control the shape of the Gaussian function, and e denotes the exponential function. The function $f(x)$ (i.e. density field of the deformed and undeformed configuration) in the design domain can be interpolated using RBF functions as:

$$f(x) = \sum_{i=1}^{N} \alpha_i \varphi(\boldsymbol{x}, \boldsymbol{X_i}) \tag{5.5}$$

where α_i is the expansion coefficient of the RBF positioned at the ith knot. Above equation can be rewritten as:

$$\boldsymbol{f(x)} = \boldsymbol{\phi^T(x, X)\alpha} \tag{5.6}$$

where

$$\boldsymbol{\phi}(\boldsymbol{x},\boldsymbol{X}) = [\varphi(\boldsymbol{x},\boldsymbol{X_1}),\varphi(\boldsymbol{x},\boldsymbol{X_2}),\cdots\varphi(\boldsymbol{x},\boldsymbol{X_N})]^T,\ \ \boldsymbol{\alpha} = [\alpha_1,\alpha_2,\cdots\alpha_N]^{\boldsymbol{T}} \tag{5.7}$$

For the projection from the particle to the FE mesh, the formulation can be written as:

$$\boldsymbol{\rho}_{fem}(\boldsymbol{x}_{fem}) = H(\boldsymbol{\phi}^{\boldsymbol{T}}(\boldsymbol{x}_{fem},\boldsymbol{x}_p)\cdot\boldsymbol{I}) \tag{5.8}$$

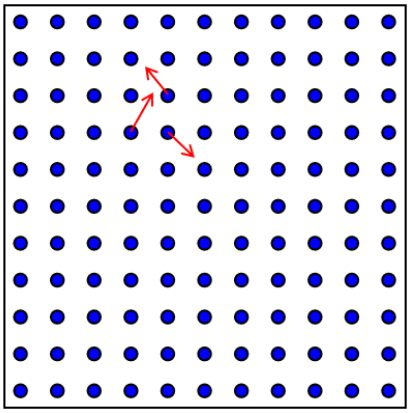

Figure 5.1 Geometry represented by moving particles

The FEA is based on the density field $\boldsymbol{\rho}_{fem}$ of the projected geometry deforms under gravity field. We define the concept of dual background mesh as shown in Figure 5.2 to formulate our optimization problem. Note that the nodal location of the FE mesh denotes as $\boldsymbol{X}_{fem}$, and the deformation under gravity is $\boldsymbol{U}_{fem}$. Thus, the deformed position $\boldsymbol{X}_d$ can be expressed as:

$$\boldsymbol{X}_d = \boldsymbol{X}_{fem} + \boldsymbol{U}_{fem} \tag{5.9}$$

After computing the deformation via FEA, the deformed shape is projected onto a fixed grid (fictitious mesh) using the RBF kernel. The density field in the fictitious domain can be written as:

$$\boldsymbol{\rho}_f(\boldsymbol{x}_\Omega) = H(\boldsymbol{\phi}^{\boldsymbol{T}}(\boldsymbol{x}_\Omega,\boldsymbol{X}_d)\cdot\boldsymbol{\beta}) \tag{5.10}$$

where $\boldsymbol{x}_\Omega$ is the centroid of the fictitious mesh. $\boldsymbol{\beta}$ is the expansion coefficient, which can be expressed as,

$$\boldsymbol{\beta} = H(\boldsymbol{\phi}^{\boldsymbol{T}}(\boldsymbol{X}_{fem},\boldsymbol{x}_p)\cdot\boldsymbol{I}) \tag{5.11}$$

(a) Finite element mesh (b) Fictitious mesh

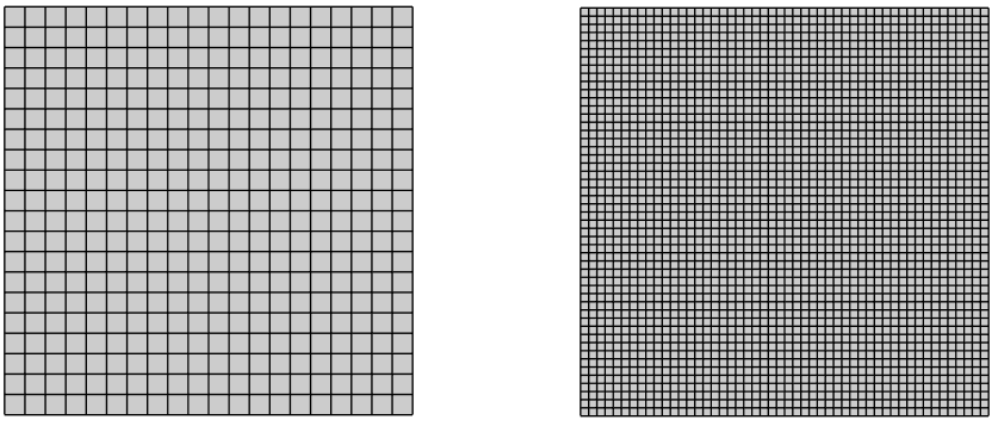

Figure 5.2 Dual background mesh (a) Finite element mesh, (b) Fictitious mesh

Note that the dual mesh as shown in Figure 5.2 is independent with each other, and mesh size can be different. As shown in Figure 5.3, the rectangle is discretized by uniformly distributed particles. The projected density field for FEA is plotted in Figure 5.3(b), and the deformed shape in the fictitious domain is presented in Figure 5.3(c).

(a) Particle distribution (b) Density field in FE mesh (c) Density field in fictitious domain

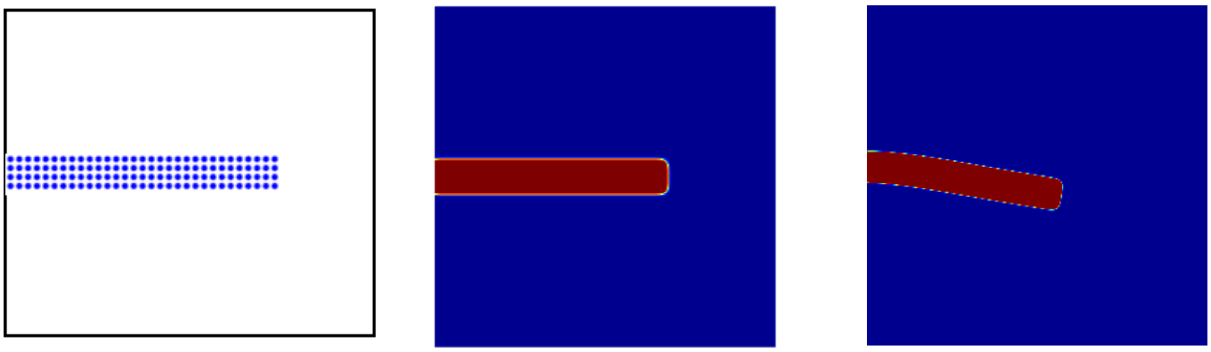

Figure 5.3 (a) Particle distribution, (b) Density field in the FE mesh, (c) Density field in fictitious domain

5.3 Optimization Formulation and Sensitivity Analysis

As described in above section, the density field in the fictitious domain $\boldsymbol{\rho}_f$ is controlled by the particle position. The target geometry is also represented in the fictitious domain using density field $\boldsymbol{\rho}_{obj}$. The objective is to minimize the difference between the density field between $\boldsymbol{\rho}_f$ and $\boldsymbol{\rho}_{obj}$. Thus, the optimization problem can be formulated as follows:

$$\begin{cases} \text{Minimize: } \chi = \frac{1}{2}\left(\boldsymbol{\rho}_f(\boldsymbol{x}_p) - \boldsymbol{\rho}_{obj}\right)^T\left(\boldsymbol{\rho}_f(\boldsymbol{x}_p) - \boldsymbol{\rho}_{obj}\right), \ \left(\underline{\boldsymbol{x}_p} < \boldsymbol{x}_p < \overline{\boldsymbol{x}_p}\right) \\ \text{subject to: } \boldsymbol{K}(\boldsymbol{\rho}_{fem})\boldsymbol{U}_{fem} = \boldsymbol{f} \end{cases} \tag{5.12}$$

where $\boldsymbol{f}$ is the self-weight loads due to gravity, and $\underline{\boldsymbol{x}_p}$ and $\overline{\boldsymbol{x}_p}$ denote the lower and upper limits of design variables. $\boldsymbol{\rho}_{fem}$ is density field use for FEA. For the structure meshed with four-node quadrilateral elements, $\boldsymbol{K}$ is global stiffness matrix and $\boldsymbol{U}_{fem}$ is the corresponding node displacement. The elemental self-weight load vector can be expressed as [169],

$$\boldsymbol{f} = V\rho g\bar{\boldsymbol{f}} \tag{5.13}$$

$$\bar{\boldsymbol{f}} = [0 \quad -0.25 \quad 0 \quad -0.25 \quad 0 \quad -0.25 \quad 0 \quad -0.25]^T \tag{5.14}$$

where g is the gravity parameter. ρ is element density, and V is volume of each element. The detailed implementation of the proposed optimization framework is described in the flowchart as shown in Figure 5.4. Note that the FEA is based on linear elastic theory, and hence material and geometry nonlinearity are not considered in this chapter, which will be investigated in the future.

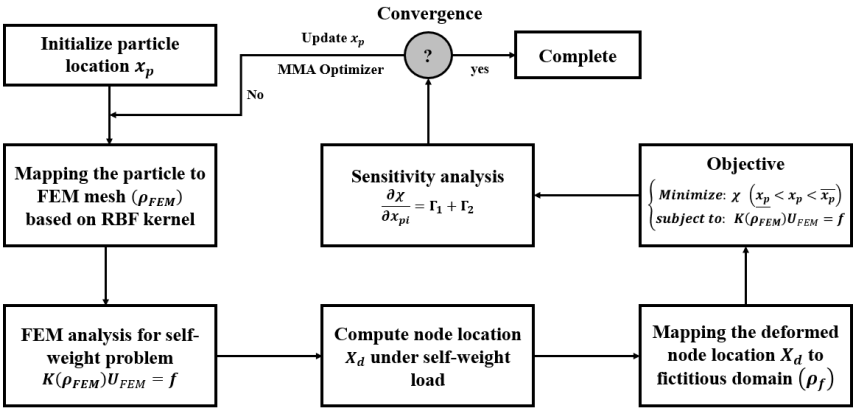

Figure 5.4 Optimization flow of the proposed gradient-based shape compensation method

5.4 Shape Interpolation based on Artificial Neural Network (ANN)

Applying the RBF-based particle method to represent geometry model is hard to capture the intricate surface feature near the boundary. In most cases, accurate describing complex shape needs large number of particles, which inevitable results in high computational cost. In fact, there is no need to use highly dense particles to predict the deformation. A small number of particles which are capable to capture the major mechanical feature of target shape are sufficient to describe the basic deformation pattern, and other deformation mode of tiny intricate feature can be directly interpolated with interpolation techniques. Shape interpolation technique is a hot topic in computer animation. In computer animation field, shape interpolation is to create a sequence of intermediate shapes form two or multiple given poses of an object, which allows generating a shape sequence based on key frames designed by artist. In recent years, several interpolation methods are proposed to generate intermediate shapes based on key frames as described in Ref [170-172]. We borrow this concept to achieve shape reconstruction based on basic deformation pattern. An interpolation technique based on artificial neural network is proposed here to reconstruct the accurate geometry

deformation. The detailed shape reconstruction algorithm is described as follows. Consider a shape represented by point cloud as shown in Figure 5.5. The blue point and red point denote the undeformed and deformed shape, respectively. Assume that the deformed pattern of point cloud with sparse points is known, the goal is to predict the deformation pattern of dense point cloud. The mathematical formulation can be written as follows,

$$(u, v) = \mathcal{F}(x, y) \tag{5.15}$$

where (x, y) denotes the initial position of point. $\mathcal{F}$ is a unknow mapping function needed to be determined, u and v denote the deformation in x or y direction. The feedforward networks [173], with one or more layers between the input and output layers, are mainly used for function approximation. The typical architectures of feedforward networks are illustrated in Figure 5.5, which contains input, hidden layers, and output. The mathematical formulation of deep feedforward neural networks can be defined as,

$$\mathbb{N}(x, y, \boldsymbol{\theta}) = \mathbb{N}\left(\boldsymbol{a}^{(L+1)}\left(\boldsymbol{h}^{(L)}\left(\boldsymbol{a}^{(L)}(\ldots \boldsymbol{h}^{(1)}(\boldsymbol{a}^{(1)}(x, y))\right)\right)\right) \tag{5.16}$$

where $\mathbb{N}$ denotes feedforward networks, and the $\boldsymbol{\theta}$ is parameter of network. The hidden layer is defined as $\boldsymbol{h}^{(l)}(\boldsymbol{x})$, a network with L hidden layers can be expressed as, where $\boldsymbol{a}^{(l)}(\boldsymbol{x})$ is a linear operation, expressed as**,**

$$\boldsymbol{a}^{(l)}(\boldsymbol{x}) = \boldsymbol{W}^{(l)}\boldsymbol{x} + \boldsymbol{b}^{(l)} \tag{5.17}$$

where $\boldsymbol{W}^{(l)}$ is weight matrix and $\boldsymbol{b}^{(l)}$ is bias vector for the $l\ th$ layer**.** The weight matrix $\boldsymbol{W}^{(l)}(\boldsymbol{l} = \boldsymbol{1}, \boldsymbol{2}, \cdots \boldsymbol{L})$ and bias $\boldsymbol{b}^{(l)}(\boldsymbol{l} = \boldsymbol{1}, \boldsymbol{2}, \cdots \boldsymbol{L})$ can be combined into a single parameter $\boldsymbol{\theta}$**.** $\boldsymbol{h}^{(l)}(\boldsymbol{l} = \boldsymbol{1}, \boldsymbol{2}, \cdots \boldsymbol{L})$ are hidden-layer activation functions (kernel functions). In fact, ANN is a universal approximator for nonlinear functions. It has been proven that a three-layer feedforward neural networks can approximate any continuous multivariate function to any accuracy [174]. Here, we apply the feed forward neural network to represent mapping function $\mathcal{F}(\cdot)$ as follows,

$$\mathcal{F}(x, y) = \mathbb{N}(x, y, \boldsymbol{\theta}) \tag{5.18}$$

where $\boldsymbol{\theta}$ is unknown weights and biases. The objective function of training process can be written as follows,

$$\begin{cases} Find: (\boldsymbol{\theta_1}, \boldsymbol{\theta_2}) \\ Min: \sum_{i=1}^{N} (\|\mathbb{N}_1(x_i, y_i, \boldsymbol{\theta_1}) - u(x_i, y_i)\|_2 + \|\mathbb{N}_2(x_i, y_i, \boldsymbol{\theta_2}) - v(x_i, y_i)\|_2) \end{cases} \tag{5.19}$$

where $\mathbb{N}_k$ $(k = 1,2)$ is the feedforward neural network, and (x_i, y_i) is the point where the deformation pattern is known. Two independent networks are applied to approximate *u* and *v*, respectively. Operator $\|\cdot\|_2$ denotes 2-norm. (x, y) denotes the coordinate of point. The backpropagation learning algorithm [175] is applied here to train the neural networks. The activation function is chosen as hyperbolic tangent function. The training network used in this chapter has four hidden layers, and each layer of network contains 10 neurons. The optimized weights and biases are obtained once the training process converging. The deformation pattern of new point (dense point cloud) can be directly predicted using trained networks $\mathbb{N}_k$ $(k = 1,2)$ as following,

$$\begin{cases} u_e = \mathbb{N}_1(x_e, y_e, \boldsymbol{\theta_1}) \\ v_e = \mathbb{N}_2(x_e, y_e, \boldsymbol{\theta_2}) \end{cases} \tag{5.20}$$

(x_e, y_e) is the position of the new point.

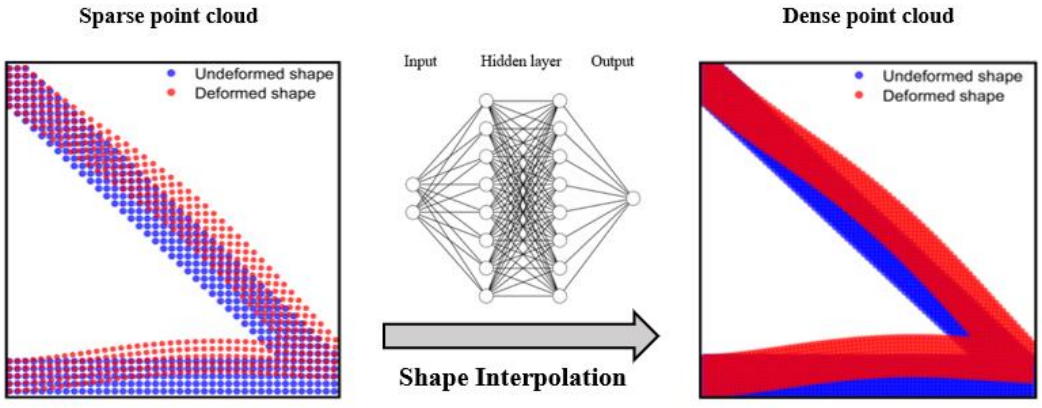

Figure 5.5 Shape interpolation based on neural networks

5.5 Numerical Examples

In this section, two 2D numerical examples are demonstrated to illustrate performance of the proposed method for shape compensation. Unless stated otherwise, the following material parameters are assumed as: $E = 1$ for material elastic modulus and Poisson's ratio $\mu = 0.3$. The shape is represented by level set of density field ($\rho = 0.1$), and FEA is based on the linear elastic model. In the FE model, the 200×200 equal sized planar 4-node elements with element length 0.2 are generated. The mesh of fictitious domain is coincident with FE mesh. Note that the move limit of MMA optimizer is chosen as $m = 0.005$. It is worth to mention that the discretization of target shape is chosen as initial distribution of particles.

5.5.1 Reverse Shape Compensation for Self-weight Horizontal Cantilever Beam

In the first example, a simple horizontal cantilever beam (Figure 5.6) is the target geometry, which is discretized by 4×31 particles as shown in Figure 5.7. The target geometry is a horizontal rectangle with a fixed boundary on the left side. The geometry deforms under self-weight loads, where the gravity parameter is chosen as $g = 0.02$. The width of the RBF kernel function is chosen as 0.6. The mapping geometry in the FE mesh is plotted in Figure 5.8(a), which works as the target density field. The deformed configuration of initial shape under self-weight loads is presented in Figure 5.8(b). The objective is to achieve a reverse shape compensation so that the deformed shape is as close to the target shape (Figure 5.8 (a)) as possible. The initial particle position is plotted in Figure 5.7(a), and the optimal particle position can be found in Figure 5.7(b). The optimization evolution progress is plotted in Figure 5.10. The optimal shape is demonstrated in Figure 5.9(a),

where the deformed shape in fictitious domain is plotted in Figure 5.9(b). The optimization progress converges after 80 iterations and convergence history is presented in Figure 5.10.

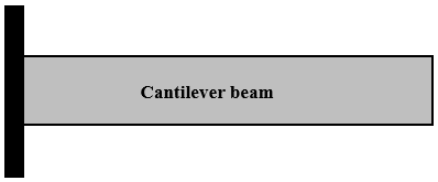

Figure 5.6 Cantilever beam

(a) Initial configuration (b) Optimal configuration

Figure 5.7 Particle distribution (a) Initial configuration (b) Optimal configuration

(a) Undeformed configuration (b) Deformed configuration

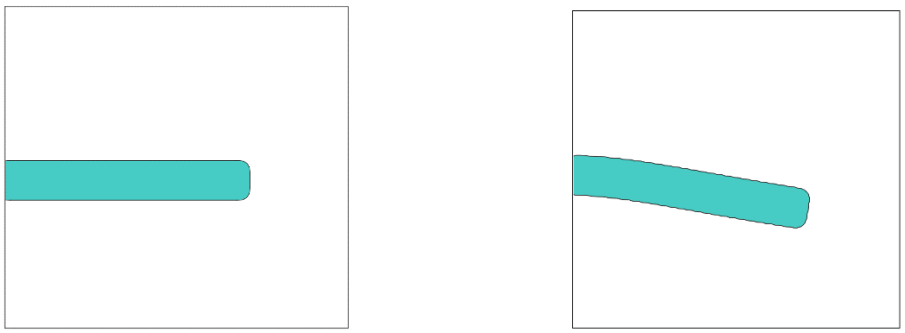

Figure 5.8 Initial geometry shape (a) Undeformed configuration (b) Deformed configuration

(a) Undeformed configuration (b) Deformed configuration

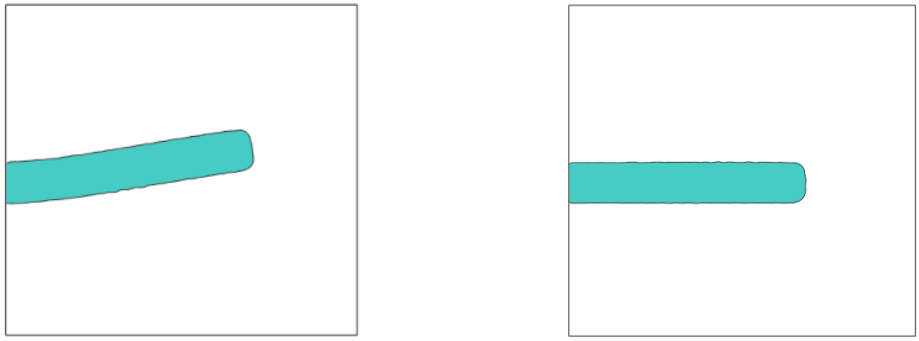

Figure 5.9 Optimal geometry shape (a) Undeformed configuration (b) Deformed configuration

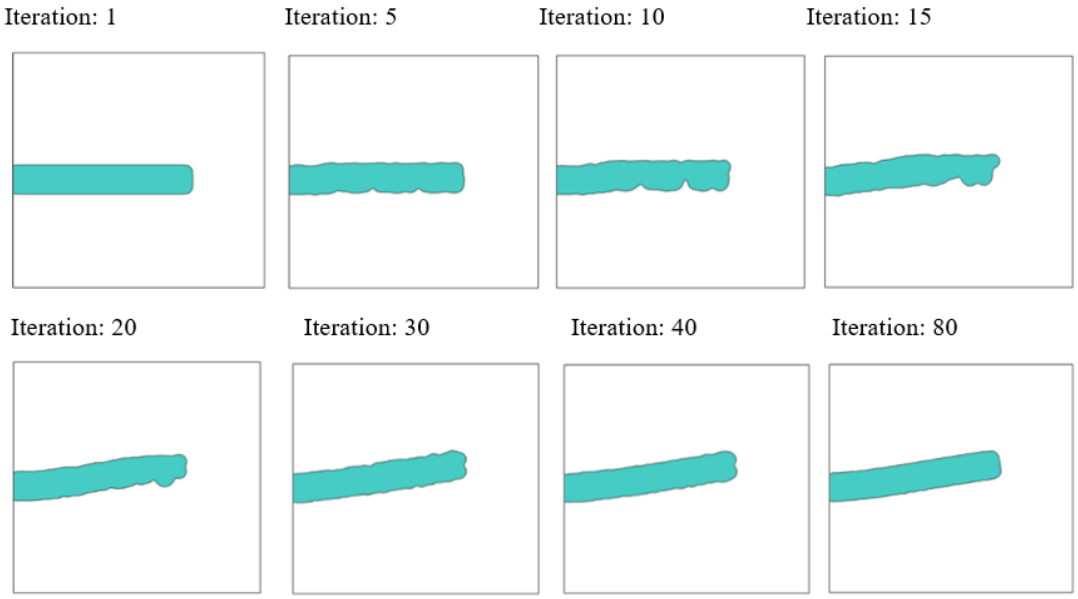

Figure 5.10 Shape evolution during optimization

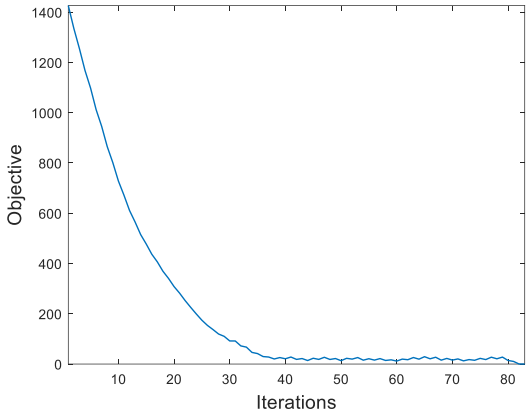

Figure 5.11 Convergence history

5.5.2 Reverse Shape Compensation for Truss Structures

Truss structures or thin-walled structures are widely used in engineering. The reverse shape compensation design problem of truss structures is investigated in the present study. Three different truss structures are presented in Figure 5.12 to work as target shape, where the left side of truss structures is fixed. The gravity parameter is chosen as g=0.1, while the other parameters remain the same as the previous examples. The optimal particle distribution and configuration are presented in Figure 5.13 and Figure 5.14. The convergence history is plotted in Figure 5.15. It is worth to mention that one layer of particles is capable to capture the major geometric feature of target shape, while some small features like sharp corner is blurred. To accurate reconstruct the real optimized shape, the shape interpolation technique is implemented. The reconstructed geometric shapes are presented in Figure 5.16.

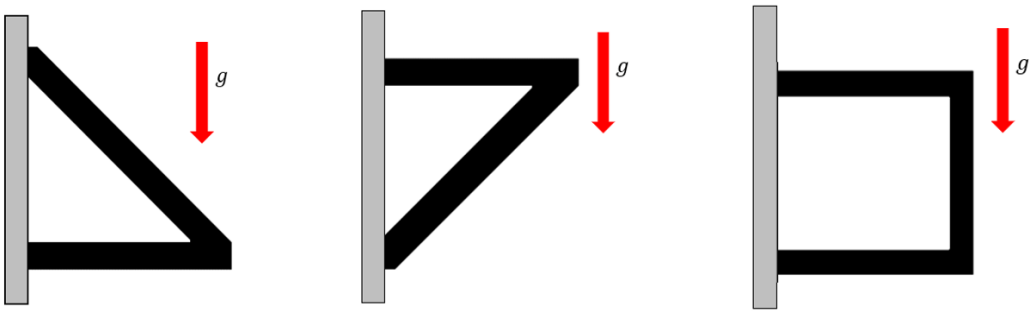

Figure 5.12 Geometric prototype

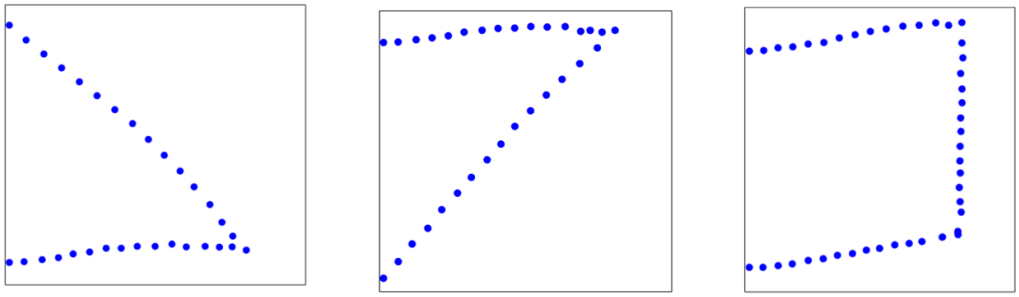

Figure 5.13 Optimal particle distribution

Figure 5.14 Optimal configuration

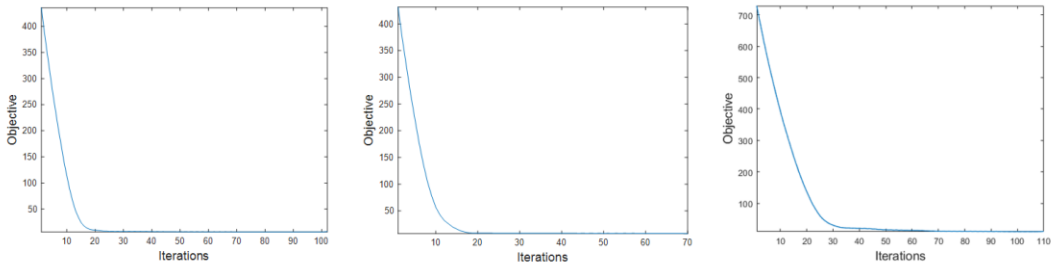

Figure 5.15 Convergence history

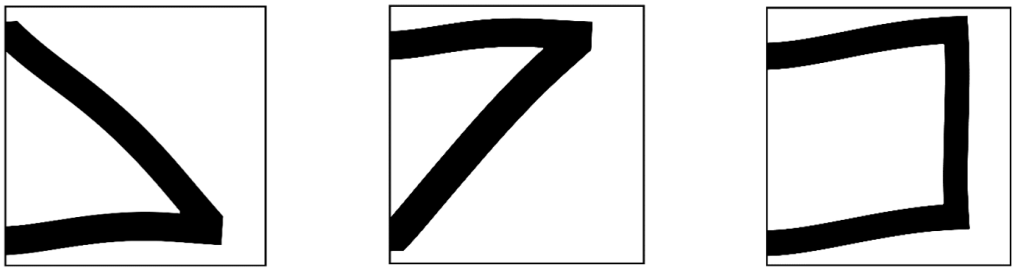

Figure 5.16 Shape reconstruction

5.6 Conclusions

In this chapter, a gradient-based moving particle optimization method is proposed to achieve reverse shape compensation under gravity stimuli. The geometry is represented by particles, where each particle can move freely in the design domain. Dual background mesh is implemented to achieve a mapping from undeformed geometry to deformed configuration. The update of particle positions is based on sensitivity information, and MMA optimizer is implemented to minimize the objective function. Two numerical examples are demonstrated in detail, where different target shapes and boundary conditions are examined to verify the effectiveness of the proposed method. As shown in numerical examples, the optimal shape is

reasonable from mechanics point of view, and no voids or gaps are generated inside the shape. The method described here is a general computational framework for reverse shape compensation, which has the capability to treat more complex situation, such as temperature change. etc. Meanwhile, further study regarding geometric and material nonlinearity will be conducted in the future. Besides, the proposed method has the potential to be applied to engineering application such as distortion compensation in additive manufacturing or four-dimensional (4D) printing techniques

6.0 A Density-based Boundary Evolving Method for Buckling-induced Design under Large Deformation

6.1 Current Progress of Large Deformation Design with Topology Optimization

Structural topology optimization is a tool for distributing material in a prescribed domain to obtain optimized structural performance through an optimal way. In recent years, designing the flexible electronics, soft robots and wearable electronic devices draws great attention from academia and industry due to their extraordinary mechanical response [53-55]. Such devices and structures usually experience large deformations under external loading conditions, which is different from the traditional stiff structure design. Recently, topology optimization methods are utilized to design flexible and soft structures based on finite deformation theory. For the SIMP method, Bruns and Tortorelli [56] embedded a filtering scheme into SIMP method to design compliant mechanism, where the geometric and material nonlinearities are considered. Wallin et al [57] compared different stiffness measurement for compliant mechanism design under large deformation. Fengwen et al [58] proposed a new energy interpolation scheme to stabilize the numerical simulations for topology optimization, where the mesh distortion phenomenon is alleviated when structures undergo large deformation. Ivarsson et al [59] applied a transient finite strain viscoplastic model in gradient-based topology optimization framework to design impact mitigating structures. Li et al [60] extended the shape preserving topology optimization approach from linear elastic case to geometrically nonlinear problems, where the structural complementary elastic work is chosen as objective function. Luo et al [61] proposed a simple and effective additive hyperelasticity technique to circumvent excessive mesh distortion in solving the density-based

topology optimization of elastic structures undergoing large deformation. Ortigosa et al [62] proposed a novel stabilized computational approach for SIMP-based TO method for hyperelastic material design subjected to very large deformation. For level set method, Chen et al [63] proposed an effective level-set-based topology optimization method for the design of hyperelastic structures undergoing large deformation. Luo et al [64] presented an effective topology optimization methodology for the compliance design of hyperelastic material with frictionless contact supports. Chung et al [65] proposed a level-set based topology optimization method for designing structures undergoing large deformation due to thermal and mechanical loads, where the thermo-mechanical response can be controlled via topology optimization. Xue et al [66] performed structural topology optimization under finite deformation using explicit geometry description, where a Moving Morphable Void (MMV)-based approach is developed for designing large deformation mechanism. Kato et al [67] proposes a method of micro-macro concurrent topology optimization for a two-phase nonlinear solid to minimize the end compliance of its microstructure undergoing large deformation. Some other related works can be found in Ref [68-71].

For structures experiencing large deformation, local buckling phenomenon always happens, which makes the force-displacement response highly nonlinear. Compared with topology optimization design under finite deformation, designing buckling-induced device is more challenging. Structural instability such as snap-through behavior is widely found in nature. At the beginning, buckling behavior is undesirable in engineering due to the resultant capacity reduction and catastrophic failure. Other than reduction of load-carrying capacity, high-rate motion and sudden energy release are two critical features of many buckling phenomena. For example, the designs are capable of snapping from their initial shape to a buckled shape with a significant

amount of energy release, and a load drop, named as negative stiffness, can be found in force-displacement response. Because of these two features, buckling behavior becomes an ideal mechanism for adaptive and smart applications [176]. Several successfully applications are found in recent years, such as design of absorbers [177], dampers [178], isolators [179], self-locking structures [180], and morphing structures [181], etc. Limited applications of topology optimization in buckling-induced design undergoing large deformation are found in recent years. Bruns et al [182] developed a robust arc-length method and applied this method in topology optimization problem to design structures that exhibit snap-through. Bruns and Sigmund [183] developed a general approach for the design of mechanisms that experience more complex snap-through behavior, where a multiphase design strategy is outlined. Lindgaard and Dahl [183] studied different compliance and buckling criterion and applied for topology optimization of a point loaded curved beam problem to maximize the snap-through buckling load. James and Waisman [21] proposed a novel design method based on TO for a bi-stable cardiovascular stent device, which is able to snap into expanded configuration under a small trigger force. Bhattacharyya et al [184] proposed a novel method to design a camber morphing mechanism for a bi-stable airfoil based on topology optimization.

The level set and density-based methods for topology optimization are often regarded as two different approaches, which results in two competing and parallel research directions with little overlap. The density-based method is convenient to derive the sensitivities and easy for programming, which also present a better numerical stability during optimization [2]. Level set method does not require penalization of intermediate densities and a clear solid-void interface can be found during optimization. Andreasen et al [185] pointed out that these two methods share more

similarity instead of difference, where a crisp interface level set optimization approach based on a cut element method is proposed. This algorithm is still in the framework of density-based method, while the clear solid-void boundary can be found during optimization. Here, an alternative computational scheme is proposed to combine the advantages of two approaches for buckling-induced design, where the boundary of topology is described in an explicit way based on RBF interpolation. It is worth to mention that the proposed computational method is in the framework of density-based method. Compared to the existing explicit TO method such as MMV or projection-based method, the differences are listed below:

a) The MMV approach is in the framework of level set method, where shape sensitivity is required for topology optimization [186]. Instead of using RBF function to describe the boundary, the MMV method apply smooth closed B-splines to explicitly represent the boundary of voids.
b) For the MMV method, the merger of multiple void components is based on reconstructing B-spline curves as described in Ref. [187]. For the method proposed in this chapter, a simple merger method based on the p-norm function is implemented.
c) The proposed method is in the framework of density-based approach, where the sensitivity of standard density-based TO method can be directly employed to obtain the design sensitivity via the chain rule. Note that shape sensitivity is not required for optimization as in MMV.
d) Compared with existing projection-based method proposed by Narato et al [188]. Instead of describing solid component, we explicit describe the boundary of void geometry with RBF functions, where the shape is controlled by RBF knots instead of fixed geometry primitives. Meanwhile, the geometry components do not disappear during optimization so that the intermediate density is only near the boundary region.

6.2 A Projection-based Boundary Evolving Method

Geometry projection method proposed by Norato et al [188] applies discrete geometry component to represent density field (solid region) based on distance function. Instead of representing the solid area, we use the discrete geometry component to represent the void area in this chapter. To achieve more design freedom, the void area is described by boundary represented by RBF function in polar coordinate as shown in Figure 6.1. Compared with bar representation, geometry shape described in polar coordinate has more flexibility and some typical shapes described in polar coordinate are presented in Figure 6.2. The basic idea is that the design can be generated through removing the void area from the initial design domain as shown in Figure 6.3. Note that the boundary of void is described using RBF formulation in polar coordinate, which will be demonstrated in the following section.

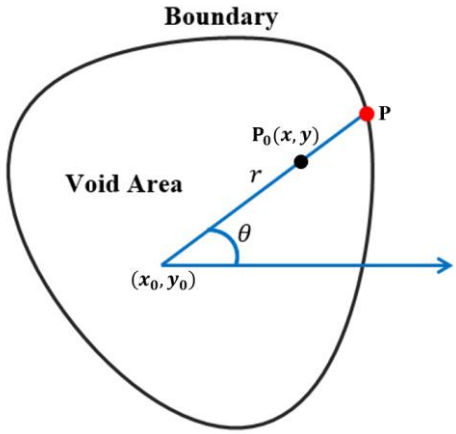

Figure 6.1 Curve described in polar coordinate

(a) $r = 1$ (b) $r = |sin(2\theta)|$ (c) $r = 1 + \cos(\theta)$ (d) $r = |sin(3\theta)|$

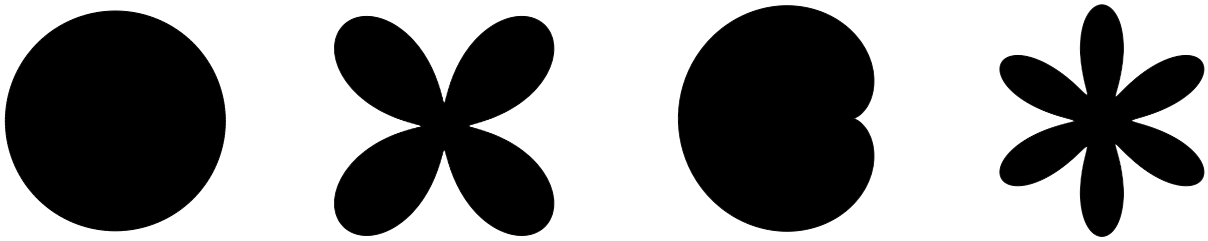

Figure 6.2 Basic shapes described in polar coordinate

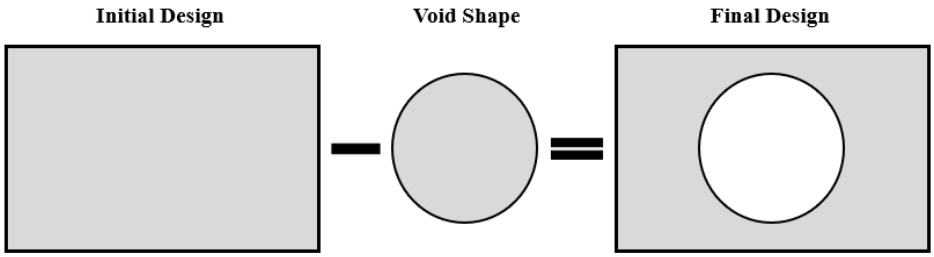

Figure 6.3 An illustration of design with void representation

To describe the shape of void in an explicit way, a parametrized projection for void description based on distance function in polar coordinate can be defined as follows,

$$\mathcal{F}(x, y; x_0, y_0) = \mathrm{H}\left(\sqrt{(x - x_0)^2 + (y - y_0)^2} - r(\theta)\right) \tag{6.1}$$

where (x_0, y_0) is the origin of polar coordinate, (x, y) is the coordinate of arbitrary point P_0 in the design domain, and $r(\theta)$ is the distance from point P on the shape boundary to the origin of polar coordinate (see Figure 6.1). Also, $\mathrm{H}(\cdot)$ denotes the Heaviside function defined as:

$$\mathrm{H}(\Delta) = \frac{1}{1+e^{-\Theta(\Delta-\mu)}} \tag{6.2}$$

where Θ and μ are two parameters to control the shape of Heaviside function. Δ is the input of Heaviside function. The effect of parameter Θ on density field can be found in Figure 6.4. The value of these two parameters are chosen as $\Theta = 100, \mu = 0$ in this chapter. Note that the

intermediate density only exist near the boundary as shown in Figure 6.4(c), where the ersatz material approach is implemented to describe the material behavior near the boundary. This material interpolation scheme is the same as standard level set method proposed by Allaire et al [10].

(a) $\Theta = 10$ (b) $\Theta = 50$ (c) $\Theta = 100$

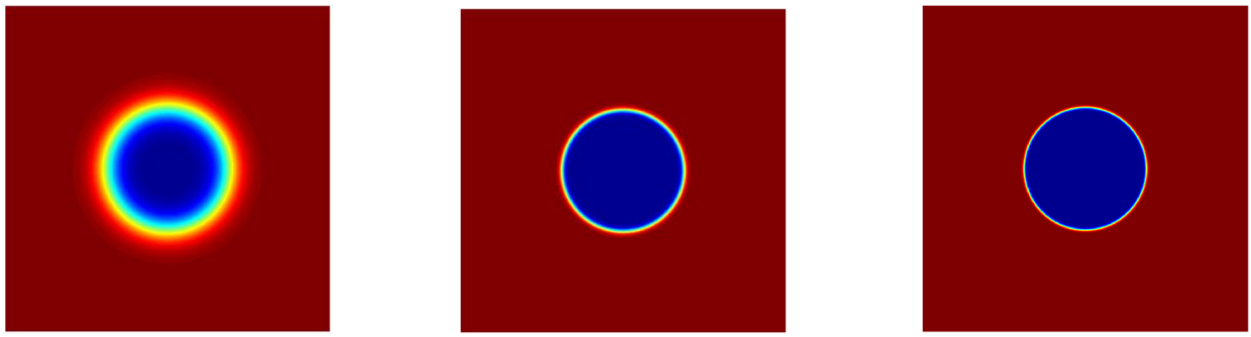

Figure 6.4 The effect of parameter Θ on density field

To effectively represent the boundary of void with a single globally continuous and differentiable function**,** the radial basis functions [139] are introduced here to describe the boundary shape. The RBFs can interpolate scattered data to generate smooth surface and is an effective way to approximate complex function. Radial basis functions are radially symmetric functions centered at a specific point, called an RBF knot, which can be expressed as follows:

$$\varphi_i(\boldsymbol{x}) = \varphi(\|\boldsymbol{x} - \boldsymbol{x_i}\|) \tag{6.3}$$

where $\|\cdot\|$ denotes the Euclidean norm and x_i is the position of the knot. There are several possible radial basis functions, including thin-plate spline, Gaussians [140], etc. In this chapter, The Gaussian function is chosen to work as the RBF kernel, where the explicit form of Gaussian function is expressed as follows:

$$\varphi(\|\boldsymbol{x} - \boldsymbol{x_i}\|) = e^{-\left(\frac{\|x - x_i\|}{\epsilon}\right)^2} \tag{6.4}$$

where ϵ is a parameter to control the shape of the Gaussian function. The boundary $r(x)$ in the polar coordinate can be represented via the RBF functions as follows:

$$r(\theta) = \sum_{i=1}^{N} \alpha_i \varphi(\theta, \vartheta_i) \tag{6.5}$$

where $r(\theta)$ is the distance from arbitrary point in design domain to origin of polar coordinate, and θ is the angle in polar coordinates. ϑ_i is the control knot, which is uniformly distributed in the range of $[0,2\pi]$, and α_i is the expansion coefficient of the radial basis function of the ith knot. The above equation can be also written as following form:

$$r(\theta, \boldsymbol{\alpha}) = \boldsymbol{\phi}^{\boldsymbol{T}}(\theta, \boldsymbol{\vartheta})\boldsymbol{\alpha} \tag{6.6}$$

where

$$\boldsymbol{\phi}(\theta, \boldsymbol{\vartheta}) = [\varphi(\theta, \vartheta_1), \varphi(\theta, \vartheta_2), \cdots \varphi(\theta, \vartheta_N)]^T, \quad \boldsymbol{\alpha} = [\alpha_1, \alpha_2, \cdots \alpha_N]^{\boldsymbol{T}} \tag{6.7}$$

where N is the number of RBF knots. Thus, the density field enveloped by the RBF boundary can be explicitly represented as:

$$\rho(a, b, \boldsymbol{\alpha}) = \mathrm{H}\left(r(\theta, \boldsymbol{\alpha}) - \sqrt{(x-a)^2 + (y-b)^2}\right) \tag{6.8}$$

where $\mathrm{H}(\cdot)$ denotes the Heaviside function. ρ denotes the density value at point (x, y) and θ is the corresponding angle in polar coordinate, and (a, b) are the coordinates of the polar origin. For void region, the density field can be easily expressed as:

$$\bar{\rho} = 1 - \rho(a, b, \boldsymbol{\alpha}) \tag{6.9}$$

6.3 Merge of Multiple Void Geometry Components

In previous section, a projection from single void geometry component to density field is described in detail. For multiple void components, composite density is defined as follows:

$$\tilde{\rho}_j = 1 - \max \rho_{ij} \ (i = 1,2 \cdots n, j = 1,2 \cdots m) \tag{6.10}$$

where n denotes the number of void components and m represents total element number. Note that $\rho_{ij} = \rho_j(a_i, b_i, \boldsymbol{\alpha_i}) = H\left(r(\theta_j, \boldsymbol{\alpha_i}) - \sqrt{(x_j - a_i)^2 + (y_j - b_i)^2}\right)$, where $(a_i, b_i, \boldsymbol{\alpha_i})$ is the control parameters of $i\ th$ void component. (x_j, y_j, θ_j) denotes the coordinate and corresponding polar angle related to the center of $j\ th$ element. The p-norm formulation is applied to approximate the maximum function, which is defined as follows:

$$\tilde{\rho}_j = 1 - \left(\sum_{i=1}^{n} \rho_{ij}{}^p\right)^{1/p} \tag{6.11}$$

Note that the physical meaning of $\tilde{\rho}_j$ denotes the volume fraction of solid within the $j\ th$ element. The value of p-norm formulation will approximate the maximum of density ρ_{ij} once the value of p tends to infinity. For finite p value, p-norm function always exceeds the maximum density. The value of p is chosen as $p = 6$ in this chapter. If a larger p is chosen, the fluctuation of convergence history may be found. A small value of p always leads to a smooth and stable convergence. After numerical testing, the $p = 6$ is a reasonable choice. Note that the value of term $\left(\sum_{i=1}^{n} \rho_{ij}{}^p\right)^{1/p}$ may exceed unity. Thus, a Heaviside function is introduced to restrict composite density between 0 and 1, which is defined as follows:

$$\bar{\bar{\rho}}_j = \frac{(\tanh(3\tilde{\rho}_j)+1)}{2} \tag{6.12}$$

where $\bar{\bar{\rho}}_j$ is physical density, which is the actual density field in the finite element analysis (FEA). To prevent $\bar{\bar{\rho}}_j$ becoming very close to zero, which may result in stiffness matrix singular. A small value $\varepsilon_0 = 1 \times 10^{-5}$ is assigned to physical density of void region, and actual physical density becomes $\left(\bar{\bar{\rho}}_j + \varepsilon_0\right)$. The composite density concept is borrowed from Ref [188]. The merger of two void geometry components is presented in Figure 6.5.

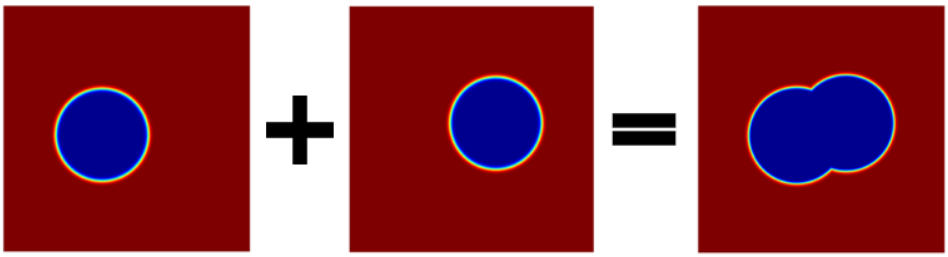

Figure 6.5 Merger of density field

6.4 Sensitivity Analysis based on Chain Rule

To employ gradient-based optimization algorithms to resolve topology optimization problems, sensitivities of design variables are required. Because the proposed method is in the framework of density-based method, the sensitivities of design variables can be obtained through chain rule as follows,

$$\frac{\boldsymbol{d}\mathbb{C}(\rho(\mathbf{X}))}{\boldsymbol{d}\mathbf{X}} = \frac{\boldsymbol{d}\mathbb{C}(\rho(\mathbf{X}))}{\boldsymbol{d}\rho}\frac{\boldsymbol{\partial}\rho}{\boldsymbol{\partial}\mathbf{X}} \tag{6.13}$$

where $\mathbb{C}$ denotes the objective or constraint functions. $\mathbf{X}$ is the design variable ($\mathbf{X} = [a, b, \boldsymbol{\alpha}]$)**,** and ρ is the physical density for FEM analysis. Therefore, the design sensitivities can be derived as follows,

$$\frac{\partial\overline{\rho}_j}{\partial\mathbf{X}} = \frac{\partial\overline{\rho}_j}{\partial\tilde{\rho}_j}\frac{\partial\tilde{\rho}_j}{\partial\rho_{ij}}\frac{\partial\rho_{ij}}{\partial\mathbf{X}} \tag{6.14}$$

The first two terms in above equations are given by,

$$\frac{\partial\overline{\rho}_j}{\partial\tilde{\rho}_j} = 3 - 3\,tanh\left(3\tilde{\rho}_j\right)^2 \tag{6.15}$$

$$\frac{\partial\tilde{\rho}_j}{\partial\rho_{ij}} = -\left(\sum_{i=1}^{n}{\rho_{ij}}^p\right)^{\frac{1}{p}-1}{\rho_{ij}}^{p-1} \tag{6.16}$$

For single void component, the sensitivity of $\rho(a,b,\boldsymbol{\alpha})$ with respect to design variables can be written as,

$$\frac{\partial \rho(a,b,\boldsymbol{\alpha})}{\partial a} = \mathrm{H}' \cdot \left(\frac{\partial r(\theta)}{\partial \theta}\frac{\partial \theta}{\partial a} + ((x-a)^2 + (y-b)^2)^{-\frac{1}{2}} \cdot (x-a) \right) \tag{6.17}$$

$$\frac{\partial \rho(a,b,\boldsymbol{\alpha})}{\partial b} = \mathrm{H}' \cdot \left(\frac{\partial r(\theta)}{\partial \theta}\frac{\partial \theta}{\partial b} + ((x-a)^2 + (y-b)^2)^{-\frac{1}{2}} \cdot (x-b) \right) \tag{6.18}$$

$$\frac{\partial \rho(a,b,\boldsymbol{\alpha})}{\partial \alpha_j} = \mathrm{H}' \cdot \varphi(\theta, \theta_j) \ \ (j = 1,2,\cdots N) \tag{6.19}$$

where H' denote the first order derivative of Heaviside function. The term $\frac{\partial r(\theta)}{\partial \theta}$ can be expressed as,

$$\frac{\partial r(\theta)}{\partial \theta} = [\frac{\partial \varphi(\theta,\theta_1)}{\partial \theta}, \frac{\partial \varphi(\theta,\theta_2)}{\partial \theta}, \cdots \frac{\partial \varphi(\theta,\theta_N)}{\partial \theta}] \cdot [\alpha_1, \alpha_2, \cdots \alpha_N]^T \tag{6.20}$$

where

$$\frac{\partial\, \varphi(\theta,\theta_i)}{\partial \theta} = -2\frac{\theta-\theta_i}{\epsilon^2} e^{-\left(\frac{\theta-\theta_i}{\epsilon}\right)^2} \ \ (i = 1,2\cdots N) \tag{6.21}$$

6.5 Nonlinear Finite Element Analysis for Buckling-induced Mechanism

6.5.1 Nonlinear Finite Element Analysis based on Total Lagrangian Formulation

As shown in Figure 6.6, a body is described by continuously distributed points *P* in domain B called material points. The body deforms under external force, and the new configuration of deformed body is denoted as:

$$\boldsymbol{x} = \varphi(\boldsymbol{X}, t) \tag{6.22}$$

where φ denotes the one-to-one mapping function. x is the location of a material point P at time t, and $\boldsymbol{X}$ represents the location of material point P in the reference configuration. It is worth to mention that the present motion is described with respect to the initial material coordinates, which can be also referred to as the Lagrangian description of motion.

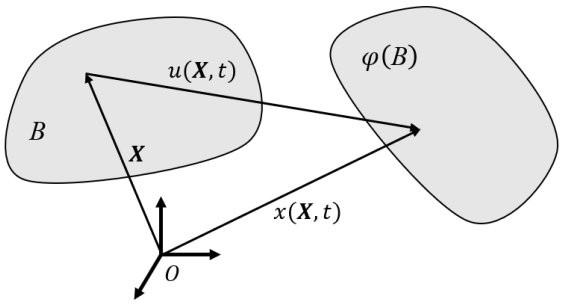

Figure 6.6 Deformation of a continuum body from its undeformed configuration to a deformed configuration

To describe the deformation, a tensor **F** is introduced to relate the initial and current configuration, which is defined as follows:

$$d\boldsymbol{x} = \mathbf{F}d\mathbf{X} \tag{6.23}$$

F denotes the deformation gradient. The above strain tensor is referred to the initial configuration. Spatial equilibrium equation for a deformable body is written as:

$$div\ \boldsymbol{\sigma} + \boldsymbol{f} = \mathbf{0} \tag{6.24}$$

where $\boldsymbol{\sigma}$ is Cauchy stress tensor and $\boldsymbol{f}$ is body force. Materials for which the constitutive behavior is only a function of current state of deformation are known as elastic. Furthermore, the material is termed hyperelastic when the work done by the stresses during deformation is only dependent on the initial and final configuration state. Note that the hyperelastic material is path independent. Elastic potential Ψ per unit undeformed volume is defined as the work done by stresses during deformation. The Mooney-Rivlin model [77], which is one of the most popular hyperelastic material model, is adopted here to describe the strain energy function. The strain energy expression

of Mooney-Rivlin model, which include the effect of the invariants I_1 , I_2, and I_3 can be written as follows:

$$\Psi = A_{10}\left(I_1 I_3^{-1/3} - 3\right) + A_{01}\left(I_2 I_3^{-2/3} - 3\right) + \frac{K}{2}\left(I_3^{1/2} - 1\right)^2 \tag{6.25}$$

where A_{10} and A_{01} are two nonzero parameters, which need to be determined through material testing. K is the bulk modulus. Most hyperelastic materials such as rubber have a large bulk modulus, which means a small volume change leads to a large hydrostatic pressure.

6.5.2 The Path-following Algorithm for Nonlinear Buckling Structures

Buckling-induced structures experience complex deformation behavior beyond the limit points. To accurately capture the highly nonlinearity of buckling-induced mechanism, the arc-length method is proposed, which is an incremental-iterative numerical technique based on FEM. This technique is originally pioneered by Wempner [189], and Crisfield [81]. For arc-length method, a constraint equation called the arc-length equation is added to the original nonlinear equations [81]. The augmented nonlinear systems are obtained, which resolve the incremental load factor along with the incremental displacements. The governing equations of nonlinear elasticity problem can be formulated as follows:

$$\mathbf{R}(\boldsymbol{u}, \lambda) = \mathbf{F}^{\text{int}}(\boldsymbol{u}) - \lambda \mathbf{F}^{\text{ext}} = \mathbf{0} \tag{6.26}$$

where $\boldsymbol{u}$ is the nodal displacement vector, and λ is the load factor. $\mathbf{F}^{\text{int}}$ denotes the internal force vector, $\mathbf{F}^{\text{ext}}$ the external force vector, and $\mathbf{R}$ is the residual vector. The solutions of the above equations are obtained through an incremental approach with iterative technique.

6.5.3 Fictitious Domain Approach

For geometrically nonlinear topology optimization, low density area (low stiffness) may become excessively distorted under large deformation. This phenomenon is dominated for standard density-based method, which inevitably leads to numerical instability in FEA. To effectively alleviate local excessive distortion during optimization, a fictitious domain approach is proposed by Wang et al [58]. The basic idea of this method is that high density element is modelled with geometrically nonlinear element, while linear element is assigned to low density area to avoid excessive element distortion. To conceptualize this idea, an energy interpolation scheme is proposed by Wang et al [58] to describe material behavior as follows:

$$\Psi(\boldsymbol{u}_e) = [\Psi(\gamma_e \boldsymbol{u}_e) - \Psi_L(\gamma_e \boldsymbol{u}_e) + \Psi_L(\boldsymbol{u}_e)]E_e \tag{6.27}$$

where E_e is elastic modulus of solid element, and $\boldsymbol{u}_e$ is the elemental nodal displacement vector. Ψ denote the stored strain energy of nonlinear element, and Ψ_L denotes the stored energy of linear element. In the equation above, the interpolation factor γ_e equals to unity for solid elements ($\rho = 1$), while $\gamma_e = 0$ corresponds to void element. The interpolation factor should satisfy that the stored energy corresponds to linear energy when $\gamma_e = 0$, while energy is simply depicted by nonlinear energy if $\gamma_e = 1$. To distinguish the high-density elements and low-density elements with a smooth continuous approach, a Heaviside function is introduced to ensure a smooth and differentiable transition. The elemental strain energy of intermediate density region is named as transition elements. For the TO method proposed in this chapter, since the intermediate density region is only near the boundary of topology, the transition elements only locate at boundary area as shown in Figure 6.7. In fact, if there exist large number of intermediate density regions in optimization, the excessive element distortion may still happen under large deformation using

fictitious domain method. However, this issue can be successfully circumvented by our proposed method. Threshold parameter γ_e can be modeled as follows [58]:

$$\gamma_e(x) = \frac{\tanh(\beta_1 x_0)+\tanh(\beta_1(x-x_0)}{\tanh(\beta_1 x_0)+\tanh(\beta_1(1-x_0))} \tag{6.28}$$

where x_0 is a threshold. In most cases, $x_0 = 0.01$ and $\beta_1 = 500$ are chosen in optimization progress.

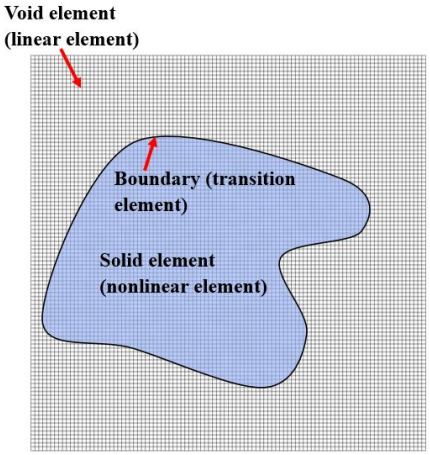

Figure 6.7 Fictitious domain method

6.6 Topology Optimization Formulation

6.6.1 Optimization Problem Formulation

To achieve a buckling-induced design, an optimization algorithm is implemented here to tailor the nonlinear response of initial design to achieve snap-through behavior. In general, an initial design, like a cube, does not show buckling phenomenon under finite deformation. How to modify the initial design to present snap-through behavior is a key objective in this chapter. A

feasible way is that controlling the two points on force-displacement curve to push the right equilibrium point downward so that the force factor of right point is less than that of left equilibrium point. This point is demonstrated in detail as shown in Figure 6.8. To ensure that the optimized structure is stiff enough, a constraint at left point (point 1) is applied, which plays key role for buckling-induced design. A formal statement of the optimization problem can be formulated as follows:

$$\begin{gathered} min\,\lambda_2 \\ subject\ to\colon\ \lambda_1 \geq \lambda_0 \quad (\lambda_0 > 0) \\ \frac{V(\rho)}{|\Omega|} - v_f^* \leq 0 \end{gathered} \tag{6.29}$$

where $|\Omega|$ is design domain area and v_f^* is prescribed volume fraction. λ_0 is a force lower limit at point 1. $\lambda_1$and λ_2 are force factors at point 1 and 2, respectively. $V(\rho)$ denotes volume of material layout. If the algorithm manages to find a solution such that $\lambda_2 < \lambda_1$, then the corresponding design will exhibit snap-through behavior. Note that the choice of λ_0 , u_0 and u_1 is dependent on numerical experience.

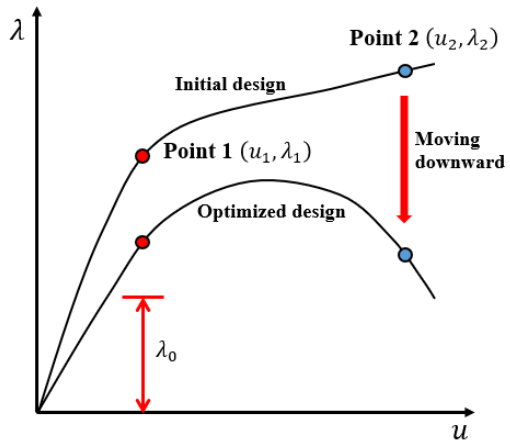

Figure 6.8 Sample force-displacement curves for initial design and optimized design

6.6.2 Sensitivity Analysis

To obtain an optimized design, gradient-based methods are required for formulating nonlinear programming problem. In this chapter, the gradients of objective and constraint functions with respect to design variables are evaluated using adjoint method [190] through analytical derivation. Since displacement u is prescribed, Lagrange multipliers $\boldsymbol{\mu_1}$and μ_2 are introduced to obtain the derivative of force factor λ with respect to physical density ρ. The nonlinear equilibrium equations are expressed in residual form as follows:

$$\boldsymbol{R} = \boldsymbol{F^{int}} - \lambda \cdot \boldsymbol{F^{ext}} = \boldsymbol{0} \tag{6.30}$$

The basic form of force $\boldsymbol{F^{ext}}$ is as follows,

$$\boldsymbol{F^{ext}} = [\boldsymbol{0}, \cdots \boldsymbol{0}, F_c, \boldsymbol{0}, \cdots \boldsymbol{0}] \tag{6.31}$$

where F_c is a constant force at a specific loading DOF. Without loss of generality, the augmented objective function is written as,

$$\chi = \lambda + \boldsymbol{\mu_1^T}(\boldsymbol{F^{int}} - \lambda \cdot \boldsymbol{F^{ext}}) + \mu_2(\boldsymbol{F^{ext^T}U} - u^*) \tag{6.32}$$

where $\boldsymbol{\mu_1^T}$ and μ_2 are constants that need to be determined through adjoint equations, and u^* is the prescribed value. $\boldsymbol{F^{ext}}$ is constant force vector. λ is the force factor of arbitrary point on the equilibrium force-displacement curve. Thus, the derivative for χ with respect to density ρ is given by:

$$\frac{\partial \chi}{\partial \rho} = \left(1 - \boldsymbol{\mu_1^T F^{ext}}\right)\frac{\partial \lambda}{\partial \rho} + \boldsymbol{\mu_1^T}\frac{\partial \boldsymbol{F^{int}}}{\partial \rho} + (\boldsymbol{\mu_1^T K} + \mu_2 \boldsymbol{F^{ext^T}})\frac{\partial \boldsymbol{U}}{\partial \rho} \tag{6.33}$$

where $\boldsymbol{K}$ is tangent stiffness. Choosing $\boldsymbol{u_1}$ and μ_2 to eliminate terms $\frac{\partial \lambda}{\partial \rho}$and $\frac{\partial \boldsymbol{U}}{\partial \rho}$, and adjoint equations can be reformulated as follows:

$$\boldsymbol{\mu_1^T F^{ext}} = 1 \tag{6.34}$$

$$\boldsymbol{K\mu_1} = -\mu_2 \boldsymbol{F^{ext}} \tag{6.35}$$

Thus,

$$\boldsymbol{\mu_1} = \frac{1}{\boldsymbol{F^{ext^T} K^{-1} F^{ext}}} \boldsymbol{K^{-1} F^{ext}} \tag{6.36}$$

$$\mu_2 = -\frac{1}{\boldsymbol{F^{ext^T} K^{-1} F^{ext}}} \tag{6.37}$$

Therefore, the sensitivity of force factor with respect to physical density is expressed as:

$$\frac{\partial \lambda}{\partial \rho} = \left(\frac{1}{\boldsymbol{F^{ext^T} K^{-1} F^{ext}}} \boldsymbol{K^{-1} F^{ext}}\right)^T \cdot \frac{\partial \boldsymbol{F^{int}}}{\partial \rho} \tag{6.38}$$

where the term $\frac{\partial \boldsymbol{F^{int}}}{\partial \rho}$ is easily obtained, and the detailed description can be found in Ref. [57]. It is worth to mention that sensitivity of the objective with respect to parameters $(a, b, \boldsymbol{\alpha})$ can be derived through chain rule. Note that above sensitivity analysis is applicable for arbitrary point on the equilibrium force-displacement curve. Therefore, the sensitivity of force factor at point 1 and point 2 with respect to density ρ can be expressed as,

$$\frac{\partial \lambda_1}{\partial \rho} = \left(\frac{1}{\boldsymbol{F^{ext^T} K_1^{-1} F^{ext}}} \boldsymbol{K_1^{-1} F^{ext}}\right)^T \cdot \frac{\partial \boldsymbol{F_1^{int}}}{\partial \rho} \tag{6.39}$$

$$\frac{\partial \lambda_2}{\partial \rho} = \left(\frac{1}{\boldsymbol{F^{ext^T} K_2^{-1} F^{ext}}} \boldsymbol{K_2^{-1} F^{ext}}\right)^T \cdot \frac{\partial \boldsymbol{F_2^{int}}}{\partial \rho} \tag{6.40}$$

where $\boldsymbol{K_1}$and $\boldsymbol{K_2}$ are tangent stiffness matrix at point 1 and point 2, and $\boldsymbol{F_1^{int}}$ and $\boldsymbol{F_2^{int}}$ are the internal force vectors at point 1 and point 2.

6.6.3 Optimization Flow

The detailed implementation of the proposed method for buckling-induced design is described in the flowchart (see Figure 2.1). At the beginning, the parameters are initialized, where several internal holes are generated in design domain like the level set method [29]. The physical

density field can be computed through the proposed method, where the boundary is explicitly described by RBF functions controlled by their knots. Nonlinear FEA is implemented to trace the force-displacement response, where MGDCM algorithm and fictitious domain method are applied. Note that for a prescribed displacement u^*, the Newton-Raphson method is applied to determine the exact force factor λ^* at u^*. (The initial point of Newton-Raphson method is obtained through MGDCM algorithm). Once the solutions are obtained, the objective and constraint functions are computed, and sensitivity analysis $\frac{\partial \lambda_1}{\partial \rho}$ and $\frac{\partial \lambda_2}{\partial \rho}$ are conducted as described in section 6.6.2. Note that the chain rule should be used to compute the sensitivity with respect to design variables. The MMA optimizer is implemented to update the design variables, where a small moving limit is chosen to avoid fluctuation of optimization. Note that the material behavior is described by the Mooney-Rivlin model [191] in our optimization model.

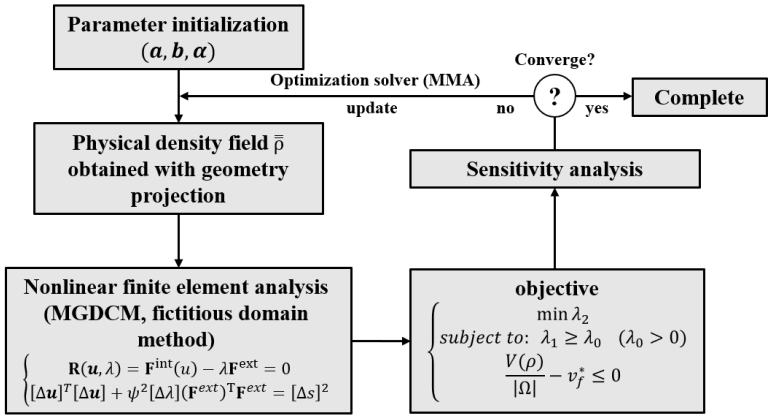

Figure 6.9 Optimization flow

6.7 Numerical Examples

6.7.1 Numerical Example 1

In this section, several numerical examples presented to demonstrate the effectiveness of the proposed projection-based boundary evolving algorithm. Before we apply the proposed method to design the buckling-induced mechanism, a linear-elastic compliance minimization problem is presented first to demonstrate the effectiveness of the proposed algorithm. In this example, an isotropic elastic material with elastic modulus $E = 1$ and Poisson's ratio of $v = 0.3$. The boundary and loading are demonstrated in Figure 6.10. The loading $F = 1$ is applied at the midpoint of right edge. The objective is minimizing compliance with volume fraction constraint ($v < 0.3$), which is standard benchmark for topology optimization [34]. The detailed description of objective function and sensitivity analysis can be found in Ref. [34]. Unless specified, the moving limit of MMA algorithm is chosen as $m = 0.01$, and the kernel width of RBF function is $\varepsilon = 0.1$. The initial design and optimized design are demonstrated in Fig. 11. As shown in Fig. 11(a), the initial design contains 4 voids, and the geometry of each void is represented by an RBF-based curve with 73 uniformly distributed knots. The evolving history of density field is plotted in Figure 6.12. It is worth to mention that the intermediate density is only near the boundary of topology as shown in Figure 6.12. The convergence history is demonstrated in Figure 6.13, where the optimization progress converges after 40 iterations.

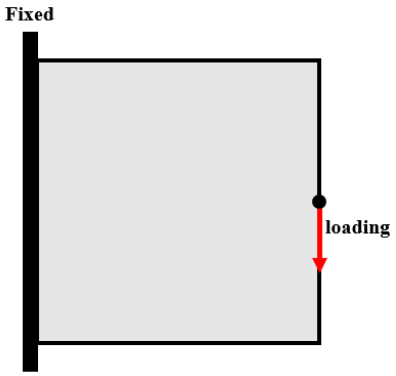

Figure 6.10 Problem definition

(a) Initial design (b) Optimized design

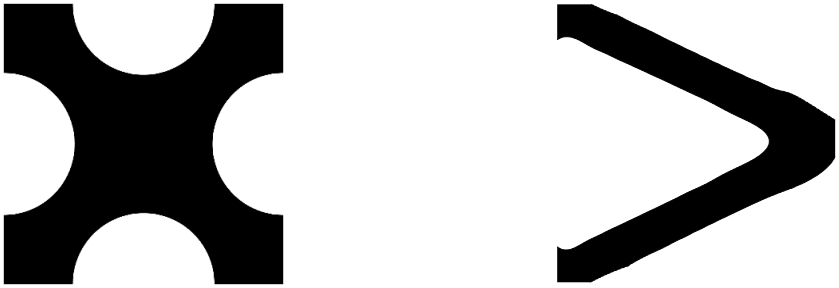

Figure 6.11 Square beam example (a) Initial design (b) Optimized design

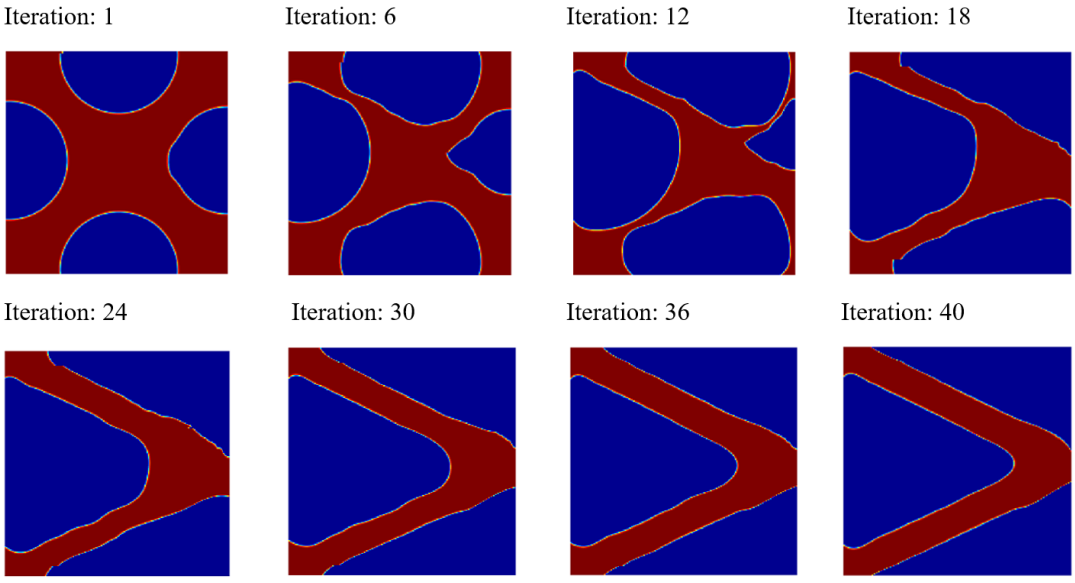

Figure 6.12 Evolving history of density field

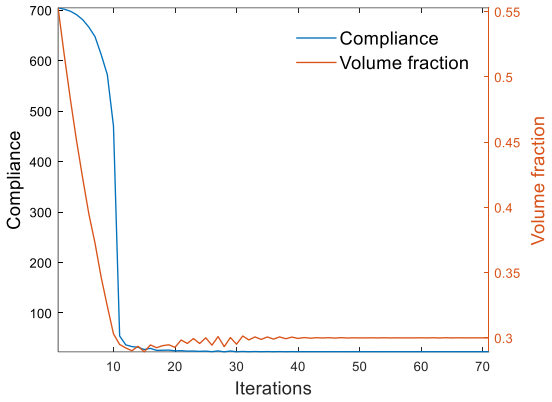

Figure 6.13 Convergence history

6.7.2 Numerical Example 2

This example focuses on the design of buckling-induced mechanism using the proposed optimization method. The rectangle domain is presented in Figure 6.14, where 200×100 plane strain elements are generated with element length 0.5 for FEA. The lower edge is constrained along the loading direction; left and right corners are constrained in horizontal direction. The downward displacement loading is applied at the mid-point of the upper edge. The material parameters of Mooney-Rivlin model is chosen as: $A_{10} = 34, A_{01} = 5.8$ and $K = 2000$. Unless specified, the plane strain assumption is applied for nonlinear FEA. As shown in Figure 6.15(a), the initial design contains 7 voids, and the geometry of each void is represented by an RBF-based curve with 73 uniformly distributed knots. The parameters of optimization problem are selected as: $u_1 = 5, u_2 = 10$ and $\lambda_0 = 20$. The constant force is chosen as $F^c = 4$, and the volume fraction constraint is $v_f^* = 0.3$. Note that the total number of design variables of each void is 75, where two extra degrees of freedom are coordinates of origin. The optimized design is plotted in Figure 6.15(b). Note that

the hinge-like components appear in the final optimized design. The optimization progress converges after 45 iterations and the optimization history is shown in Figure 6.16. The deformation of the optimized designs at different loading steps is demonstrated in Figure 6.17. Obviously, the beam with two hinges will rotate approximate 90 degrees when the loading displacement $u = 15.8$ as shown in Figure 6.17. The force-displacement curve is plotted in Figure 6.18. Note that there is no buckling occurs in the initial design, while the negative stiffness behavior is found in the optimized design after optimization.

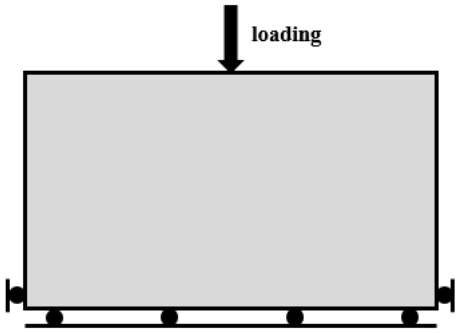

Figure 6.14 Problem definition

(a) Initial design (b) Optimized design

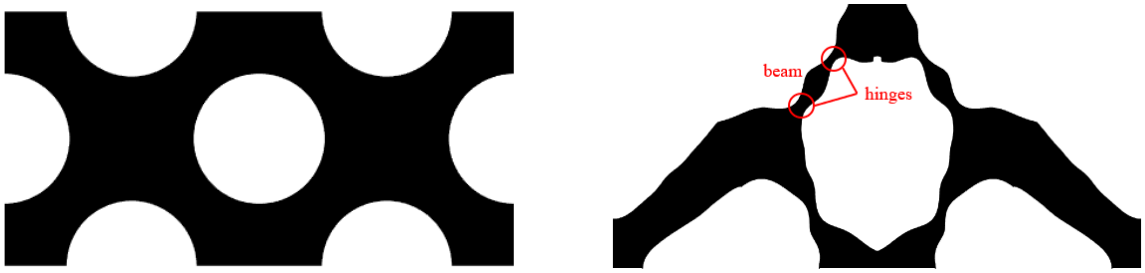

Figure 6.15 (a) Initial design (b) Optimized design

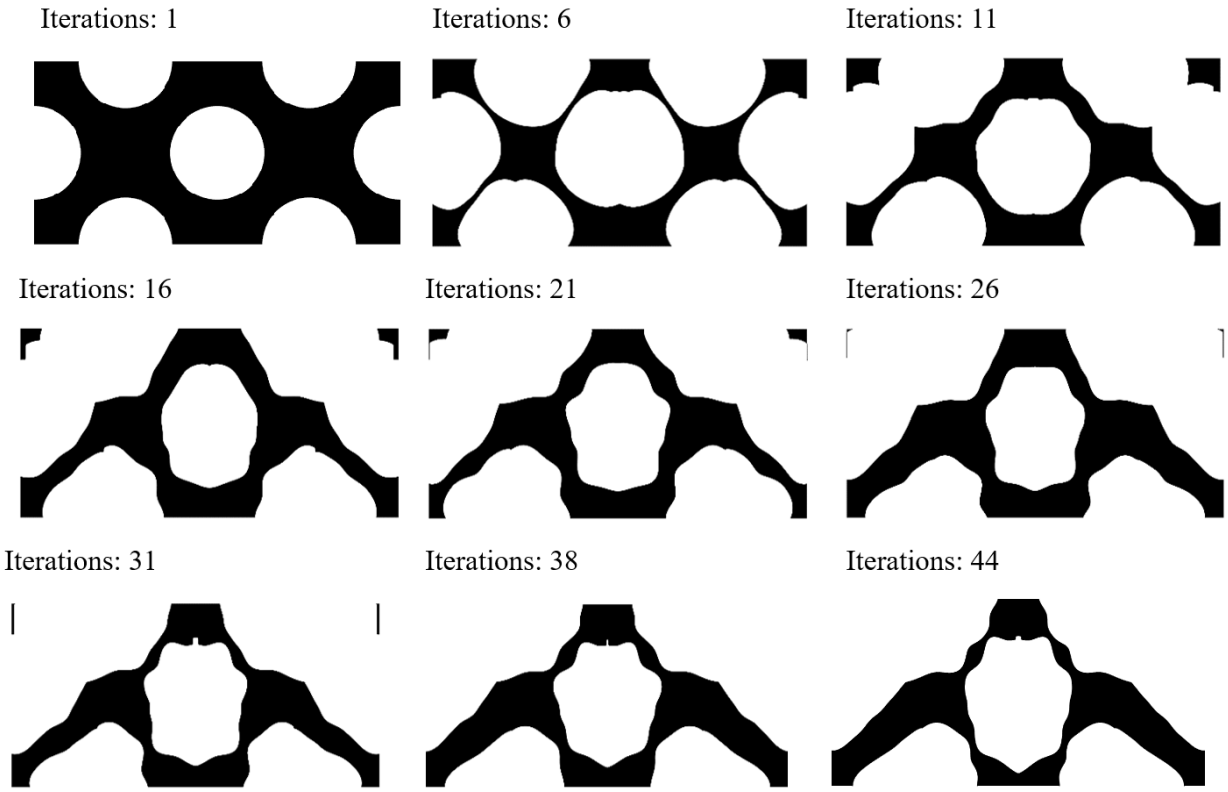

Figure 6.16 Evolving history of optimized design

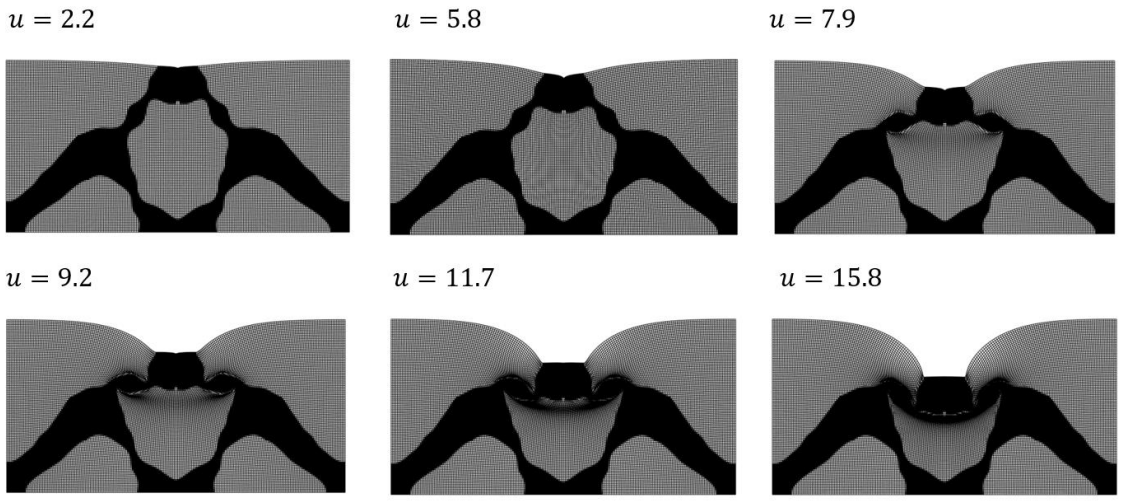

Figure 6.17 Deformation at different loading steps

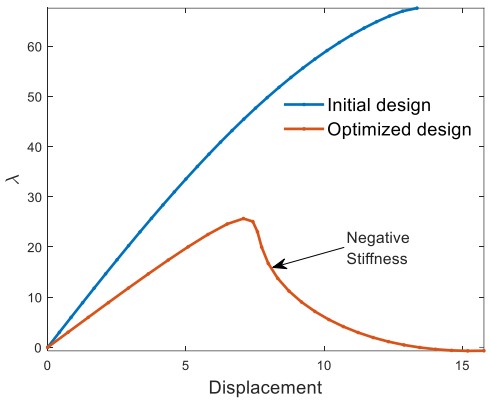

Figure 6.18 Force-displacement response

To make a comparison, different constraint parameter values are chosen to check their effect on the optimized designs. Other optimization parameters are the same as in the previous example. In this case, the constraint parameters are chosen as $u_1 = 5, u_2 = 15$ and $\lambda_0 = 15$. The initial design is shown in Figure 6.19(a), and the optimized design is plotted in Figure 6.19(b). The force-displacement response is plotted in Figure 6.21, where the negative stiffness phenomenon appears after $u = 12$. The buckling mode is different compared with the previous case. Note that the buckling happens when the hinge-like component rotates as shown in Figure 6.20. In the present example, the limit point locates at the $u \approx 12$ with force factor $\lambda \approx 28$. This example shows that the buckling design is quite sensitive to design parameter value change.

(a) Initial design (b) Optimized design

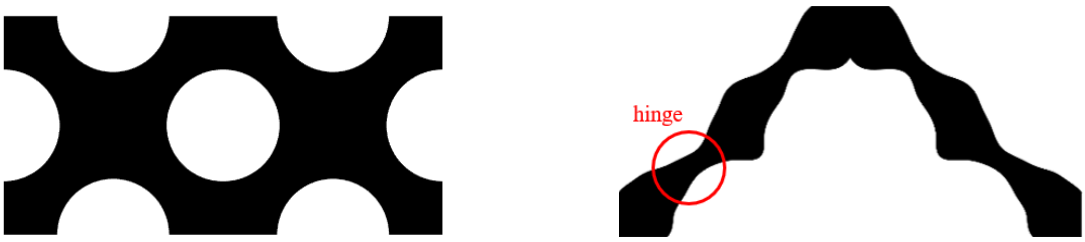

Figure 6.19 (a) Initial design (b) Optimized design

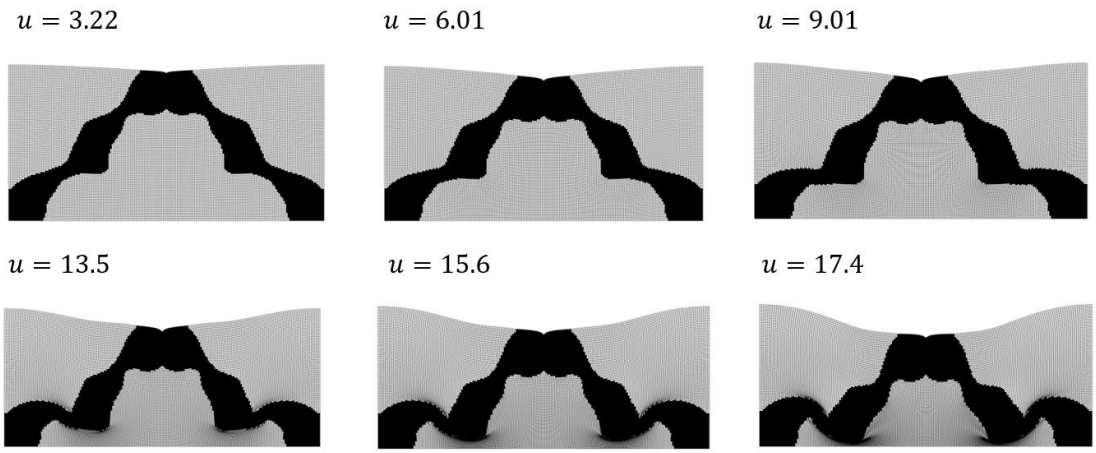

Figure 6.20 Deformation at different loading steps

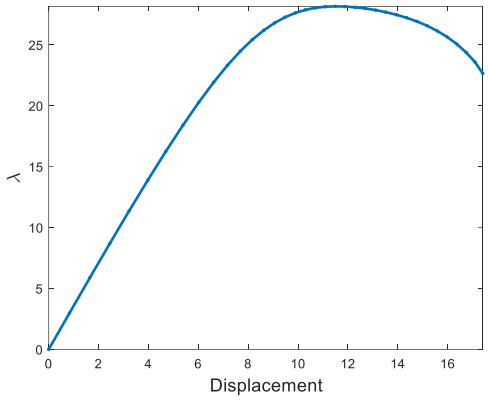

Figure 6.21 Force-displacement response

6.8 Conclusion

In this chapter, a new computational scheme for topology optimization is proposed, where the boundary of voids is described based on RBF interpolation method in an explicit way, and p-norm function is implemented to merge the multiple voids. The proposed method is applied to design snap-through mechanism undergoing large deformation. The main advantages of the

proposed approach can be summarized as: (1) The proposed computational scheme is in the framework of density-based method, where the sensitivity analysis for standard density-based method is directly utilized based on the chain rule. (2) The intermediate density only locates at the boundary region, which shares the advantages of level set based methods. The proposed method is better for circumventing the excessive mesh distortion issue in low density area. (3) Since the structural geometry is explicitly described, it is easy to incorporate some manufacturing constraints, e.g., feature size, curvature of the structural boundary, etc. This point will be examined in the future. (4) Merging multiple voids based on p-norm functions is straightforward and simple for numerical implementation. As demonstrated in numerical examples, the proposed method is capable of optimizing the initial design to generate buckling-induced mechanism with appropriate moving limit of MMA algorithm, and no divergence occurs during optimization.

7.0 A Novel Mathematical Formulation for Projection-based Topology Optimization Method Considering Multi-Axis Machining Constraint

7.1 Current Progress of Topology Optimization for Multi-axis Machining

Topology optimization has become an important tool to determine the optimal shape for maximum performance subject to given design constraints. These performance objective functions and design constraints affect the applicability of the design and typically include the mass, compliance, stress, or displacement due to loading conditions. New methods have since been implemented such as the Solid Isotropic Material with Penalization (SIMP) method [192] and the level-set method [29], both of which can be found in commercial software. For the SIMP method, each element is assigned a density variable to control the material distribution and remove material from gradient-based optimization. For the level-set method, the boundary of the shape geometry is the zero level-set of an implicit function. The parameters defining the function are optimized to produce the optimal shape.

These methods can produce complex shapes not typically considered by a human engineer or designer. Consequently, it can be difficult to manufacture these designs as well and can require extensive post-processing [193]. To control the geometric complexity, other new methods have been developed such as moving morphable components (MMC) [11, 13], moving morphable voids (MMV) [194], and geometry projection [195]. MMC and MMV use controlled geometries to add or remove material from the design domain and determine the optimal shape. Geometry projection methods [19, 188] use geometries to describe the density distribution on a background mesh.

Additionally, integrating the topology optimization process with CAD has been addressed as well to further reduce post-processing [196].

This chapter mainly focuses on the multi-axis machining constraints, which is a widely used techniques in subtractive manufacturing for metal component production. For multi-axis machining, the relative position and orientation of cutting tools and workpiece can be manipulated in 4 or 5 degrees of freedom. The unnecessary material is removed by machining tool until the desired shape achieves. Compared with 2.5D milling, the multi-axis machining allows more design freedom. Besides machining, metal additive manufacturing is also a well-known technique to print free-form design with high design freedom, while the material strength and fatigue properties of parts made of AM still have large gap compared to metal machining. For high-strength aerospace or naval structures, multi-axis machining is an ideal option for manufacturing parts. Thus, topology optimization approaches considering machining constraint is a necessary and valuable research to achieve a trade-off between the available manufacturing technologies. In recent years, a few effective approaches for multi-axis machining-based topology optimization are proposed. For 2.5D milling, Liu et al [197] proposes an explicit feature-based level-set method, where the feature fitting algorithm is incorporated into the boundary evolvement process. Furthermore, Liu and Albert [198] proposed a novel CAD-based topology optimization system for milling constraint, where feature and dynamic modeling history is incorporated into the optimization process. For multi-axis machining, Amir et al [199] presented a topology optimization framework using convolutions in configuration space to enable manufactured design using multi-axis machining, where an inaccessibility measure field of design domain is introduced to identify non-manufacturable features. Nigel et al [200] proposed a level-set-based topology optimization method for multi-axis machining, where the advection velocity at every iteration is modified to

ensure the manufacturability conditions. This level-set-based method simulates the subtractive process by cutting materials accessible to the machine in every iteration until optimization converges. Matthijs et al [201] proposed a density-based approach incorporating multi-axis restrictions, where a filter technique based on KS aggregation function [202] is introduced to transform an input design field into a manufacturable geometry. Besides the multi-axis machining, several other related topology optimization studies regarding casting constraints can also be found in Ref [203-206].

The aim of this chapter is to propose a novel density-based approach to optimize parts for multi-axis machining restrictions, where a concise aggregation-free density projection formulation is demonstrated. The subtractive manufacturing constraints can be satisfied after density projection.

7.2 Mathematical Formulation for Multi-axis Machining

7.2.1 Machining Restriction

The milling head is generally described by a cylinder capped with a hemisphere oriented in the milling direction. The end of the head cylinder is assumed to extend infinitely far away from the cutting surface. For 3 axis machining, the workpiece is still while the cutting tool moves along the 3 mutually perpendicular axes to mill the part, which is a most widely used technique to create mechanical parts. While for 5-axis machining process, the milling tool can be oriented to approach the surface from an arbitrary direction. The machinable part is determined by whether all its surface points are accessible by tool bit without any intersection with the interior of the part. As described

by Ref [201], machinability means that the density field must be monotonically increasing in the insertion direction without any internal holes. To enforce the milling constraints, a Heaviside function-based projection method is proposed here to construct the monotonically increasing density field in the milling direction.

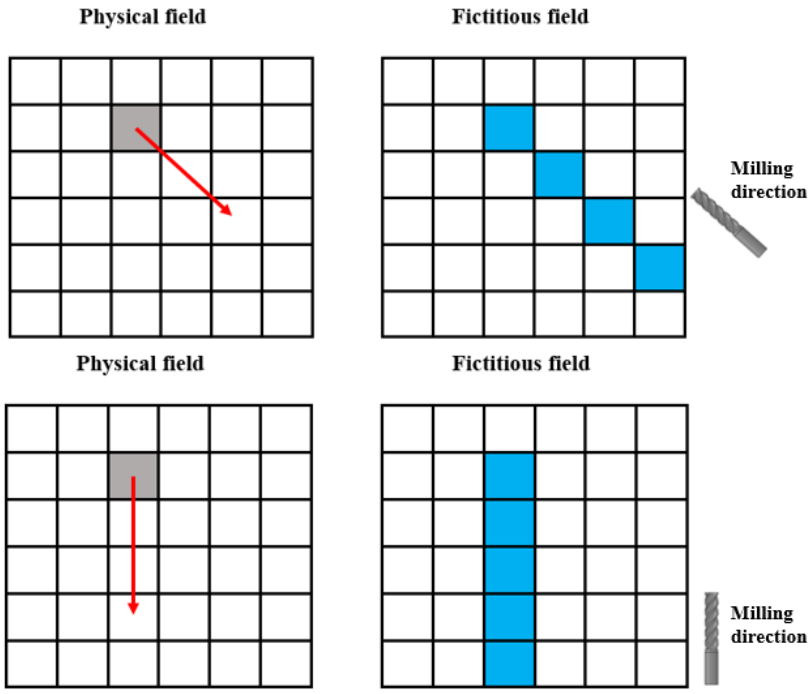

Figure 7.1 Density Mapping from fictitious field to physical field

This subsection outlines the conceptual idea for the proposed mathematical formulation considering multi-axis machining constraint. The physical field is used for FEM analysis. The physical density field is computed through the cumulative summation of fictitious density along reverse milling direction as shown in Figure 7.1. The Heaviside function is introduced here to map the fictitious density to physical density as follows,

$$\rho_p = \mathrm{H}_2\left(\sum_{j\in\mathcal{M}} \mathrm{H}_1(\rho_f^{(j)})\right) \tag{7.1}$$

where notation $\sum(\cdot)$ means cumulative summation of fictitious element density along reverse milling direction. $\mathcal{M}$ is the set of elements along reverse milling direction. The element set $\mathcal{M}$ can be determined based on following flowchart,

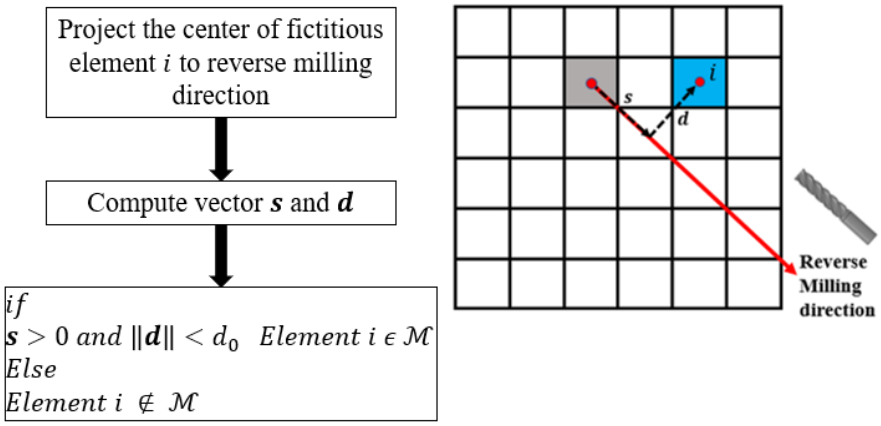

Figure 7.2 Flowchart of computing set $\mathcal{M}$

As shown in flowchart, d_0 is a threshold, and the operation $\|\cdot\|$ denotes the Euclidean norm. As demonstrated in Figure 7.2, the grey element in physical field ρ_p is computed through summation of blue element ($\mathcal{M}$) in fictitious density field ρ_f. $\mathrm{H}_1(\cdot)$ and $\mathrm{H}_2(\cdot)$ denote the Heaviside functions defined as:

$$\begin{cases} \mathrm{H}_1(x) = \frac{\tanh(10x-3)+1}{2} \\ \mathrm{H}_2(x) = \frac{\tanh(6x-3)+1}{2} \end{cases} \tag{7.2}$$

The shape of Heaviside functions is plotted as follows,

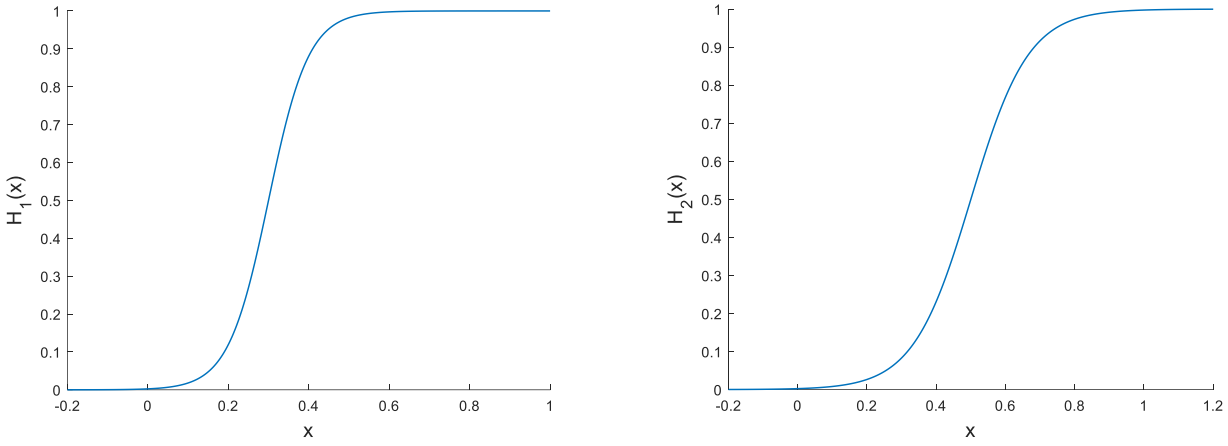

Figure 7.3 Heaviside functions

To effectively control the minimum size of void area, we introduce the void field to work as design variables. The relationship between void field and fictitious domain can be defined as follows,

$$\rho_f = \frac{1}{\sum_{i\in N_f} d_{fi}} \sum_{i\in N_f} d_{fi}\left(1-\rho_v^{(i)}\right) \tag{7.3}$$

where d_{fi} is weight factor for filter defined as:

$$d_{fi} = max(0, r_{min} - \Delta(f,i)) \tag{7.4}$$

r_{min} is the filter radius. $\Delta(f,i)$ denotes the distance between the center of element i and f. N_f is the set of elements i for which the distance $\Delta(f,i)$ less than r_{min}. More details regarding filtering techniques can be found in Ref [34]. Therefore, the physical density ρ_p can be explicitly expressed as,

$$\rho_p = \mathrm{H}_2\left(\sum_{f\in\mathcal{M}} \mathrm{H}_1\left(\frac{1}{\sum_{i\in N_f} d_{fi}} \sum_{i\in N_f} d_{fi}\left(1-\rho_v^{(i)}\right)\right)\right) \tag{7.5}$$

For multiple milling directions $(i = 1, \cdots, n)$, the composite physical density field can be simply expressed as,

$$\overline{\rho_p} = \prod_{i=1}^{n}\left(\rho_p{}^{(i)}\right) \tag{7.6}$$

where $\rho_p{}^{(i)}$ denote the physical density computed from the i milling direction. A typical projection from void density field to physical density field is demonstrated in Figure 7.4.

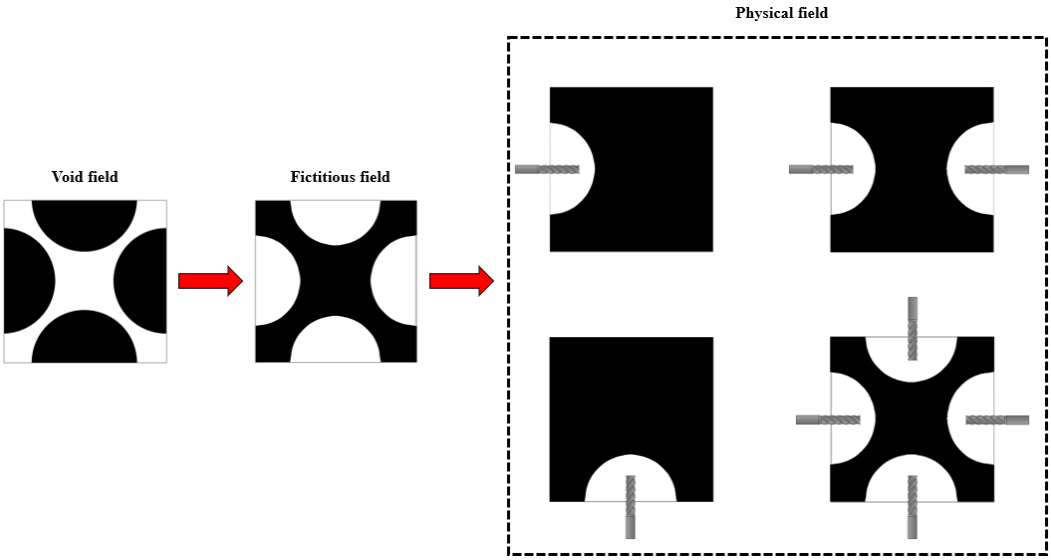

Figure 7.4 Projection from the void field to physical field

7.2.2 Sensitivity Analysis

Given a response $f(\rho_v)$, the sensitivity with respect to the design variables ρ_v can be obtained through the chain rule as follows,

$$\frac{\partial f}{\partial \rho_v^{(l)}} = \frac{\partial f}{\partial \overline{\rho_p}} \frac{\partial \overline{\rho_p}}{\partial \rho_v{}^{(l)}} = \frac{\partial f}{\partial \overline{\rho_p}} \sum_{i=1}^{n} \left(\frac{\partial \rho_p{}^{(i)}}{\partial \rho_v^{(l)}} \prod_{j=1; j\neq i}^{n} \left(\rho_p{}^{(j)} \right) \right) \tag{7.7}$$

where Einstein summation applies to all repeated subscripts. n is the number of machining direction. The explicit form of the term $\frac{\partial \rho_p{}^{(i)}}{\partial \rho_v^{(l)}}$ can be expressed as,

$$\frac{\partial \rho_p{}^{(i)}}{\partial \rho_v^{(l)}} = \mathrm{H}_2{}' \cdot \left(\sum_{f \in \mathcal{M}^{(i)}} \frac{\partial \mathrm{H}_1 \left(\frac{1}{\sum_{i \in N_f} d_{fi}} \sum_{i \in N_f} d_{fi} \left(1 - \rho_v^{(i)} \right) \right)}{\partial \rho_v^{(l)}} \right) \tag{7.8}$$

where

$$\frac{\partial \mathrm{H}_1\left(\frac{1}{\sum_{i\in N_f} d_{fi}}\sum_{i\in N_f} d_{fi}\left(1-\rho_v^{(i)}\right)\right)}{\partial \rho_v^{(l)}} = \mathrm{H}_1{}' \cdot \frac{\partial\left(\frac{1}{\sum_{i\in N_f} d_{fi}}\sum_{i\in N_f} d_{fi}\left(1-\rho_v^{(i)}\right)\right)}{\partial \rho_v^{(l)}} \tag{7.9}$$

where $\mathrm{H}_1{}'$and $\mathrm{H}_2{}'$ denote the first derivative of Heaviside function. The detailed form of $\frac{\partial f}{\partial \rho_v^{(l)}}$ can be easily derived, which is omitted here.

7.3 Numerical Examples

7.3.1 Machining-based Optimization for a 2D Cantilever Beam

The first 2D numerical example for machining-based topology optimization is demonstrated in Figure 7.5. The design domain is uniformed meshed by 100×100 quad elements with unit length. The loading $F = 1$ is applied on the right-bottom corner, and left side is fully fixed. The volume fraction constraint $\bar{V}$ is chosen as 0.2. The elastic constants are chosen as follows: Elastic modulus $E = 1$ and Poisson's ratio $\mu = 0.3$. The filter radius for design variable is chosen as r_{min} = 4. The initial void field (design variable) is plotted in Figure 7.7. To make a comparison, different milling direction constraints are applied to produce optimized design. The reference solution without any manufacturing constraints is demonstrated in Figure 7.6. Obviously, the reference solution cannot be manufactured if machining operations are limited in the x, y-plane. The initial and optimized designs for single milling orientation are demonstrated in Figure 7.7, and convergence history is plotted in Figure 7.8. Compared with the reference solution, the optimized part for unidirectional milling restriction shows strong limitation of design freedom,

which also has great impact on structural compliance. Note that the designs with single milling orientation constraint are considerably more compliant with respect to reference design. For multiple tool orientations, the optimized designs are shown in Figure 7.9, and convergence history is plotted in Figure 7.10. The structural performance with multiple directions is better than the single orientation, while the compliance value still higher than the reference design. This simple 2D numerical example proves the effectiveness of proposed method to force the optimization process towards a different solution considering multi-axis machining constraints.

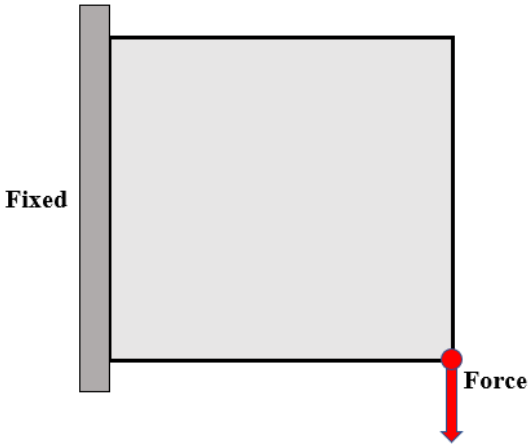

Figure 7.5 Two-dimensional Cantilever Beam

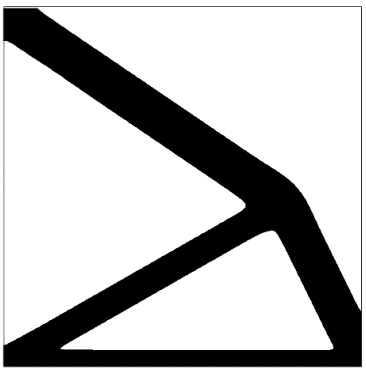

Figure 7.6 Reference design (Compliance: 50.05)

(a) Initial design

(b) Optimized design

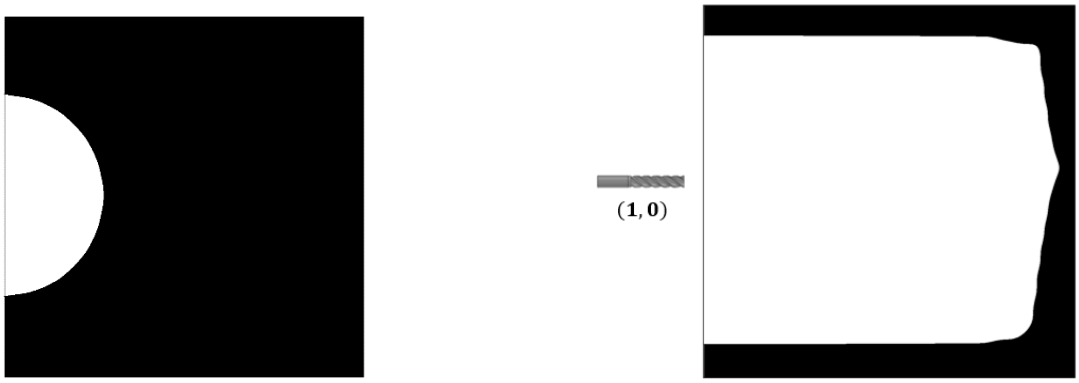

(a) Initial design

(b) Optimized design

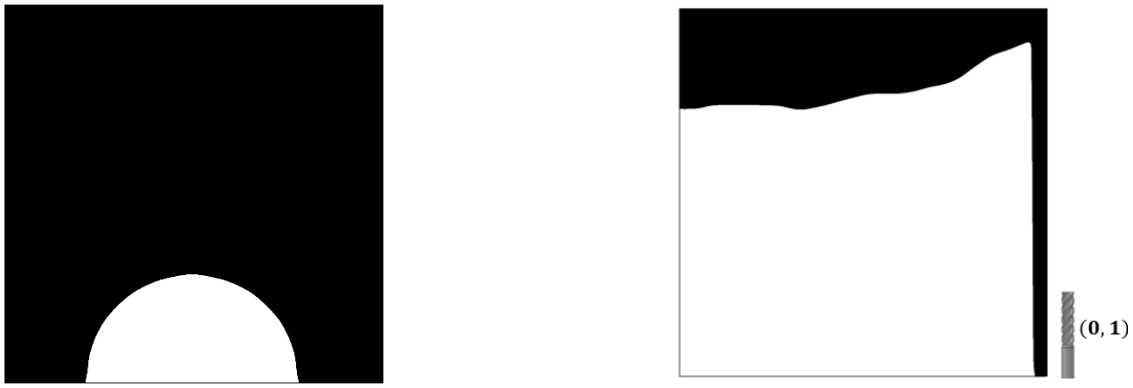

Figure 7.7 Designs obtained using single tool orientation

(a) Orientation (1,0)

(b) Orientation (0,1)

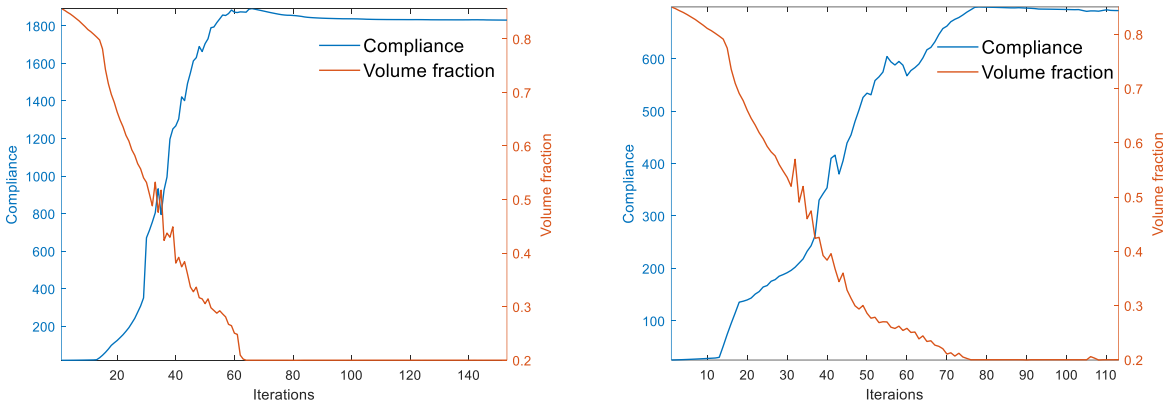

Figure 7.8 Convergence history

(a) Initial design

(b) Optimized design

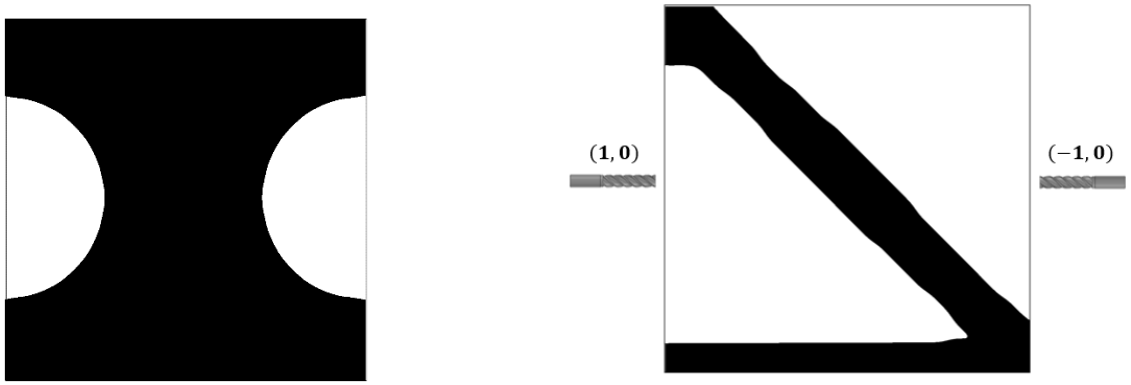

(a) Initial design

(b) Optimized design

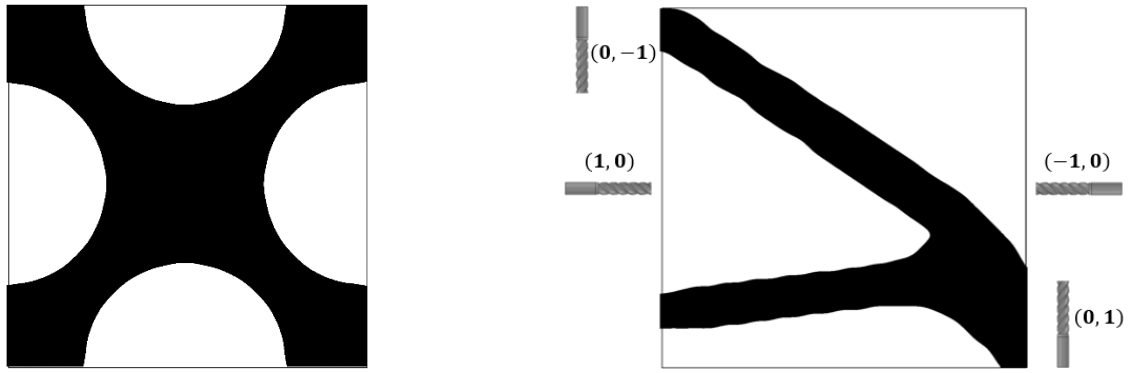

Figure 7.9 Designs obtained using multiple tool orientations

(a) 2 Orientations

(b) 4 Orientations

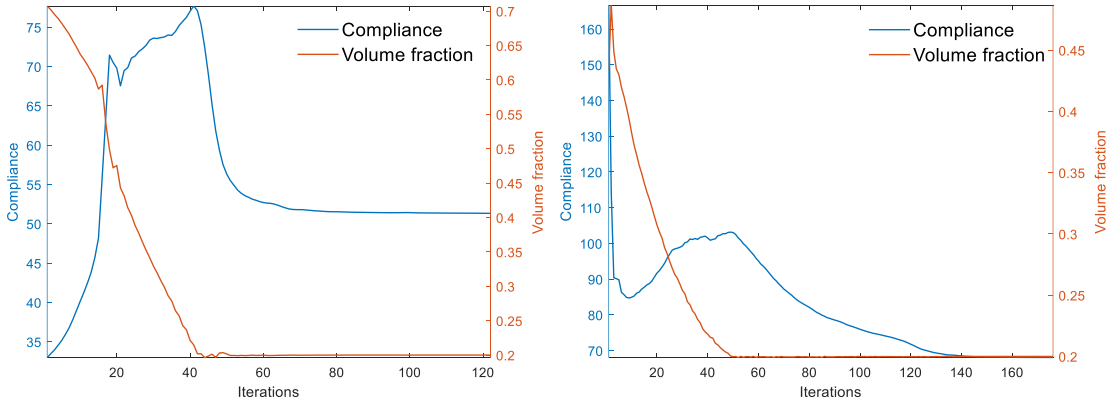

Figure 7.10 Convergence history

7.3.2 Machining-based Optimization for 3D Cantilever Beam

In this subsection, we focus on verifying the effectiveness of proposed method for 3D designs. In the first test example, a three-dimensional cantilever beam example is presented for compliance minimization. The unit force is applied at the midpoint of right-bottom edge, and the left end is fully fixed. The design domain is discretized by a $144 \times 48 \times 48$ hexahedral mesh with unit element length. The elastic constants are chosen as follows: Elastic modulus $E = 1$ and Poisson's ratio $\mu = 0.3$. The volume fraction constraint is set to be 0.3. The filter radius for multi-axis machining optimization is chosen as $r_{min} = 4$. A reference solution is demonstrated in Figure 7.13, where no machining constraints are applied. As shown in Figure 7.13, optimized design exists hollow chamber, which is not accessible by machine tools. It is worth to mention that the initialization of fictitious field for optimization is shown in Figure 7.12. To ensure the manufacturability of the optimized design, the results of two-orientation machining optimization for the Cantilever beam are plotted in Figure 7.14. The orientation of machine tool is described by the vector (a, b, c) in the local coordinate as shown in Figure 7.11. The compliance value of designs obtained from different orientations (Figure 7.14) is close and slightly higher than the reference design. For multi-axis machining constraints, the optimized result is demonstrated in Figure 7.15 with 6 different milling orientations. However, compliances differ slightly between all designs, which denotes the amount of directions is not very influential for current issue.

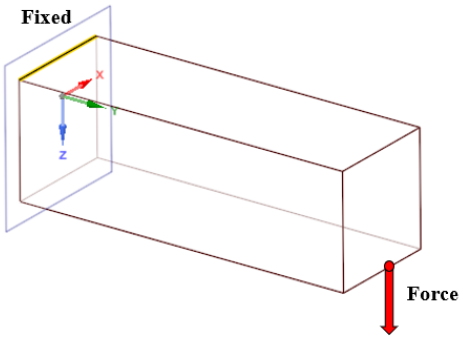

Figure 7.11 Three-dimensional Cantilever Beam

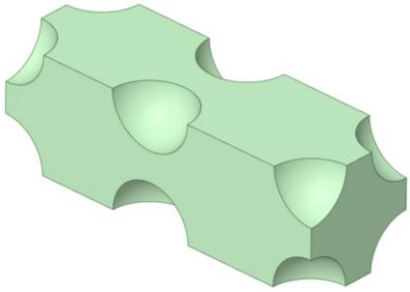

Figure 7.12 Initialization of fictitious field

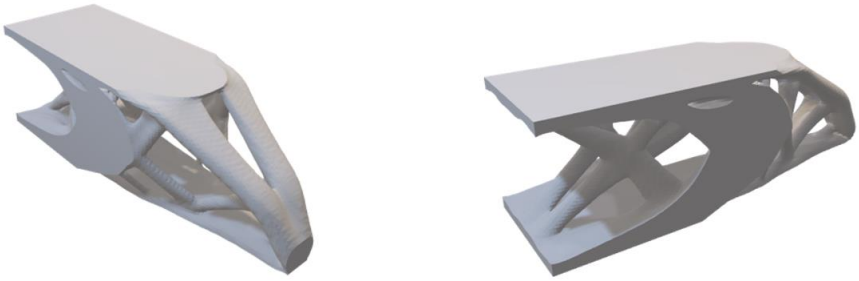

Figure 7.13 Reference solution without machining constraints (Compliance:10.43)

(a) Compliance:11.18

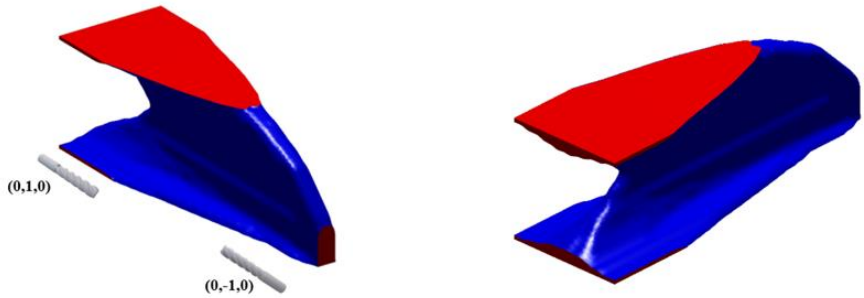

(b) Compliance:10.77

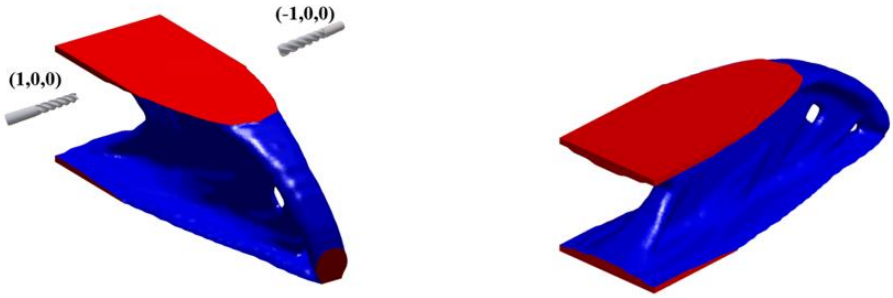

(c) Compliance:13.64

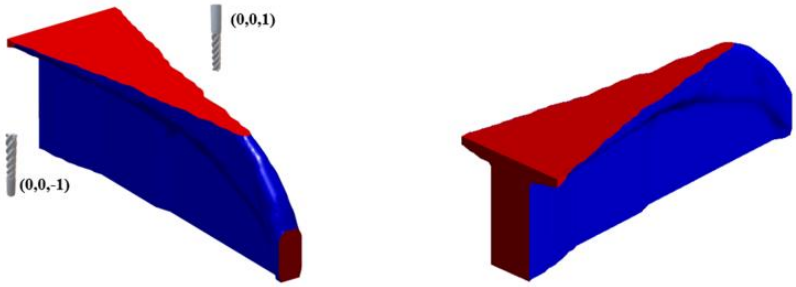

(d) Compliance:12.04

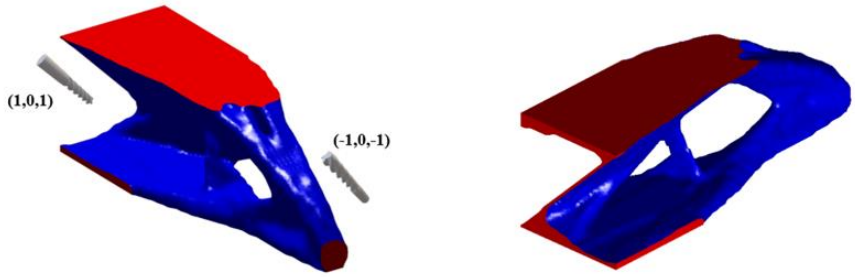

Figure 7.14 Two orientation machining constraints

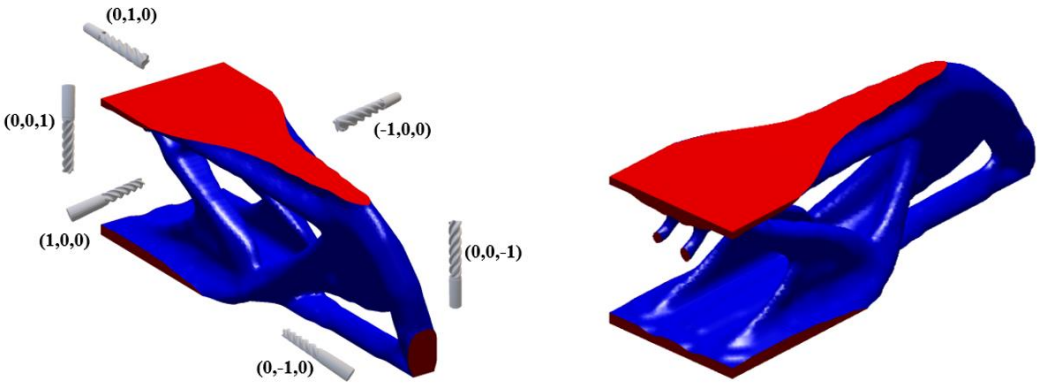

Figure 7.15 Multiple machining tool orientations (Compliance=11.85)

To further examine the effects of filter radius on final optimized design, different filter sizes r_{min} are selected to produce diverse designs as shown in Figure 7.16. The machining tool orientations (6 directions) are shown in Figure 7.15. As mentioned by Ref [207-209], filter size is a straightforward and effective way to control the member size of optimal design. As plotted in Figure 7.16, for small radius size ($r_{min} = 1$), small and narrow hollow chambers are found, which may not be accessible by machine tool. However, the hollow chamber size increases after increasing the filter radius r_{min}, while the compliance values (C) of multiple designs are close in this case.

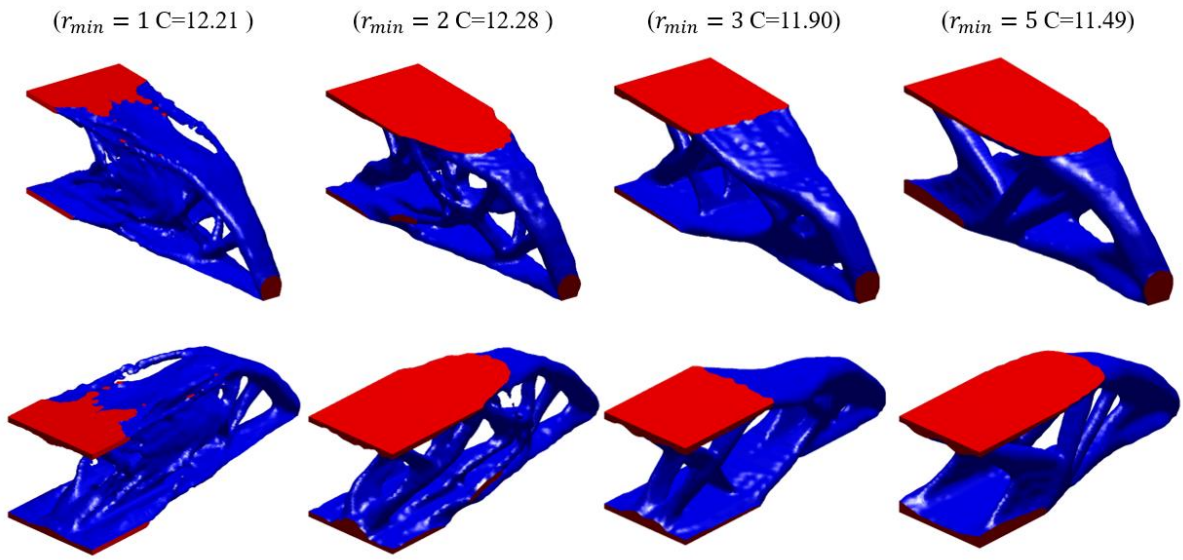

Figure 7.16 Machinable designs with different filter radius

7.3.3 Machining-based Optimization for 3D MBB Beam

In this section, an MBB Design example is presented for compliance minimization. The unit force is applied at the center of top face. Left and right bottom edges are fully fixed as shown in Figure 7.17. Due to the symmetry, only half of the MBB beam is chosen to optimize, where the half design domain is discretized by $144 \times 48 \times 48$ hexahedral mesh with unit element length. The material properties are the same as the previous example. The filter size for design variables is selected as $r_{min} = 4$. The volume constraint is chosen as $\bar{V} = 0.2$. The reference result without machining constraints obtained from standard density-based method is shown in Figure 7.19. This reference design is not manufacturable through machining as it contains several inaccessible internal surfaces. Similar to the previous example, we start by considering a two-opposite direction for milling operation. The initialization of fictitious field for optimization is demonstrated in Figure 7.18. Several machinable designs are generated through the proposed method as demonstrated in Figure 7.20. The machinable MBB designs have very different optimized

configurations compared to the reference case, while the compliance values of machinable designs are remarkably competitive with reference.

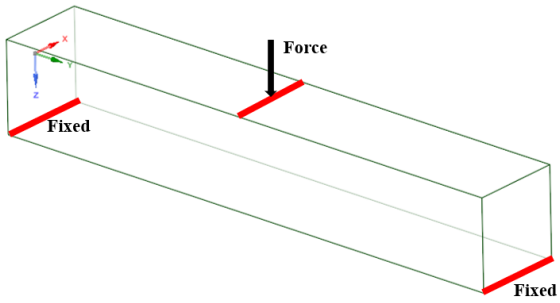

Figure 7.17 Machinable designs with different filter radius

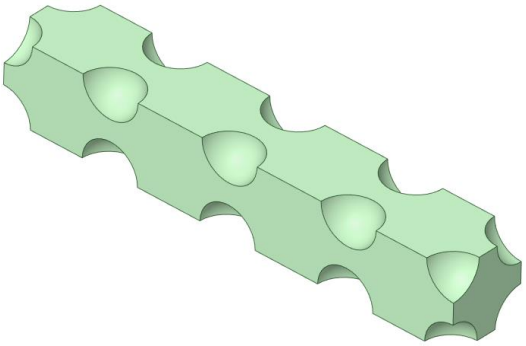

Figure 7.18 Initialization of fictitious field

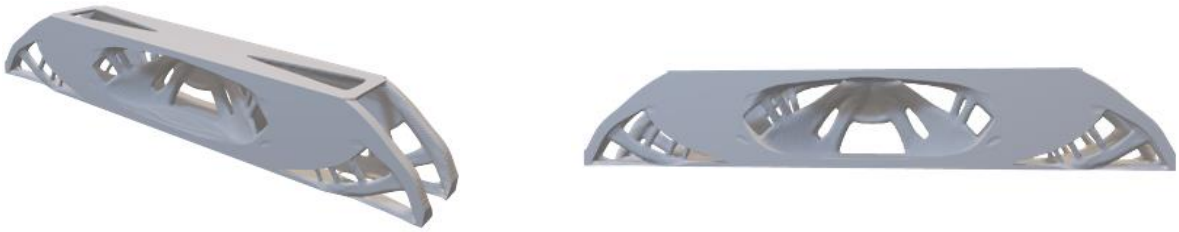

Figure 7.19 Reference design (Compliance=10.72)

(a) Compliance:11.38

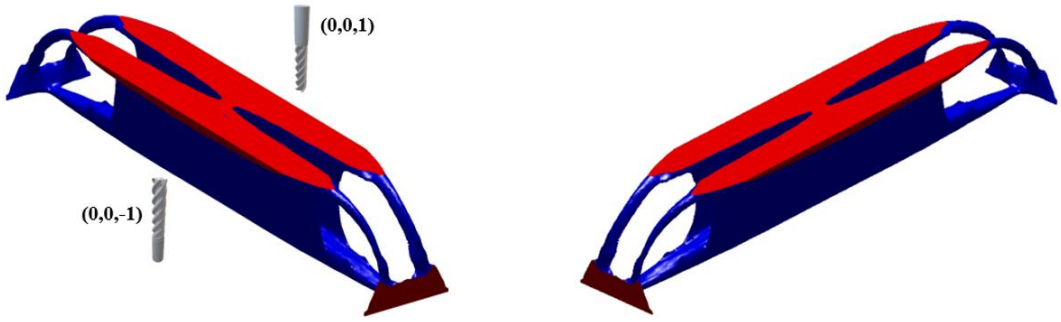

(b) Compliance:10.21

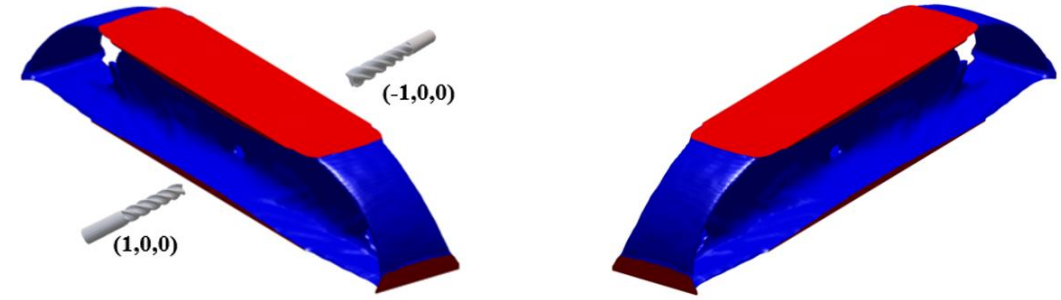

(c) Compliance: 11.09

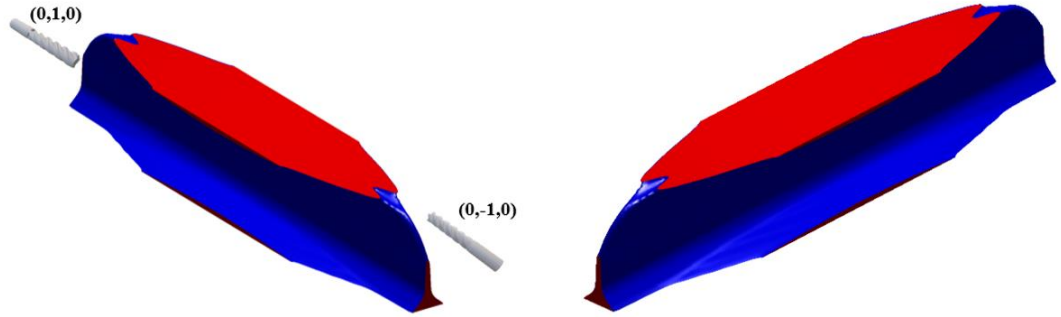

Figure 7.20 Two opposite milling directions

For a multi-axis milling scenario, the set of milling orientations is extended as shown in Figure 7.21. As plotted in Figure 7.21, the machinable design is obtained by 6 mutually orthogonal milling directions. The compliance value (C=10.05) of optimized design is slightly outperform

than the reference design (C=10.72). Clearly, the reference design is only a local optimum, as gradient-based method is only able to converge to a local minimum.

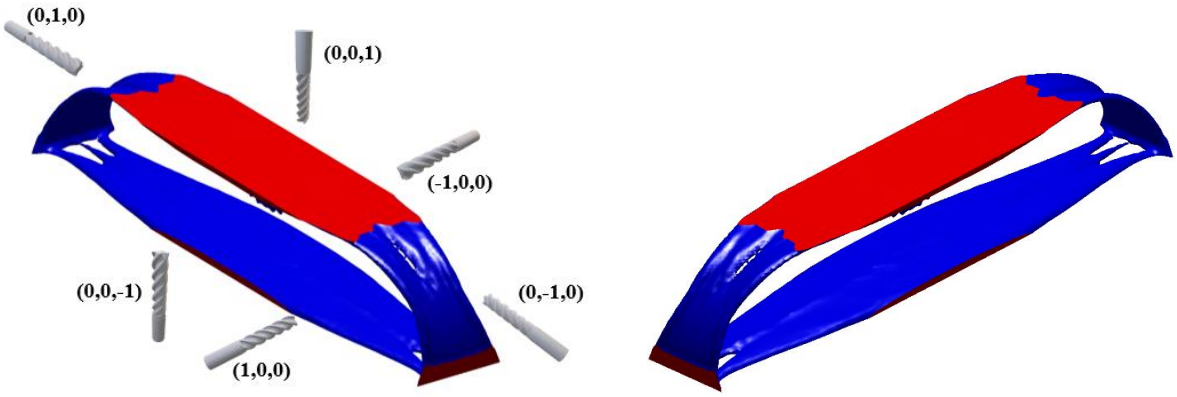

Figure 7.21 Multiple milling directions (Compliance: 10.05)

7.4 Conclusion

In recent years, developing advanced topology optimization methods for conventional subtractive manufacturing becomes a new trend in this field. In this chapter, a novel mathematical formulation to impose multi-axis machining restrictions in the framework of density-based method is proposed. A simple density mapping method based on Heaviside function for multi-axis restrictions is demonstrated in detail, where no aggregation functions (E.g. KS-function [202]) are involved. Several 2D and 3D numerical examples are demonstrated to validate the effectiveness of proposed method. The current study does not consider precisely controlling the length to diameter ratio (L:D ratio) of machinable design [210]. In general, some small features generated by topology optimization are hard to reach like a thin and deep pocket. For multi-axis machining, deep and narrow areas require specialized tooling and are time-consuming to produce. These narrow areas may require additional equipment setup and increase the cost of a component.

Increasing the filter radius as described in the proposed method can effectively reduce these narrow regions. In the future research, the length to diameter ratio will be investigated and incorporated into the current optimization framework.

8.0 Conclusions

8.1 Main Contributions

The research works in this dissertation are mainly focused on development of projection-based methods for topology and shape optimization. The projection-based topology optimization approach is able to properly restrict the optimal solutions by implementing geometric constraints. The core of projection method is to applying new design variables projected in a pseudo-density domain to find the optimal solutions. The main contributions of this dissertation are summarized as follows,

(1) **The projection-based method is proposed to maximum extreme energy dissipation of metamaterial considering failure constraint, where the geometric dimension can be controlled in a straightforward way.** Approximation of theoretical energy absorption is formulated through mathematical expression and strict sensitivities are deducted by adjoint method. Material failure is measured by strain energy and p-norm formulation are utilized. To explicit control and express geometric shape, an alternative projection method is presented for continuum-based topology optimization made of geometric components. This geometric projection algorithm is completely based on a fixed grid and hence inherit the advantages of density-based TO method. By applying the chain rule, the sensitivities with respect to geometry parameters are convenient to derive. This guarantees the application of gradient-based optimization frame with standard nonlinear programming algorithms. The density mapping algorithm in this article is based on Heaviside function, which is possessed of strong generality and can be extended to apply curved skeleton to control complex geometry shape in the future.

(2) **A Bézier skeleton explicit density (BSED) representation algorithm is proposed for the topology optimization of stretchable metamaterial, where manufacturing friendly structures without any intricate small features are generated for optimal design.** Material failure is measured by strain energy and p-norm formulation are utilized. A Heaviside function is applied to create a mapping from geometry skeleton to mesh grids, where the skeleton is described by the Bézier curves. This density representation method successfully inherits the main advantages of density-based topology optimization. Sensitivities of the objectives and constraints with respect to control parameters can be readily derived by using the chain rule. Due to the powerful curve fitting ability, using Bézier curve to represent density field can explore design space effectively compared to bar-like structures. Furthermore, this density representation method is mesh independent and the design variables are reduced significantly so that the optimization problem can be solved efficiently using regular optimization algorithm.

(3) **A new projection-based algorithm based on implicit field for gyroid lattice design is proposed, where the proposed method is able to design functionally graded lattice without the need for any homogenization.** Thus, the lattice design based on this method is not limited to periodic structures, and can be extended to irregular porous scaffold designs. The unit cell size for lattice design can be large and not limited by size effects (homogenization necessary condition [150]), which is preferred for AM. Now that the geometry is defined by implicit function, the geometry information is far less than feature-based geometry modeling [151], which is sometimes extremely tedious for modeling porous media or lattice structures, and the data communication between implicit field with additive manufacturing systems is well-addressed by Ref. [134].

(4) **A gradient-based moving particle optimization method is proposed to achieve reverse shape compensation under gravity stimuli, which is a general computational**

framework for reverse shape compensation. The geometry is represented by particles, where each particle can move freely in the design domain. Dual background mesh is implemented to achieve a mapping from undeformed geometry to deformed configuration. The update of particle positions is based on sensitivity information, and MMA optimizer is implemented to minimize the objective function. The method described here has the capability to treat more complex situation, such as temperature change. etc. Besides, the proposed method has the potential to be applied to engineering application such as distortion compensation in additive manufacturing or four-dimensional (4D) printing techniques

(5) **A new computational scheme for topology optimization is proposed, where the boundary of voids is described based on RBF interpolation method in an explicit way, and p-norm function is implemented to merge the multiple voids.** The proposed method is applied to design snap-through mechanism undergoing large deformation. The main advantages of the proposed approach can be summarized as: (1) The proposed computational scheme is in the framework of density-based method, where the sensitivity analysis for standard density-based method is directly utilized based on the chain rule. (2) The intermediate density only locates at the boundary region, which shares the advantages of level set based methods. The proposed method is better for circumventing the excessive mesh distortion issue in low density area. (3) Since the structural geometry is explicitly described, it is easy to incorporate some manufacturing constraints, e.g., feature size, curvature of the structural boundary, etc. (4) Merging multiple voids based on p-norm functions is straightforward and simple for numerical implementation.

(6) **A novel projection-based mathematical formulation to impose multi-axis machining restrictions in the framework of density-based method is proposed.** A simple density mapping method based on Heaviside function for multi-axis restrictions is demonstrated

in detail, where no aggregation functions (E.g. KS-function [202]) are involved. In general, some small features generated by topology optimization are hard to reach like a thin and deep pocket. These narrow areas may require additional equipment setup and increase the cost of a component. Increasing the filter radius as described in the proposed method can effectively reduce these narrow regions.

8.2 Future Works

Though several different projection-based methods are shown in this dissertation to control the geometric shape and dimension, there are still a lot of important topics that need to be further carefully investigated. The potential future works based on the research works in this dissertation are summarized as follows.

(1) **For buckling-induced and stretchable metamaterial design, extending the current method to three-dimensional design is a challenging thing, which should be addressed in the future.** How to effectively accelerate the finite element solution process for large scale nonlinear problems is a critical issue needed to be resolved. Meanwhile, employing GPU to accelerate the solution process is another promising direction in the future.

(2) **Projection-based Moving Particle Optimization Method will be extended to large deformation problem or elastic-plasticity problem.** In the present computational framework, only the small deformation is considered, and finite element analysis is still based on the linear elastic theory. Compared with nonlinear problem, the linear problem is stable for optimization even though the sensitivity is not fully correct due to some small derivation mistakes. However, for large deformation problem, the correctness of sensitivity derivation becomes more critical and

small deviation of sensitivities may result in divergence of optimization. Meanwhile, large deformation problem is sensitive to mesh distortion, where the local mesh distortion may result in failure of FEM analysis. However, the large deformation is common in soft matter deformation under stimuli or thin-walled structures produced by AM techniques. For parts produced by additive manufacturing, the local plasticity deformation is inevitable due to residual stress, which is caused by material expansion and shrinkage due to temperature change in manufacturing process. Thus, effective reverse shape compensation algorithm based on elastic-plasticity material model is essential to achieve the real application of proposed method for AM parts.

(3) **Topology optimization design with multi-axis machining restrictions should be extended to considering the tool shape and size.** In general, tool length limitations have a strong impact on part optimal shape and performance, how to effectively consider the tool length limitations and incorporated into current computational scheme is a challenge and should be further explored in the future.

Bibliography

[1] K. Suzuki and N. Kikuchi, "A homogenization method for shape and topology optimization," *Computer methods in applied mechanics and engineering,* vol. 93, no. 3, pp. 291-318, 1991.

[2] N. P. van Dijk, K. Maute, M. Langelaar, and F. Van Keulen, "Level-set methods for structural topology optimization: a review," *Structural and Multidisciplinary Optimization,* vol. 48, no. 3, pp. 437-472, 2013.

[3] X. Guo and G.-D. Cheng, "Recent development in structural design and optimization," *Acta Mechanica Sinica,* vol. 26, no. 6, pp. 807-823, 2010.

[4] O. Sigmund and K. Maute, "Topology optimization approaches," *Structural and Multidisciplinary Optimization,* vol. 48, no. 6, pp. 1031-1055, 2013.

[5] J. Liu *et al.*, "Current and future trends in topology optimization for additive manufacturing," *Structural and Multidisciplinary Optimization,* vol. 57, no. 6, pp. 2457-2483, 2018.

[6] M. Osanov and J. K. Guest, "Topology optimization for architected materials design," *Annual Review of Materials Research,* vol. 46, pp. 211-233, 2016.

[7] F. Wein, P. Dunning, and J. A. Norato, "A review on feature-mapping methods for structural optimization," *arXiv preprint arXiv:1910.10770,* 2019.

[8] M. P. Bendsøe, "Optimal shape design as a material distribution problem," *Structural optimization,* vol. 1, no. 4, pp. 193-202, 1989.

[9] G. Allaire, F. Jouve, and A.-M. Toader, "A level-set method for shape optimization," *Comptes Rendus Mathematique,* vol. 334, no. 12, pp. 1125-1130, 2002.

[10] G. Allaire, F. Jouve, and A.-M. Toader, "Structural optimization using sensitivity analysis and a level-set method," *Journal of computational physics,* vol. 194, no. 1, pp. 363-393, 2004.

[11] X. Guo, W. Zhang, and W. Zhong, "Doing Topology Optimization Explicitly and Geometrically—A New Moving Morphable Components Based Framework," *Journal of Applied Mechanics,* vol. 81, no. 8, 2014, doi: 10.1115/1.4027609.

[12] W. Zhang, J. Zhou, Y. Zhu, and X. Guo, "Structural complexity control in topology optimization via moving morphable component (MMC) approach," *Structural and Multidisciplinary Optimization,* vol. 56, no. 3, pp. 535-552, 2017.

[13] W. Zhang *et al.*, "Explicit three dimensional topology optimization via Moving Morphable Void (MMV) approach," *Computer Methods in Applied Mechanics and Engineering,* vol. 322, pp. 590-614, 2017.

[14] W. Zhang, D. Li, J. Zhou, Z. Du, B. Li, and X. Guo, "A moving morphable void (MMV)-based explicit approach for topology optimization considering stress constraints," *Computer Methods in Applied Mechanics and Engineering,* vol. 334, pp. 381-413, 2018.

[15] J. Norato, B. Bell, and D. Tortorelli, "A geometry projection method for continuum-based topology optimization with discrete elements," *Computer Methods in Applied Mechanics and Engineering,* vol. 293, pp. 306-327, 2015.

[16] S. Zhang, A. L. Gain, and J. A. Norato, "Adaptive mesh refinement for topology optimization with discrete geometric components," *Computer Methods in Applied Mechanics and Engineering,* vol. 364, p. 112930, 2020.

[17] H. Kazemi, A. Vaziri, and J. A. Norato, "Multi-material topology optimization of lattice structures using geometry projection," *Computer Methods in Applied Mechanics and Engineering,* vol. 363, p. 112895, 2020.

[18] S. Zhang, A. L. Gain, and J. A. Norato, "A geometry projection method for the topology optimization of curved plate structures with placement bounds," *International Journal for Numerical Methods in Engineering,* vol. 114, no. 2, pp. 128-146, 2018.

[19] S. Zhang, A. L. Gain, and J. A. Norato, "Stress-based topology optimization with discrete geometric components," *Computer Methods in Applied Mechanics and Engineering,* vol. 325, pp. 1-21, 2017.

[20] S. Watts and D. A. Tortorelli, "A geometric projection method for designing three-dimensional open lattices with inverse homogenization," *International Journal for Numerical Methods in Engineering,* vol. 112, no. 11, pp. 1564-1588, 2017.

[21] K. A. James and H. Waisman, "Layout design of a bi-stable cardiovascular stent using topology optimization," *Computer Methods in Applied Mechanics and Engineering,* vol. 305, pp. 869-890, 2016.

[22] S. Zhang, J. A. Norato, A. L. Gain, and N. Lyu, "A geometry projection method for the topology optimization of plate structures," *Structural and Multidisciplinary Optimization,* vol. 54, no. 5, pp. 1173-1190, 2016.

[23] H. Kazemi, A. Vaziri, and J. A. Norato, "Topology optimization of structures made of discrete geometric components with different materials," *Journal of Mechanical Design,* vol. 140, no. 11, 2018.

[24] J. Kato, D. Yachi, K. Terada, and T. Kyoya, "Topology optimization of micro-structure for composites applying a decoupling multi-scale analysis," *Structural and Multidisciplinary Optimization,* vol. 49, no. 4, pp. 595-608, 2014.

[25] X. S. Zhang, H. Chi, and G. H. Paulino, "Adaptive multi-material topology optimization with hyperelastic materials under large deformations: A virtual element approach," *Computer Methods in Applied Mechanics and Engineering*, vol. 370, p. 112976, 2020.

[26] O. Giraldo-Londoño and G. H. Paulino, "A unified approach for topology optimization with local stress constraints considering various failure criteria: von Mises, Drucker–Prager, Tresca, Mohr–Coulomb, Bresler–Pister and Willam–Warnke," *Proceedings of the Royal Society A*, vol. 476, no. 2238, p. 20190861, 2020.

[27] O. Sigmund, "A 99 line topology optimization code written in Matlab," *Structural and multidisciplinary optimization*, vol. 21, no. 2, pp. 120-127, 2001.

[28] M. P. Bendsøe and O. Sigmund, "Material interpolation schemes in topology optimization," *Archive of applied mechanics*, vol. 69, no. 9-10, pp. 635-654, 1999.

[29] M. Y. Wang, X. Wang, and D. Guo, "A level set method for structural topology optimization," *Computer methods in applied mechanics and engineering*, vol. 192, no. 1-2, pp. 227-246, 2003.

[30] X. Huang and Y.-M. Xie, "A further review of ESO type methods for topology optimization," *Structural and Multidisciplinary Optimization*, vol. 41, no. 5, pp. 671-683, 2010.

[31] Z. Liu, J. G. Korvink, and R. Huang, "Structure topology optimization: fully coupled level set method via FEMLAB," *Structural and Multidisciplinary Optimization*, vol. 29, no. 6, pp. 407-417, 2005.

[32] V. J. Challis, "A discrete level-set topology optimization code written in Matlab," *Structural and multidisciplinary optimization*, vol. 41, no. 3, pp. 453-464, 2010.

[33] K. Suresh, "A 199-line Matlab code for Pareto-optimal tracing in topology optimization," *Structural and Multidisciplinary Optimization*, vol. 42, no. 5, pp. 665-679, 2010.

[34] E. Andreassen, A. Clausen, M. Schevenels, B. S. Lazarov, and O. Sigmund, "Efficient topology optimization in MATLAB using 88 lines of code," *Structural and Multidisciplinary Optimization*, vol. 43, no. 1, pp. 1-16, 2011.

[35] C. Talischi, G. H. Paulino, A. Pereira, and I. F. Menezes, "PolyTop: a Matlab implementation of a general topology optimization framework using unstructured polygonal finite element meshes," *Structural and Multidisciplinary Optimization*, vol. 45, no. 3, pp. 329-357, 2012.

[36] T. Zegard and G. H. Paulino, "GRAND—Ground structure based topology optimization for arbitrary 2D domains using MATLAB," *Structural and Multidisciplinary Optimization*, vol. 50, no. 5, pp. 861-882, 2014.

[37] N. Aage, E. Andreassen, and B. S. Lazarov, "Topology optimization using PETSc: An easy-to-use, fully parallel, open source topology optimization framework," *Structural and Multidisciplinary Optimization,* vol. 51, no. 3, pp. 565-572, 2015.

[38] M. Otomori, T. Yamada, K. Izui, and S. Nishiwaki, "Matlab code for a level set-based topology optimization method using a reaction diffusion equation," *Structural and Multidisciplinary Optimization,* vol. 51, no. 5, pp. 1159-1172, 2015.

[39] L. Xia and P. Breitkopf, "Design of materials using topology optimization and energy-based homogenization approach in Matlab," *Structural and multidisciplinary optimization,* vol. 52, no. 6, pp. 1229-1241, 2015.

[40] A. Pereira, C. Talischi, G. H. Paulino, I. F. Menezes, and M. S. Carvalho, "Fluid flow topology optimization in PolyTop: stability and computational implementation," *Structural and Multidisciplinary Optimization,* vol. 54, no. 5, pp. 1345-1364, 2016.

[41] P. Wei, Z. Li, X. Li, and M. Y. Wang, "An 88-line MATLAB code for the parameterized level set method based topology optimization using radial basis functions," *Structural and Multidisciplinary Optimization,* vol. 58, no. 2, pp. 831-849, 2018.

[42] R. A. Loyola, O. M. Querin, A. G. Jiménez, and C. A. Gordoa, "A sequential element rejection and admission (SERA) topology optimization code written in Matlab," *Structural and Multidisciplinary Optimization,* vol. 58, no. 3, pp. 1297-1310, 2018.

[43] A. Laurain, "A level set-based structural optimization code using FEniCS," *Structural and Multidisciplinary Optimization,* vol. 58, no. 3, pp. 1311-1334, 2018.

[44] E. D. Sanders, A. Pereira, M. A. Aguiló, and G. H. Paulino, "PolyMat: an efficient Matlab code for multi-material topology optimization," *Structural and Multidisciplinary Optimization,* vol. 58, no. 6, pp. 2727-2759, 2018.

[45] C. Dapogny, P. Frey, F. Omnès, and Y. Privat, "Geometrical shape optimization in fluid mechanics using FreeFem++," *Structural and Multidisciplinary Optimization,* vol. 58, no. 6, pp. 2761-2788, 2018.

[46] Q. Chen, X. Zhang, and B. Zhu, "A 213-line topology optimization code for geometrically nonlinear structures," *Structural and Multidisciplinary Optimization,* vol. 59, no. 5, pp. 1863-1879, 2019.

[47] J. Gao, Z. Luo, L. Xia, and L. Gao, "Concurrent topology optimization of multiscale composite structures in Matlab," *Structural and Multidisciplinary Optimization,* vol. 60, no. 6, pp. 2621-2651, 2019.

[48] Y. Liang and G. Cheng, "Further elaborations on topology optimization via sequential integer programming and Canonical relaxation algorithm and 128-line MATLAB code," *Structural and Multidisciplinary Optimization,* vol. 61, no. 1, pp. 411-431, 2020.

[49] H. Smith and J. A. Norato, "A MATLAB code for topology optimization using the geometry projection method," *Structural and Multidisciplinary Optimization*, pp. 1-16, 2020.

[50] R. Picelli, R. Sivapuram, and Y. M. Xie, "A 101-line MATLAB code for topology optimization using binary variables and integer programming," *Structural and Multidisciplinary Optimization*, pp. 1-20, 2020.

[51] H. Lin, A. Xu, A. Misra, and R. Zhao, "An ANSYS APDL code for topology optimization of structures with multi-constraints using the BESO method with dynamic evolution rate (DER-BESO)," *Structural and Multidisciplinary Optimization*, pp. 1-26, 2020.

[52] F. Ferrari and O. Sigmund, "A new generation 99 line Matlab code for compliance Topology Optimization and its extension to 3D," *arXiv preprint arXiv:2005.05436*, 2020.

[53] J. T. Overvelde *et al.*, "A three-dimensional actuated origami-inspired transformable metamaterial with multiple degrees of freedom," *Nature communications*, vol. 7, no. 1, pp. 1-8, 2016.

[54] Z. Yan *et al.*, "Controlled mechanical buckling for origami-inspired construction of 3D microstructures in advanced materials," *Advanced functional materials*, vol. 26, no. 16, pp. 2629-2639, 2016.

[55] T. Li *et al.*, "Fast-moving soft electronic fish," *Science Advances*, vol. 3, no. 4, p. e1602045, 2017.

[56] T. E. Bruns and D. A. Tortorelli, "Topology optimization of non-linear elastic structures and compliant mechanisms," *Computer methods in applied mechanics and engineering*, vol. 190, no. 26-27, pp. 3443-3459, 2001.

[57] M. Wallin, N. Ivarsson, and D. Tortorelli, "Stiffness optimization of non-linear elastic structures," *Computer Methods in Applied Mechanics and Engineering*, vol. 330, pp. 292-307, 2018.

[58] F. Wang, B. S. Lazarov, O. Sigmund, and J. S. Jensen, "Interpolation scheme for fictitious domain techniques and topology optimization of finite strain elastic problems," *Computer Methods in Applied Mechanics and Engineering*, vol. 276, pp. 453-472, 2014.

[59] N. Ivarsson, M. Wallin, and D. Tortorelli, "Topology optimization of finite strain viscoplastic systems under transient loads," *International Journal for Numerical Methods in Engineering*, vol. 114, no. 13, pp. 1351-1367, 2018.

[60] Y. Li, J. Zhu, F. Wang, W. Zhang, and O. Sigmund, "Shape preserving design of geometrically nonlinear structures using topology optimization," *Structural and Multidisciplinary Optimization*, vol. 59, no. 4, pp. 1033-1051, 2019.

[61] Y. Luo, M. Y. Wang, and Z. Kang, "Topology optimization of geometrically nonlinear structures based on an additive hyperelasticity technique," *Computer methods in applied mechanics and engineering*, vol. 286, pp. 422-441, 2015.

[62] R. Ortigosa, D. Ruiz, A. Gil, A. Donoso, and J. Bellido, "A stabilisation approach for topology optimisation of hyperelastic structures with the SIMP method," *Computer Methods in Applied Mechanics and Engineering*, vol. 364, p. 112924, 2020.

[63] F. Chen, Y. Wang, M. Y. Wang, and Y. Zhang, "Topology optimization of hyperelastic structures using a level set method," *Journal of Computational Physics*, vol. 351, pp. 437-454, 2017.

[64] Y. Luo, M. Li, and Z. Kang, "Topology optimization of hyperelastic structures with frictionless contact supports," *International Journal of Solids and Structures*, vol. 81, pp. 373-382, 2016.

[65] H. Chung, O. Amir, and H. A. Kim, "Level-set topology optimization considering nonlinear thermoelasticity," *Computer Methods in Applied Mechanics and Engineering*, vol. 361, p. 112735, 2020.

[66] R. Xue *et al.*, "Explicit structural topology optimization under finite deformation via moving morphable void (MMV) approach," *Computer Methods in Applied Mechanics and Engineering*, vol. 344, pp. 798-818, 2019.

[67] J. Kato, D. Yachi, T. Kyoya, and K. Terada, "Micro-macro concurrent topology optimization for nonlinear solids with a decoupling multiscale analysis," *International Journal for Numerical Methods in Engineering*, vol. 113, no. 8, pp. 1189-1213, 2018.

[68] H. Deng, L. Cheng, X. Liang, D. Hayduke, and A. C. To, "Topology optimization for energy dissipation design of lattice structures through snap-through behavior," *Computer Methods in Applied Mechanics and Engineering*, vol. 358, p. 112641, 2020.

[69] H. Deng, S. Hinnebusch, and A. C. To, "Topology optimization design of stretchable metamaterials with Bézier skeleton explicit density (BSED) representation algorithm," *Computer Methods in Applied Mechanics and Engineering*, vol. 366, p. 113093, 2020.

[70] T. Nishino, J. Kato, and T. Kyoya, "Topology optimization with Geometrical Nonlinearity Considering Uncertain loading Condition," *Transactions of the Japan Society for Computational Engineering and Science*, vol. 2019, p. 20190004, 2019.

[71] J. Kato, D. Yachi, S. Nishizawa, S. Takase, K. Terada, and T. Kyoya, "Topology optimization of microstructures for hyperelastic composites based on a decoupling multi-scale analysis," *Transactions of the Japan Society for Computational Engineering and Science*, vol. 2015, 2015.

[72] J. Bonet and R. D. Wood, *Nonlinear continuum mechanics for finite element analysis*. Cambridge university press, 1997.

[73] T. Belytschko, W. K. Liu, B. Moran, and K. Elkhodary, *Nonlinear finite elements for continua and structures*. John wiley & sons, 2013.

[74] N.-H. Kim, *Introduction to nonlinear finite element analysis*. Springer Science & Business Media, 2014.

[75] J. N. Reddy, *An Introduction to Nonlinear Finite Element Analysis: with applications to heat transfer, fluid mechanics, and solid mechanics*. OUP Oxford, 2014.

[76] A. Dorfmann and A. Muhr, *Constitutive models for rubber*. CRC Press, 1999.

[77] M. Mooney, "A theory of large elastic deformation," *Journal of applied physics,* vol. 11, no. 9, pp. 582-592, 1940.

[78] C. B. Pedersen, T. Buhl, and O. Sigmund, "Topology synthesis of large-displacement compliant mechanisms," *International Journal for numerical methods in engineering,* vol. 50, no. 12, pp. 2683-2705, 2001.

[79] T. E. Bruns and D. A. Tortorelli, "An element removal and reintroduction strategy for the topology optimization of structures and compliant mechanisms," *International journal for numerical methods in engineering,* vol. 57, no. 10, pp. 1413-1430, 2003.

[80] F. Wang, B. S. Lazarov, O. Sigmund, J. S. J. C. M. i. A. M. Jensen, and Engineering, "Interpolation scheme for fictitious domain techniques and topology optimization of finite strain elastic problems," vol. 276, pp. 453-472, 2014.

[81] M. Crisfield, "An arc-length method including line searches and accelerations," *International journal for numerical methods in engineering,* vol. 19, no. 9, pp. 1269-1289, 1983.

[82] M. Ritto-Corrêa and D. Camotim, "On the arc-length and other quadratic control methods: Established, less known and new implementation procedures," *Computers & Structures,* vol. 86, no. 11-12, pp. 1353-1368, 2008.

[83] Y.-B. Yang and M.-S. Shieh, "Solution method for nonlinear problems with multiple critical points," *AIAA journal,* vol. 28, no. 12, pp. 2110-2116, 1990.

[84] S. E. Leon, E. N. Lages, C. N. de Araújo, and G. H. Paulino, "On the effect of constraint parameters on the generalized displacement control method," *Mechanics Research Communications,* vol. 56, pp. 123-129, 2014.

[85] G. Moore and A. Spence, "The calculation of turning points of nonlinear equations," *SIAM Journal on Numerical Analysis,* vol. 17, no. 4, pp. 567-576, 1980.

[86] P. Wriggers and J. Simo, "A general procedure for the direct computation of turning and bifurcation points," *International journal for numerical methods in engineering,* vol. 30, no. 1, pp. 155-176, 1990.

[87] P.-O. Persson and G. Strang, "A simple mesh generator in MATLAB," *SIAM review,* vol. 46, no. 2, pp. 329-345, 2004.

[88] J.-F. Bonnans, J. C. Gilbert, C. Lemaréchal, and C. A. Sagastizábal, *Numerical optimization: theoretical and practical aspects*. Springer Science & Business Media, 2006.

[89] P. T. Boggs and J. W. Tolle, "Sequential quadratic programming," *Acta numerica,* vol. 4, pp. 1-51, 1995.

[90] B. Haghpanah, A. Shirazi, L. Salari-Sharif, A. G. Izard, and L. Valdevit, "Elastic architected materials with extreme damping capacity," *Extreme Mechanics Letters,* vol. 17, pp. 56-61, 2017.

[91] W. Wang *et al.*, "Novel slide-ring material/natural rubber composites with high damping property," *Scientific reports,* vol. 6, p. 22810, 2016.

[92] K. Volokh, "Comparison of biomechanical failure criteria for abdominal aortic aneurysm," *Journal of biomechanics,* vol. 43, no. 10, pp. 2032-2034, 2010.

[93] E. Holmberg, B. Torstenfelt, and A. Klarbring, "Stress constrained topology optimization," *Structural and Multidisciplinary Optimization,* vol. 48, no. 1, pp. 33-47, 2013.

[94] K. Svanberg, "The method of moving asymptotes—a new method for structural optimization," *International journal for numerical methods in engineering,* vol. 24, no. 2, pp. 359-373, 1987.

[95] A. Patel and K. Mequanint, "Hydrogel biomaterials," in *Biomedical engineering-frontiers and challenges*: IntechOpen, 2011.

[96] Y. Jiang and Q. Wang, "Highly-stretchable 3D-architected mechanical metamaterials," *Scientific reports,* vol. 6, p. 34147, 2016.

[97] F. Wang, O. Sigmund, and J. S. Jensen, "Design of materials with prescribed nonlinear properties," *Journal of the Mechanics and Physics of Solids,* vol. 69, pp. 156-174, 2014.

[98] Q. Gu, M. Barbato, and J. P. Conte, "Handling of constraints in finite-element response sensitivity analysis," *Journal of Engineering Mechanics,* vol. 135, no. 12, pp. 1427-1438, 2009.

[99] P. Trapper and K. Volokh, "Elasticity with energy limiters for modeling dynamic failure propagation," *International Journal of Solids and Structures,* vol. 47, no. 25-26, pp. 3389-3396, 2010.

[100] K. Volokh and H. Gao, "On the modified virtual internal bond method," *Journal of Applied Mechanics,* vol. 72, no. 6, pp. 969-971, 2005.

[101] K. Volokh, "Hyperelasticity with softening for modeling materials failure," *Journal of the Mechanics and Physics of Solids,* vol. 55, no. 10, pp. 2237-2264, 2007.

[102] P. Trapper and K. Volokh, "Modeling dynamic failure in rubber," *International Journal of Fracture*, vol. 162, no. 1-2, pp. 245-253, 2010.

[103] K. Volokh and P. Trapper, "Fracture toughness from the standpoint of softening hyperelasticity," *Journal of the Mechanics and Physics of Solids*, vol. 56, no. 7, pp. 2459-2472, 2008.

[104] K. Y. Volokh, "Multiscale modeling of material failure: From atomic bonds to elasticity with energy limiters," *International Journal for Multiscale Computational Engineering*, vol. 6, no. 5, 2008.

[105] D. Rittel, Z. Wang, and M. Merzer, "Adiabatic shear failure and dynamic stored energy of cold work," *Physical review letters*, vol. 96, no. 7, p. 075502, 2006.

[106] B. Mueller, "Additive manufacturing technologies–Rapid prototyping to direct digital manufacturing," *Assembly Automation*, 2012.

[107] H. A. Karimi and B. Akinci, *CAD and GIS integration*. CRC Press, 2009.

[108] J. Chung, D. Patel, R. Cook, and M. K. Simmons, "Feature-based modeling for mechanical design," *Computers Graphics*, vol. 14, no. 2, pp. 189-199, 1990.

[109] S. Sivakumar and V. Dhanalakshmi, "An approach towards the integration of CAD/CAM/CAI through STEP file using feature extraction for cylindrical parts," *International Journal of Computer Integrated Manufacturing*, vol. 26, no. 6, pp. 561-570, 2013.

[110] J. Brennan-Craddock, D. Brackett, R. Wildman, and R. Hague, "The design of impact absorbing structures for additive manufacture," in *Journal of Physics: Conference Series*, 2012, vol. 382, no. 1: IOP Publishing, p. 012042.

[111] I. Maskery *et al.*, "An investigation into reinforced and functionally graded lattice structures," *Journal of Cellular Plastics*, vol. 53, no. 2, pp. 151-165, 2017.

[112] X. Wang *et al.*, "Topological design and additive manufacturing of porous metals for bone scaffolds and orthopaedic implants: A review," *Biomaterials*, vol. 83, pp. 127-141, 2016.

[113] A. Panesar, M. Abdi, D. Hickman, and I. Ashcroft, "Strategies for functionally graded lattice structures derived using topology optimisation for additive manufacturing," *Additive Manufacturing*, vol. 19, pp. 81-94, 2018.

[114] D. Brackett, I. Ashcroft, R. Wildman, and R. J. Hague, "An error diffusion based method to generate functionally graded cellular structures," *Computers Structures*, vol. 138, pp. 102-111, 2014.

[115] S. C. Kapfer, S. T. Hyde, K. Mecke, C. H. Arns, and G. E. Schröder-Turk, "Minimal surface scaffold designs for tissue engineering," *Biomaterials*, vol. 32, no. 29, pp. 6875-6882, 2011.

[116] L. Cheng, J. Bai, and A. C. To, "Functionally graded lattice structure topology optimization for the design of additive manufactured components with stress constraints," *Computer Methods in Applied Mechanics Engineering,* vol. 344, pp. 334-359, 2019.

[117] J. Groen, F. Stutz, N. Aage, J. A. Bærentzen, and O. Sigmund, "De-homogenization of optimal multi-scale 3D topologies," *arXiv preprint arXiv:.13002,* 2019.

[118] J. P. Groen, J. Wu, and O. Sigmund, "Homogenization-based stiffness optimization and projection of 2D coated structures with orthotropic infill," *Computer Methods in Applied Mechanics Engineering,* vol. 349, pp. 722-742, 2019.

[119] J. P. Groen and O. Sigmund, "Homogenization-based topology optimization for high-resolution manufacturable microstructures," *International Journal for Numerical Methods in Engineering,* vol. 113, no. 8, pp. 1148-1163, 2018.

[120] J. Wu, A. Clausen, and O. Sigmund, "Minimum compliance topology optimization of shell–infill composites for additive manufacturing," *Computer Methods in Applied Mechanics Engineering,* vol. 326, pp. 358-375, 2017.

[121] L. Cheng, P. Zhang, E. Biyikli, J. Bai, J. Robbins, and A. To, "Efficient design optimization of variable-density cellular structures for additive manufacturing: theory and experimental validation," *Rapid Prototyping Journal,* 2017.

[122] H. Zeinalabedini, Y. O. Yildiz, P. Zhang, K. Laux, M. Kirca, and A. C. To, "Homogenization of additive manufactured polymeric foams with spherical cells," *Additive Manufacturing,* vol. 12, pp. 274-281, 2016.

[123] P. Zhang *et al.*, "Efficient design-optimization of variable-density hexagonal cellular structure by additive manufacturing: theory and validation," *Journal of Manufacturing Science Engineering,* vol. 137, no. 2, 2015.

[124] L. Xia and P. Breitkopf, "Multiscale structural topology optimization with an approximate constitutive model for local material microstructure," *Computer Methods in Applied Mechanics Engineering,* vol. 286, pp. 147-167, 2015.

[125] L. Xia, *Multiscale structural topology optimization*. Elsevier, 2016.

[126] F. Fritzen, L. Xia, M. Leuschner, and P. Breitkopf, "Topology optimization of multiscale elastoviscoplastic structures," *International Journal for Numerical Methods in Engineering,* vol. 106, no. 6, pp. 430-453, 2016.

[127] L. Xia and P. Breitkopf, "Recent advances on topology optimization of multiscale nonlinear structures," *Archives of Computational Methods in Engineering,* vol. 24, no. 2, pp. 227-249, 2017.

[128] D. Da, J. Yvonnet, L. Xia, M. V. Le, and G. Li, "Topology optimization of periodic lattice structures taking into account strain gradient," *Computers Structures,* vol. 210, pp. 28-40, 2018.

[129] J. Fu, L. Xia, L. Gao, M. Xiao, and H. Li, "Topology optimization of periodic structures with substructuring," *Journal of Mechanical Design,* vol. 141, no. 7, p. 071403, 2019.

[130] M. Xu, L. Xia, S. Wang, L. Liu, and X. Xie, "An isogeometric approach to topology optimization of spatially graded hierarchical structures," *Composite Structures,* vol. 225, p. 111171, 2019.

[131] Y. Zhu, S. Li, Z. Du, C. Liu, X. Guo, and W. Zhang, "A novel asymptotic-analysis-based homogenisation approach towards fast design of infill graded microstructures," *Journal of the Mechanics Physics of Solids,* vol. 124, pp. 612-633, 2019.

[132] A. Clausen, E. Andreassen, and O. Sigmund, "Topology optimization of 3D shell structures with porous infill," *Acta Mechanica Sinica,* vol. 33, no. 4, pp. 778-791, 2017.

[133] P. Geoffroy-Donders, G. Allaire, and O. Pantz, "3-d topology optimization of modulated and oriented periodic microstructures by the homogenization method," *Journal of Computational Physics,* vol. 401, p. 108994, 2020.

[134] Q. Li, Q. Hong, Q. Qi, X. Ma, X. Han, and J. Tian, "Towards additive manufacturing oriented geometric modeling using implicit functions," *Visual Computing for Industry, Biomedicine, Art,* vol. 1, no. 1, pp. 1-16, 2018.

[135] A. Ricci, "A constructive geometry for computer graphics," *The Computer Journal,* vol. 16, no. 2, pp. 157-160, 1973.

[136] D. J. Yoo, "Porous scaffold design using the distance field and triply periodic minimal surface models," *Biomaterials,* vol. 32, no. 31, pp. 7741-7754, 2011.

[137] D. W. Abueidda, M. Elhebeary, C.-S. A. Shiang, S. Pang, R. K. A. Al-Rub, and I. M. Jasiuk, "Mechanical properties of 3D printed polymeric Gyroid cellular structures: Experimental and finite element study," *Materials Design,* vol. 165, p. 107597, 2019.

[138] D.-J. Yoo, "Advanced porous scaffold design using multi-void triply periodic minimal surface models with high surface area to volume ratios," *International journal of precision engineering manufacturing,* vol. 15, no. 8, pp. 1657-1666, 2014.

[139] E. Kansa, H. Power, G. Fasshauer, and L. Ling, "A volumetric integral radial basis function method for time-dependent partial differential equations. I. Formulation," *Engineering Analysis with Boundary Elements,* vol. 28, no. 10, pp. 1191-1206, 2004.

[140] A. D. Cheng, M. Golberg, E. Kansa, and G. Zammito, "Exponential convergence and H-c multiquadric collocation method for partial differential equations," *Numerical Methods for Partial Differential Equations: An International Journal,* vol. 19, no. 5, pp. 571-594, 2003.

[141] D. Li, W. Liao, N. Dai, and Y. M. Xie, "Anisotropic design and optimization of conformal gradient lattice structures," *Computer-Aided Design,* vol. 119, p. 102787, 2020.

[142] L. Cheng, J. Liu, and A. C. To, "Concurrent lattice infill with feature evolution optimization for additive manufactured heat conduction design," *Structural Multidisciplinary Optimization,* vol. 58, no. 2, pp. 511-535, 2018.

[143] A. Bensoussan, J.-L. Lions, and G. Papanicolaou, *Asymptotic analysis for periodic structures*. American Mathematical Soc., 2011.

[144] J. Feng, J. Fu, Z. Lin, C. Shang, and B. Li, "A review of the design methods of complex topology structures for 3D printing," *Visual Computing for Industry, Biomedicine, Art,* vol. 1, no. 1, p. 5, 2018.

[145] G. Wang *et al.*, "Design and compressive behavior of controllable irregular porous scaffolds: based on voronoi-tessellation and for additive manufacturing," *ACS Biomaterials Science Engineering,* vol. 4, no. 2, pp. 719-727, 2018.

[146] E. Andreassen, A. Clausen, M. Schevenels, B. S. Lazarov, and O. Sigmund, "Efficient topology optimization in MATLAB using 88 lines of code," *Structural Multidisciplinary Optimization,* vol. 43, no. 1, pp. 1-16, 2011.

[147] E. Pärt-Enander, A. Sjöberg, B. Melin, and P. Isaksson, *The MATLAB handbook*. Addison-Wesley Harlow, 1996.

[148] S. Rahmatalla and C. Swan, "A Q4/Q4 continuum structural topology optimization implementation," *Structural Multidisciplinary Optimization,* vol. 27, no. 1-2, pp. 130-135, 2004.

[149] D. Herzog, V. Seyda, E. Wycisk, and C. Emmelmann, "Additive manufacturing of metals," *Acta Materialia,* vol. 117, pp. 371-392, 2016.

[150] I. Goda, F. Dos Reis, and J.-F. Ganghoffer, "Limit analysis of lattices based on the asymptotic homogenization method and prediction of size effects in bone plastic collapse," in *Generalized Continua as Models for Classical and Advanced Materials*: Springer, 2016, pp. 179-211.

[151] O. W. Salomons, F. J. van Houten, and H. Kals, "Review of research in feature-based design," *Journal of manufacturing systems,* vol. 12, no. 2, pp. 113-132, 1993.

[152] H. Meng and G. Li, "A review of stimuli-responsive shape memory polymer composites," *Polymer,* vol. 54, no. 9, pp. 2199-2221, 2013.

[153] Q. Meng and J. Hu, "A review of shape memory polymer composites and blends," *Composites Part A: Applied Science and Manufacturing,* vol. 40, no. 11, pp. 1661-1672, 2009.

[154] C. Y. Yap *et al.*, "Review of selective laser melting: Materials and applications," *Applied physics reviews,* vol. 2, no. 4, p. 041101, 2015.

[155] K. Xu, T.-H. Kwok, Z. Zhao, and Y. Chen, "A reverse compensation framework for shape deformation control in additive manufacturing," *Journal of Computing and Information Science in Engineering,* vol. 17, no. 2, 2017.

[156] K. Tong, E. A. Lehtihet, and S. Joshi, "Parametric error modeling and software error compensation for rapid prototyping," *Rapid Prototyping Journal,* 2003.

[157] W. Zha and S. Anand, "Geometric approaches to input file modification for part quality improvement in additive manufacturing," *Journal of Manufacturing Processes,* vol. 20, pp. 465-477, 2015.

[158] S. Afazov, W. A. Denmark, B. L. Toralles, A. Holloway, and A. Yaghi, "Distortion prediction and compensation in selective laser melting," *Additive Manufacturing,* vol. 17, pp. 15-22, 2017.

[159] A. Yaghi, S. Ayvar-Soberanis, S. Moturu, R. Bilkhu, and S. Afazov, "Design against distortion for additive manufacturing," *Additive Manufacturing,* vol. 27, pp. 224-235, 2019.

[160] S. Afazov *et al.*, "A methodology for precision additive manufacturing through compensation," *Precision Engineering,* vol. 50, pp. 269-274, 2017.

[161] G. Sossou, F. Demoly, H. Belkebir, H. J. Qi, S. Gomes, and G. Montavon, "Design for 4D printing: Modeling and computation of smart materials distributions," *Materials & Design,* vol. 181, p. 108074, 2019.

[162] A. S. Gladman, E. A. Matsumoto, R. G. Nuzzo, L. Mahadevan, and J. A. Lewis, "Biomimetic 4D printing," *Nature materials,* vol. 15, no. 4, pp. 413-418, 2016.

[163] F. Momeni, X. Liu, and J. Ni, "A review of 4D printing," *Materials & design,* vol. 122, pp. 42-79, 2017.

[164] H. Li, X. Guo, R. G. Nuzzo, and K. J. Hsia, "Capillary induced self-assembly of thin foils into 3Dstructures," *Journal of the Mechanics and Physics of Solids,* vol. 58, no. 12, pp. 2033-2042, 2010.

[165] A. M. Abdullah, X. Li, P. V. Braun, J. A. Rogers, and K. J. Hsia, "Kirigami-Inspired Self-Assembly of 3D Structures," *Advanced Functional Materials,* 2020.

[166] A. M. Abdullah, X. Li, P. V. Braun, J. A. Rogers, and K. J. Hsia, "Self-Folded Gripper-Like Architectures from Stimuli-Responsive Bilayers," *Advanced Materials,* vol. 30, no. 31, p. 1801669, 2018.

[167] C. Huang, D. Quinn, S. Suresh, and K. J. Hsia, "Controlled molecular self-assembly of complex three-dimensional structures in soft materials," *Proceedings of the National Academy of Sciences,* vol. 115, no. 1, pp. 70-74, 2018.

[168] C. Huang, D. Quinn, Y. Sadovsky, S. Suresh, and K. J. Hsia, "Formation and size distribution of self-assembled vesicles," *Proceedings of the National Academy of Sciences,* vol. 114, no. 11, pp. 2910-2915, 2017.

[169] X. Huang and Y. Xie, "Evolutionary topology optimization of continuum structures including design-dependent self-weight loads," *Finite Elements in Analysis and Design,* vol. 47, no. 8, pp. 942-948, 2011.

[170] Z. Zhang, G. Li, H. Lu, Y. Ouyang, M. Yin, and C. Xian, "Fast as-isometric-as-possible shape interpolation," *Computers & Graphics,* vol. 46, pp. 244-256, 2015.

[171] S.-Y. Baek, J. Lim, and K. Lee, "Isometric shape interpolation," *Computers & Graphics,* vol. 46, pp. 257-263, 2015.

[172] P. von Radziewsky, E. Eisemann, H.-P. Seidel, and K. Hildebrandt, "Optimized subspaces for deformation-based modeling and shape interpolation," *Computers & Graphics,* vol. 58, pp. 128-138, 2016.

[173] I. Goodfellow, Y. Bengio, and A. Courville, *Deep learning*. MIT press, 2016.

[174] G. Cybenko, "Approximation by superpositions of a sigmoidal function," *Mathematics of control, signals and systems,* vol. 2, no. 4, pp. 303-314, 1989.

[175] D. E. Rumelhart, G. E. Hinton, and R. J. Williams, "Learning internal representations by error propagation," California Univ San Diego La Jolla Inst for Cognitive Science, 1985.

[176] N. Hu and R. Burgueño, "Buckling-induced smart applications: recent advances and trends," *Smart Materials and Structures,* vol. 24, no. 6, p. 063001, 2015.

[177] S. Yuen and G. Nurick, "The energy-absorbing characteristics of tubular structures with geometric and material modifications: an overview," *Applied Mechanics Reviews,* vol. 61, no. 2, 2008.

[178] L. Dong and R. Lakes, "Advanced damper with high stiffness and high hysteresis damping based on negative structural stiffness," *International Journal of Solids and Structures,* vol. 50, no. 14-15, pp. 2416-2423, 2013.

[179] J. Winterflood, D. G. Blair, and B. Slagmolen, "High performance vibration isolation using springs in Euler column buckling mode," *Physics Letters A,* vol. 300, no. 2-3, pp. 122-130, 2002.

[180] N. Friedman and A. Ibrahimbegovic, "Overview of highly flexible, deployable lattice structures used in architecture and civil engineering undergoing large displacements," *YBL Journal of Built Environment,* vol. 1, no. 1, pp. 85-103, 2013.

[181] W. M. Huang *et al.*, "Instability/collapse of polymeric materials and their structures in stimulus-induced shape/surface morphology switching," *Materials & Design,* vol. 59, pp. 176-192, 2014.

[182] T. Bruns, O. Sigmund, and D. A. Tortorelli, "Numerical methods for the topology optimization of structures that exhibit snap-through," *International Journal for Numerical Methods in Engineering,* vol. 55, no. 10, pp. 1215-1237, 2002.

[183] T. Bruns and O. Sigmund, "Toward the topology design of mechanisms that exhibit snap-through behavior," *Computer Methods in Applied Mechanics and Engineering,* vol. 193, no. 36-38, pp. 3973-4000, 2004.

[184] A. Bhattacharyya, C. Conlan-Smith, and K. A. James, "Design of a bi-stable airfoil with tailored snap-through response using topology optimization," *Computer-Aided Design,* vol. 108, pp. 42-55, 2019.

[185] C. S. Andreasen, M. O. Elingaard, and N. Aage, "Level set topology and shape optimization by density methods using cut elements with length scale control," *Structural and Multidisciplinary Optimization,* pp. 1-23, 2020.

[186] W. Zhang, W. Yang, J. Zhou, D. Li, and X. Guo, "Structural topology optimization through explicit boundary evolution," *Journal of Applied Mechanics,* vol. 84, no. 1, 2017.

[187] W. Zhang *et al.*, "Stress-related topology optimization of shell structures using IGA/TSA-based Moving Morphable Void (MMV) approach," *Computer Methods in Applied Mechanics and Engineering,* vol. 366, p. 113036, 2020.

[188] J. Norato, B. Bell, and D. A. Tortorelli, "A geometry projection method for continuum-based topology optimization with discrete elements," *Computer Methods in Applied Mechanics and Engineering,* vol. 293, pp. 306-327, 2015.

[189] G. A. Wempner, "Discrete approximations related to nonlinear theories of solids," *International Journal of Solids and Structures,* vol. 7, no. 11, pp. 1581-1599, 1971.

[190] A. Jameson, "Aerodynamic shape optimization using the adjoint method," *Lectures at the Von Karman Institute, Brussels,* 2003.

[191] R. M. Hackett, *Hyperelasticity primer*. Springer, 2016.

[192] F. Wang, B. S. Lazarov, and O. Sigmund, "On projection methods, convergence and robust formulations in topology optimization," *Structural and Multidisciplinary Optimization,* vol. 43, no. 6, pp. 767-784, 2011.

[193] S. C. Subedi, C. S. Verma, and K. Suresh, "A Review of Methods for the Geometric Post-Processing of Topology Optimized Models," *Journal of Computing and Information Science in Engineering,* vol. 20, no. 6, 2020, doi: 10.1115/1.4047429.

[194] W. Zhang, J. Yuan, J. Zhang, and X. Guo, "A new topology optimization approach based on Moving Morphable Components (MMC) and the ersatz material model," *Structural and Multidisciplinary Optimization,* vol. 53, no. 6, pp. 1243-1260, 2016/06/01 2016, doi: 10.1007/s00158-015-1372-3.

[195] J. A. Norato, B. K. Bell, and D. A. Tortorelli, "A geometry projection method for continuum-based topology optimization with discrete elements," *Computer Methods in Applied Mechanics and Engineering*, vol. 293, pp. 306-327, 2015/08/15/ 2015, doi: https://doi.org/10.1016/j.cma.2015.05.005.

[196] J. C. Cuillière, V. Francois, and J. M. Drouet, "Towards the Integration of Topology Optimization into the CAD Process," *Computer-Aided Design and Applications*, Article vol. 11, no. 2, pp. 120-140, 2014, doi: 10.1080/16864360.2014.846067.

[197] J. Liu and Y.-S. Ma, "3D level-set topology optimization: a machining feature-based approach," *Structural and Multidisciplinary Optimization*, vol. 52, no. 3, pp. 563-582, 2015.

[198] J. Liu and A. C. To, "Computer-Aided Design-Based Topology Optimization System With Dynamic Feature Shape and Modeling History Evolution," *Journal of Mechanical Design*, vol. 142, no. 7, 2020.

[199] A. M. Mirzendehdel, M. Behandish, and S. Nelaturi, "Topology optimization with accessibility constraint for multi-axis machining," *Computer-Aided Design*, vol. 122, p. 102825, 2020.

[200] N. Morris, A. Butscher, and F. Iorio, "A subtractive manufacturing constraint for level set topology optimization," *Structural and Multidisciplinary Optimization*, pp. 1-16, 2020.

[201] M. Langelaar, "Topology optimization for multi-axis machining," *Computer Methods in Applied Mechanics and Engineering*, vol. 351, pp. 226-252, 2019.

[202] G. Kreisselmeier and R. Steinhauser, "Systematic control design by optimizing a vector performance index," in *Computer aided design of control systems*: Elsevier, 1980, pp. 113-117.

[203] A. R. Gersborg and C. S. Andreasen, "An explicit parameterization for casting constraints in gradient driven topology optimization," *Structural and Multidisciplinary Optimization*, vol. 44, no. 6, pp. 875-881, 2011.

[204] Q. Li, W. Chen, S. Liu, and H. Fan, "Topology optimization design of cast parts based on virtual temperature method," *Computer-Aided Design*, vol. 94, pp. 28-40, 2018.

[205] Q. Xia, T. Shi, M. Y. Wang, and S. Liu, "A level set based method for the optimization of cast part," *Structural and Multidisciplinary Optimization*, vol. 41, no. 5, pp. 735-747, 2010.

[206] Y. Wang and Z. Kang, "Structural shape and topology optimization of cast parts using level set method," *International Journal for Numerical Methods in Engineering*, vol. 111, no. 13, pp. 1252-1273, 2017.

[207] T. S. Kim, J. E. Kim, J. H. Jeong, and Y. Y. Kim, "Filtering technique to control member size in topology design optimization," *KSME international journal*, vol. 18, no. 2, pp. 253-261, 2004.

[208] B. Bourdin, "Filters in topology optimization," *International journal for numerical methods in engineering*, vol. 50, no. 9, pp. 2143-2158, 2001.

[209] O. Sigmund, "Morphology-based black and white filters for topology optimization," *Structural and Multidisciplinary Optimization*, vol. 33, no. 4-5, pp. 401-424, 2007.

[210] R. R. Kibbe, J. E. Neely, R. O. Meyer, W. T. White, M. Bonkoski, and P. Bradshaw, *Machine tool practices*. Wiley, 1982.